Preparation, characterization and nonlinear optical absorption studies in $Bi_{12}SiO_{20}$, Cu_2O and CdS nanomaterials

A thesis submitted for the Degree of

Doctor of Philosophy

by

H. Sekhar

School of Physics

University of Hyderabad

Hyderabad - 500 046

India

December 2012

To My Mother, Grandmother and Sister

DECLARATION

I hereby declare that the matter embodied in the thesis entitled "**Preparation, characterization and nonlinear optical absorption studies in $Bi_{12}SiO_{20}$, Cu_2O and CdS nanomaterials**" is the result of investigation carried out by me in the School of Physics, University of Hyderabad, India, under direct supervision of Prof. D. Narayana Rao.

Place: Hyderabad

Date: (H. Sekhar)

CERTIFICATE

This is to certify that the work described in this thesis entitled "**Preparation, characterization and nonlinear optical absorption studies in $Bi_{12}SiO_{20}$, Cu_2O and CdS nanomaterials**" has been carried out by Mr. H**. Sekhar**, under my direct supervision and this has not been submitted for any degree or diploma at this or any other University.

Place: Hyderabad

Date: **(Prof. D. Narayana Rao)**

Dean

School of Physics

ACKNOWLEDGEMENTS

It would not have been possible to write this doctoral thesis without the help and support of the kind people around me.

First and foremost, I would like to express my heartfelt appreciation to my supervisor, Prof. D. Narayana Rao, for giving me an opportunity to work under him. His wide knowledge and constructive comments have been of great help to me. I have learnt a lot from his dedication and hard work. His guidance to me goes even beyond science and has helped me to grow as a strong individual.

I thank Prof. S.P. Tewari, Dean, school of Physics, former Dean Prof. C .Bansal, and in-charge faculty for their co-operation in providing facilities in the school of Physics. I wish to express my warm and sincere thanks to my doctoral committee members: Dr. Anatha Lakshmi, Dr. V. Ashoka, Dr. V. Nirmal Kumar and Dr. Suneel Singh for their encouragement.

My association with Dr. P. Prem Kiran, ACRHEM has been very rewarding and sincere thanks to him. I also thank Prof. C. S. Sunandana for enlightening discussions. I owe due thanks all my lab mates Balu, Manoj, Deepak, Alee, Ashok, Sri Ram, Sreeramulu, Kuladeep, Anji, Ramya, Dr. R. Sathyavathi and Dr. L. Jyothi. I wish to thank all the technical staff, especially Abraham, Lakshmi Narayana (FE-SEM), Ravi Shankar (XRD), Kumar (Chem, XRD), Ramana (SEST, XRD) and Suresh (ESR).

At this juncture, I should extend my sincere thanks and deep appreciation to my best friends: A. Sendilkumar, B. Yugandhar, Sanjeev Kumar and Dr. P. Ravi (ACHREM) for many fruitful discussions. I thank M. Chandra Sekhar, Gupta and Hari (Prof. TPR students) from School of Chemistry, for rendering help at various stages of material synthesis. I thank some of sports

friends like V. Venkat Rao (Life Science (Coach)), Manikanta (ACHREM), Kishore and Y. Rakesh Kumar for their support.

Special thanks to G. Trivikrama Rao and Harshavardhan Reddy for their cooperation and support. I thank V. Gopal Krinshna, Pittala Suresh, D. Rajesh, Tirupathi, Siva, Dhanu, Ramesh, Ravi, Botta Raju, Sanjeeb, Srinivas (SEST) and other friends in the School of Physics.

Financial support in the form of UoH-BBL and UGC-CAS-BSR fellowship is gratefully acknowledged.

The unconditional love of my Amma, Sister and ammaamma and their blessings made me what I am today and I owe everything to them. Hence, I dedicate this thesis to them.

Finally, I thank all those who, directly or indirectly, helped me all along.

H. Sekhar

Table of contents

Chapter 1

Introduction

Abstract

In this chapter, we briefly summarize the different aspects of nanomaterials in terms of its properties, applications and modes of synthesis. We will discuss about its properties with size effects. The propagation of an ultrashort pulse in a nonlinear optical medium and various mechanisms are discussed in detail. The materials chosen for the present study and motivation for choosing these materials are explained. Chapter wise division of the thesis is given.

Chapter 1

1.1 Introduction

Matter can be classified according to their size. Macroscopic matter is visible with the naked eye. Atoms and molecules are microscopic with dimensions < 1nm. Mesoscopic particles are in the order of micron(s), can be observed with optical microscopes. In between microscopic and mesoscopic, is another class of matter nanoscopic particles, that has attracted many researchers to turn towards nanoscience and nanotechnology. A nanosolid, nanoparticle, nanocluster, nanocrystallite, and nanograin, etc., are defined as substances or devices that are in the shape of spherical dot, rod, thin plate, or any irregular shape smaller than 100 nanometer. Nanotechnology deals with processes that take place on the nanometer scale, that is, from approximately 1 to 100 nm. New physical and chemical properties are expected to occur when the size of the particles is reduced to the nanometric scale. The number of atoms or ions located on the surface increases considerably as the particle size reduces in the nano-domain [1]. In nanoscale materials the electronic structure also gets modified resulting in development of the discrete energy levels in contrast to continuous energy level in bulk materials [2,3] as shown in figure. 1.1. This phenomenon is also called quantum confinement. The main idea behind the nanoscience is to control and/or engineer the structural, physical, chemical or biological properties of materials on the nanometer (atomic) scale. It is worth stating that, in some cases the properties of these materials can be very different (most often superior) in comparison to the macroscale (bulk) properties of the same material [1-3]. Materials in the micrometer scale exhibit physical properties mostly similar to that of bulk form. Most of the properties of say, a homogeneous bulk spherical solid material with macroscopic dimensions are related to its crystal structure and chemical composition. The number of surface atoms of this bulk material comprises a negligible proportion of the total

number of its constituent atoms and hence plays a negligible role in the observed (bulk) properties of the material. Assuming that the particles are spherical in shape, then the surface area to volume ratio can be given as S/V = 3/r where r is the radius of the particle. Decreasing the particle radius increases the surface area to volume ratio.

Other properties of materials that are greatly affected by reduction in size to nanolevel are lowering of melting (due to melting of surface of atoms) point of the material, reduced lattice constant and the stabilization of crystallographic phases in different from the bulk [4-6]. Nanoscale materials possess unique properties. The effective thermal conductivity of suspensions containing spherical particles increases, since heat transfer takes place at the surface of the particles; it is therefore preferable to use particles with a large surface area to volume ratio [7]. Thus, if nanometer-sized particles could be suspended in traditional heat transfer fluids, a new class of engineered fluids with high thermal conductivity, called "nanofluids" and highly sensitive gas sensors could be fabricated.

Semiconductor quantum dots or nanocrystals either free-standing or embedded in a material have a larger bandgap. Due to their small size and high potential well for the delocalized electrons and holes, quantum dots have molecular-like discrete energy levels which exhibit strong size dependence as shown in figure 1.1. Some emerging multidisciplinary fields of applications have appeared such as nanoelectronics [8], nanostructured sensors (nano-nose) [9] and nanostructured solar cells [10]. Nanoscale materials bridge the gap between the behavior of an isolated atom and that of the corresponding bulk counterpart where interatomic interaction becomes dominance.

Nanomaterials have been put to use in the commercial products, with some being available for several years or decades. Today the range of

commercial products with nanomaterials is very broad, which include stain-resistant and wrinkle-free textiles, cosmetics, sunscreens, electronics, paints, varnishes and computer processor chips. Nanocoatings and nanocomposites are finding uses in diverse consumer products, such as windows, sports equipment, bicycles and automobiles. Nanoscale zinc oxide and titanium dioxide are using in cosmetics, sun-block creams and self-cleaning windows. Longer-lasting tennis ball using butyl rubber/ nano-clay composites and nanoscale silica is being used as filler in a range of products, including cosmetics and dental fillings.

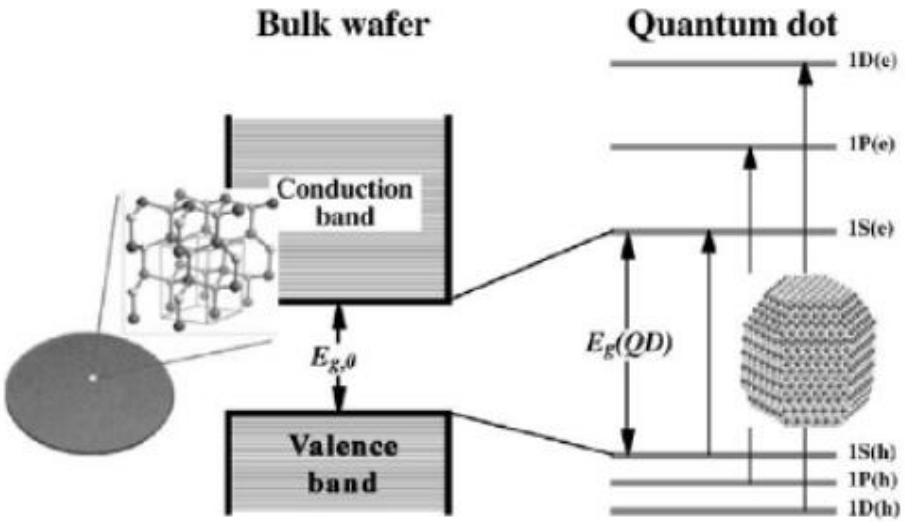

Figure 1.1 *Schematic diagram of a semiconductor bulk crystal with continuous conduction and valence energy bands separated by a fixed energy gap, E_g, and a quantum dot (QD) discrete atomic like states with energies that are determined by the QD radius R*

1.2 Classification of nanomaterials

Nanomaterials can be classified according to confinement of charge carriers in one dimension (if one dimension is reduced to the nano range while the other

two dimensions remain large eg. surface films), two dimensions (if two dimensions are reduced to the nanorange and one remains large eg. strands or fibres), or three dimensions (all three dimensions reduced to the nanorange eg. particles). They can exist in single, fused, aggregated or agglomerated forms with spherical, tubular, and irregular shapes. Several terminologies are commonly used to describe nanostructured materials; some of the terms encountered often: cluster, colloid, nanoparticle, nanocrystal, quantum dot. Although these terms are not very precisely defined, some general meanings are as follows. Cluster usually means a collection of units (atoms/molecules) surrounded by a ligand shell which makes it stable, isolable and soluble in an appropriate medium. Colloid is a stable liquid suspension having particles. Nanoparticles are solid particles with sizes up to a few hundred nanometers; they could be polycrystalline or a single crystal. If the nanoparticle is single crystal in nature, then it is termed as nanocrystal and if it exhibits confinement effect due to size in three dimensions, it is called quantum dot.

Some of the terms commonly occurred in nanoparticle or nanocrystal i.e. are discussed below.

Valence Band:

The lower edge of the bandgap contains all the electrons with the lowest energy called valence band. Since electrons tend to occupy energy states with the lowest energy possible, the valence band's energy levels are usually almost completely full.

Band Gap:

Bandgaps are the forbidden zone for electrons and they are the regions in between valence and conduction band.

Conduction Band:

Above the bandgap and higher energy levels are termed as conduction band. Because the bandgap is always much larger than the separation between energy levels, not many electrons can jump the bandgap and cross into the conduction band from the valence band. A very small number of electrons normally occupy the conduction band primarily due to thermal collisions. Electrons can also be stimulated to cross the bandgap if they absorb radiation with energy greater than or equal to the bandgap energy.

Continuous Band:

Energy levels are separated by a small amount of energy. For some processes, they may be treated as continuous levels of band (energy separation is negligible). This type of model works well for bulk semiconductor crystals.

Discrete levels:

Energy levels are separated by enough energy that the addition or subtraction of one atom or electron to the crystal will measurably change the energy of the bandgap. This type of model works well for semiconductor nanocrystals. Semiconductor nanocrystal having discrete states can be defined as a quantum dot.

Hole:

Holes are missing electrons in a valence band. They behave as particles with the same properties as that of the electrons that would have been occupying the same states except that they carry a positive charge, and arise when a negatively charged electron jumps to the conduction band. In natural bulk semiconductor material, an extremely small percentage of electrons occupy the conduction band the overwhelming majority of electron occupy the valence band, filling it almost completely. The only way for an electron in the valence band to jump to the conduction band is to acquire enough energy to cross the bandgap, and most

electrons in bulk simply do not have enough energy to do so. Applying an external stimulus such as heat, voltage, or photon flux can induce some electrons to jump the forbidden gap to the conduction band. The valence band location they vacate is referred to as a hole since it leaves a temporary "hole" in the valence band electron structure.

Exciton:

An exciton is a bound state of an electron and hole which are attracted to each other by the electrostatic Coulomb force. An electron-hole pair is created when an electron leaves the valence band and enters the conduction band. Excitons have a natural physical separation between the electron and the hole that varies from substance to substance; this average distance is called the exciton Bohr radius. In a large semiconductor crystal, the exciton Bohr diameter is small compared to the crystal, and the exciton is free to wander throughout the crystal. In a quantum dot, the exciton Bohr diameter is on the order of the physical dimension of the dot or smaller, and the exciton is confined. This is called quantum confinement, which is synonymous with having discrete, rather than continuous energy levels.

There are two situations, called the weak confinement and the strong confinement regime. In the weak regime, the particle radius is larger than the radius of the electron-hole pair, but the range of motion of the exciton is limited, which causes a blue shift of the absorption spectrum. When the radius of the particle is smaller than the orbital radius of the electron-hole pair, the motion of electron and hole become independent and the exciton does not exist. The hole and the electron have their own set of energy levels. Here also there is a blue shift.

1.3 Synthesis of nanomaterials:

Nanomaterials deal with very fine structures: a nanometer is a billionth of a meter. There are several methods to synthesize new isolated nanomaterials with well designed properties, not just by changing the chemical composition of the components, but by controlling the size and shape of the components.

The synthesis of nanomaterials and the creation of nanostructures are achieved mainly through two complementary methods identified as top-down and bottom-up approach (figure 1.2). Both methods play very important role to produce nanoscale materials and there are several advantages and disadvantages in both approaches. The top-down approach involves whittling down or dis-assemble (break, or dissociate) bulk (macroscopic) solids to the nanometer scale. This approach generally relies on physical processes, or a combination of physical and/or chemical, electrical or thermal processes for their production. Some of the popular methods that come under the category of top-down approach are high energy milling, electro-explosion, laser ablation, sputtering etc. The biggest problem with top down approach is the imperfection of surface structure and significant crystallographic damage to the processed patterns. But this approach leads to the bulk production of nano material. Regardless of the defects produced by top down approach, they will continue to play an important role in the synthesis of nano structures.

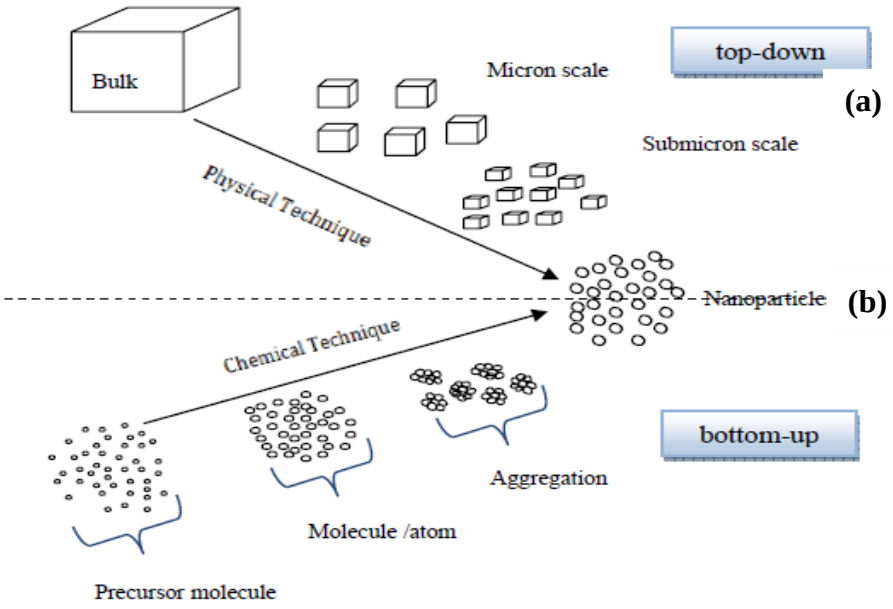

Figure 1.2 *The two complementary approaches (a) top-down and (b) bottom-up to synthesize nanomaterials.*

The bottom-up approach, on the contrary, involves assembling atom-by-atom, or molecule-by molecule into structures on the nanometer scale with properties varying according to the number of constituent entities/grain size. Building the system atom by atom or molecule by molecule guarantees the best control over all particles in the system. Commonly used techniques that come in category of bottom-up approach are sol-gel method, microemulsions, and chemical precipitation method.

1.3.1 Mechanical alloying

Mechanical milling (attrition) is one of the examples of 'top down' method for synthesizing metallic and ceramic nanomaterials, where the material is prepared by the structural decomposition of coarser-grained structures as a result of severe plastic deformation. This has become a popular method to produce nanocrystalline materials because of its simplicity, the relatively inexpensive

equipment needed, and the applicability to essentially the synthesis of all classes of materials. A ball mill, a type of grinder, is a cylindrical device used in grinding (or mixing) materials like ores, chemicals, ceramic raw materials and paints. Ball mills rotate around a horizontal axis, partially filled with the material to be ground plus the grinding medium. Different materials are used as media, including ceramic balls, and stainless steel balls. An internal cascading effect reduces the material to a fine powder.

Using this mechanical milling one can prepare large quantities of nano materials for various applications. Major disadvantage of this technique are

1. Broad size distribution
2. Varied particle shape or geometry
3. Significant amount of impurities and defects from the milling medium
4. Difficult to design and control desired particle size and shape

Mechanical milling is typically achieved using high energy shaker, planetary ball, or tumbler mills. The energy transferred to the powder from steel balls depends on the rotational (vibrational) speed, size and number of the balls, ratio of the ball to powder mass, the timing of milling and the milling atmosphere. Nanoparticles are produced by the shear action during grinding. To produce non-oxide materials by using mechanical alloying is very restrictive due to oxidation in air environment since it needs that the milling take place in an inert atmosphere and that the powder particles be handled in an appropriate vacuum system or glove box.

1.3.2 Colloidal Synthesis

Colloidal synthesis (attrition) is one of the examples of ‘bottom-up’ method for synthesizing nanomaterials. This method involves growing nanoparticles, nanorods and tetrapods of inorganic materials (elements and compounds) by chemical reaction of their precursors in a carefully chosen solvent. This has a

very simple method of producing nanocrystalline materials with a reasonable uniformity in sizes. Generally, when a solid is formed from its precursors through a chemical reaction, it starts with the fast formation of a multitude of nuclei. More and more of the solid product then add to the nuclei, and the sizes of the crystallites grow infinitely big in size. To arrest the growth of crystallites is possible by "cap" the surface by an appropriate surfactant, which is usually a long-chain organic molecule with a functional group [11]. Whether the surfactant should be added during the reaction, or be generated *in situ* or added post synthesis depends on the material under study. The selection of surfactant depends on the nature of nanocrystal forming materials. One can tune the size and shape of nanocrystal by controlling the reaction conditions like time, temperature, concentrations of the precursors, and chemical nature of reagents and surfactants.

1.3.3 Reverse Micelle Synthesis

Reverse micelle also called microemulsions have been used to prepare nanoparticles for more than two decades, and a wide variety of materials have been synthesized by these methods. The reverse micellar system is generally composed of two immiscible liquids such as water and oil, where the aqueous phase is dispersed as nanosize water droplets encapsulated by a monolayer film of surfactant molecules in a continuous nonpolar organic solvent such as hydrocarbon oil. The continuous oil phase generally consists of isooctane or hexane. Sodium bissulfosuccinate serves as the surfactant. In addition to water, aqueous solutions contain a variety of dissolved salts. The size of the reverse micelle, and subsequently the volume of the aqueous pool contained within reverse micelle, is governed by the water-to-surfactant ratio, also termed W_O, where $W_O = [H_2O]/[\text{surfactant}]$. A continuous exchange of the reverse micelle contents through dynamic collisions enables the reaction to proceed. However,

since the reaction is confined within the reactor cavity, growth of a crystal beyond the dimension of the cavity is inhibited. In the final stage of this synthesis, a passivating reagent, such as p-thiocresol, is added to the continuous oil phase. This species is then able to enter the aqueous phase as an anion and bond to the surface of the contained nanocrystal, eventually rendering the surface of the nanocrystal hydrophobic and inducing precipitation of the capped nanoparticles. Inorganic and metal nanoparticles have been made using this approach. By appropriate choice of the surfactant or mixture of surfactants, the shape of the cavity can be made cylindrical to produce nanorods [12].

1.3.4 Sol-gel process

The sol-gel is a wet chemical technique routinely used to synthesize wide variety of material like thin fibers, porous structures, dense powders and thin films. The starting materials used in the preparation of the "sol" are usually inorganic metal salts or metal organic compounds such as metal alkoxides. In sol-gel process, the precursor is subjected to a series of hydrolysis and polymerization reactions to form a colloidal suspension; Sol-gel synthesis is to “dissolve” the compound in a liquid in order to bring it back as a solid in a controlled manner. The precursors for synthesizing these colloids consist usually of a metal or metalloid element surrounded by various reactive ligands. The starting material is processed to form a dispersible oxide and forms a sol in contact with water or dilute acid. Removal of the liquid from the sol yields the gel, and the sol/gel transition controls the particle size and shape. Sol-gel processing refers to the hydrolysis and condensation of alkoxide-based precursors such as tetraethyl orthosilicate (TEOS). The reactions involved in the sol-gel process based on the hydrolysis and condensation of metal alkoxides can be described as follows:

$$MOR + H_2O \longrightarrow MOH + ROH \text{ (hydrolysis)}$$

$$MOH + ROM \longrightarrow M\text{-}O\text{-}M + ROH \text{ (condensation)}$$

Sol-gel method of synthesizing nanomaterials is very popular amongst chemists and is widely employed to prepare oxide materials. The sol-gel process can be characterized by a series of distinct steps. The interest in this synthesis method arises due to the possibility of synthesizing nonmetallic inorganic materials like glasses, glass ceramics or ceramic materials at very low temperatures compared to the high temperature process required by melting glass or firing ceramics.

1.4 Nonlinear Absorption

Since the advent of laser in 1960s, many interesting material properties are explored. However, along with laser came all the dangerous associated with high intensity light, including damage to optical sensor like human eye, range finders and night vision equipment. To protect the sensors from laser light, researchers exploring new materials that transmit low intensity light but absorb high intensity light. These materials known as optical limiters. As intensity light increases the transmitted light limits a threshold at which point it is clamped. When considering a material for optical limiter, two of the properties that are particular interest are the materials nonlinear absorption coeiffient and nonlinear refraction. By measuring these nonlinear optical properties of materials, these materials can be identified as optical limiters.

In the linear optics regime, that is associated with very low intensities, the interaction of light with transparent optical materials is straightforward. However, at the high intensities available from high power pulsed laser pulses, the subject becomes much richer, as the pulse itself affects and is affected by the material as it propagates through in dramatic ways. In this thesis we limit

our studies to third order nonlinear phenomenon associated with the interaction of pulsed laser pulses with transparent media that are observed at high input intensities namely.

The first idea about two-photon-absorption was developed by Albert Einstein in 1905. It is based on the simultaneous absorption of two photons to produce excitation to a level at the sum of the two photon energies. Then in 1931, Maria Goeppert-Mayer established a formula for two-photon absorption in an atomic or a molecular system using second-order quantum perturbation theory. When a medium is subject to an intense electric field such that due to an intense laser pulse, the polarization response of the material is described by equation 1.1. Assuming that the polarization of the medium can be expressed in a power series of the field strength $\overline{E}$

$$\overline{P} = \chi^{(1)} \cdot \overline{E} + \chi^{(2)} : \overline{\mathrm{E}}\overline{\mathrm{E}} + \chi^{(3)} \vdots \overline{E}\overline{E}\overline{E} ... \qquad (1.1)$$

Where $\chi^{(n)}$ is the complex susceptibility tensor of order n. The first term, $\chi^{(1)}$ is responsible for linear absorption and refraction, while the remaining terms are associated with light-induced nonlinear effects. The term $\chi^{(2)}$ is used only noncentrosymmetric crystal and it gives rise to sum and difference frequency mixing, optical rectification, and the electro-optic effect. The term most widely applied to optical limiting is that involving $\chi^{(3)}$. The most important third order optical nonlinear process is optical limiting, which is associated with imaginary part of $\chi^{(3)}$.

There are two types of nonlinearities, instantaneous and accumulative arise from interactions with memory, i.e. the polarization density generated by an applied field either develops or decays on a time scale comparable to or longer than the excitation duration. Such interactions are generally dissipative,

i.e. they require energy transfer from the field to the medium, and the nonlinearity itself is initiated by this energy transfer. Hence, in contrast with the instantaneous nonlinearities that depend on the instantaneous intensity within the medium, the accumulative nonlinearities typically depend on the energy density deposited in the medium. Examples of instantaneous nonlinearities are two or multi photon absorption. Examples of accumulative nonlinearities include nonlinear absorptive processes, such as excited-state absorption and free-carrier absorption, and nonlinear refractive processes associated with free-carrier generation or optically-induced heating.

1.4.1 Saturable and Reverse saturable absorbers

Shortly after invention of laser many researchers were investigating dyes for potential application to Q-switching of the laser cavity. The first reverse saturable absorption (RSA) behavior observed by Guiliano and Hess in 1967 while investigating vat dyes and their modified cousins. They observed that under intense laser pulses, these organic dyes not only bleach (saturable absorption (SA)) to transparency but instead darkened at high intensities. RSA occurs as a consequence of the absorption cross section of an excited molecular state being greater than that of the ground state; the system will be less transmissive. Since then a number of compounds have been found to possess such a property. These compounds include phthalocyanine, metallo-phthalocyanine [13], cubanelike transition-metal clusters [14], and King's complex [15]. Recently, semiconductor and metal nanoparticles are also shows RSA behavior in broad spectral range [16]. As the optical excitation intensity increases, more molecules are promoted to the excited state, thus giving rise to higher absorption at intense light excitation. Because the RSA process involves electronic transitions, materials that exhibit RSA generally have an extremely fast response. Two photon, multiphoton, excited state and free carrier

absorption processes show similar characteristics to that of RSA behavior. Furthermore, many of these molecules have a broad linear absorption, resulting in a broadband limiting response. These advantages make RSA extremely attractive for use in broadband optical limiting of laser pulses.

1.4.2 Two or multiphoton absorption processes:

Two photon absorption as well as multiphoton absorption (n>2) process has been studied in a wide variety of materials [17,18]. Especially in the last two decades, nonlinear absorption in organic molecules, semiconductor bulk materials, and semiconductor and metal nano materials has been largely investigated both experimentally and theoretically. In semiconductor nanocrystals, largely due to their size and shape dependent nonlinear optical properties, two or multi multiphoton absorption has emerged into an interesting hot research topic from last two decades [19,20]. In the following sections, the phenomenological quantifications of two and multiphoton absorption and associated optical nonlinearities are outlined.

Two photon absorption (TPA) can also be used in a manner similar to reverse saturable absorption (RSA) to construct optical limiters. In contrast with RSA, TPA is an instantaneous nonlinear process that involves a transition of electron from its ground state (1) of a material to a higher-lying state (2) via an intermediate virtual state. Two photon absorption (TPA) involves the simultaneous absorption of two photons as schematically shown in figure 1.3(a). In this case, the attenuation of the incident light is described by

$$\frac{dI}{dz} = -\beta I^2$$

where β is the two-photon absorption coefficient.

Three photon or multi photon absorption involves a transition from the ground state to a higher-lying state by the simultaneous absorption of three or more number of photons via multiple numbers of virtual states as shown in figure 1.3(b). In this case, the attenuation of the incident light is described by

$$\frac{dI}{dz} = -\alpha_n I^n$$

where α_n is the n-photon absorption coefficient.

$$\frac{dI(z)}{dz} = -\alpha_n I^n(z)$$

$$\int_{I_{in}}^{I_{out}} \frac{1}{I^n(z)} dI(z) = -\alpha_n \int_0^L dz$$

$$-\alpha_n L = \left[\frac{I^{-n+1}}{-n+1}\right]_{I_{in}}^{I_{out}} \Rightarrow \alpha_n L = \frac{1}{n-1}\left[\frac{1}{I_{in}^{n-1}} - \frac{1}{I_{out}^{n-1}}\right]$$

$$\alpha_n L = \frac{1}{(n-1)I_{in}^{n-1}}\left[1 - \frac{1}{T^{n-1}}\right],$$

$$where\ T = \frac{I_{out}}{I_{in}} \quad T^{n-1} = \frac{1}{1+\alpha_n L(n-1)I_{in}^{n-1}}$$

$$T = \frac{1}{\left[1+\alpha_n L(n-1)I_{in}^{n-1}\right]^{\frac{1}{n-1}}}$$

$$\frac{I_{in}}{\omega_0^2} = \frac{I_{00}}{\omega_Z^2}, \quad where\ I_{in} = \frac{I_{00}}{1+\frac{Z^2}{Z_0^2}}\ and\ \omega_Z^2 = \omega_0^2\left(1+\frac{Z^2}{Z_0^2}\right)$$

$$T = \frac{1}{\left[1+(n-1)\alpha_n L\left(I_{00}/\left(1+\left(Z/Z_0\right)^2\right)\right)^{n-1}\right]^{1/n-1}}$$

$$\Rightarrow T_{OA(nPA)} = \frac{1}{\left[1+(n-1)\alpha_n L\left(I_{00}/\left(1+\left(Z/Z_0\right)^2\right)\right)^{n-1}\right]^{1/n-1}}$$

where α_n is the effective MPA coefficient (n = 2 for 2PA; n = 3 for 3PA, and so on), I_{00} is the peak intensity (at Z = 0), I_{in} is intensity at sample position (if Z- is the distance from the focal point I_{in} (I_Z) is the intensity at that point), $Z_0 = \pi\omega_0^2/\lambda$ is Rayleigh range (figure 1.4), ω_0 is the beam waist at the focal point (Z = 0), dz is small slice of the sample, I_{in} is input intensity and I_{out} is output intensity of the sample.

If we retain only the 2PA term and ignore all other terms, we have an analytical expression for open aperture (OA) Z-scan for merely two-photon absorbers. Similarly retaining the 3PA term and ignoring the other terms provides us an analytical expression for OA scans for only three-photon absorbers.

$$T_{OA(2PA)} = \frac{1}{1+\alpha_2 L_{eff}\left(I_{00}/\left(1+\left(z/z_0\right)^2\right)\right)} \qquad (1.1)$$

$$T_{OA(3PA)} = \frac{1}{1+2\alpha_3 L'_{eff}\left(I_{00}/\left(1+\left(z/z_0\right)^2\right)\right)^{1/2}} \qquad (1.2)$$

The effective path lengths in the sample of length L for 2PA, 3PA is given as

$$L_{eff} = \frac{1-e^{-\alpha_0 L}}{\alpha_0} \quad L'_{eff} = \frac{1-e^{-2\alpha_0 L}}{2\alpha_0}$$

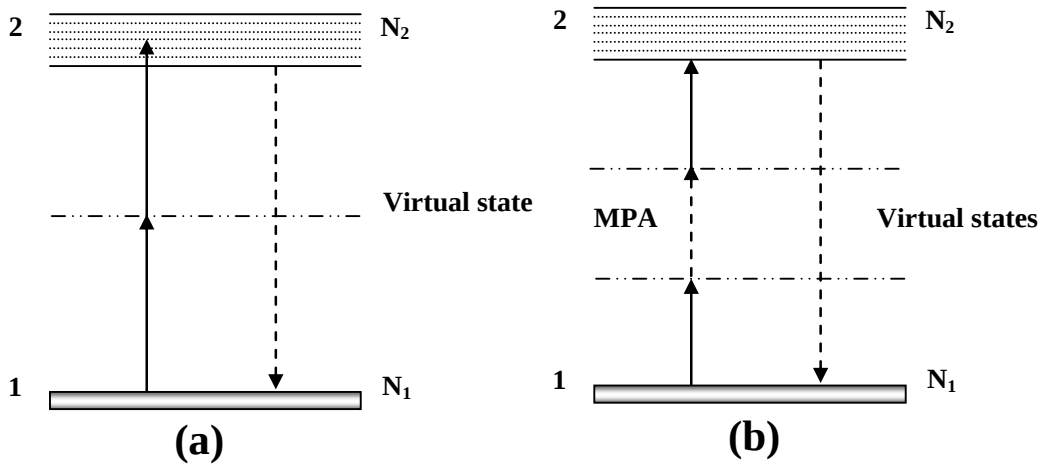

Figure 1.3 *Schematic energy level diagram for (a)Two-photon absorption (TPA); (b)Multi-photon absorption (MPA).*

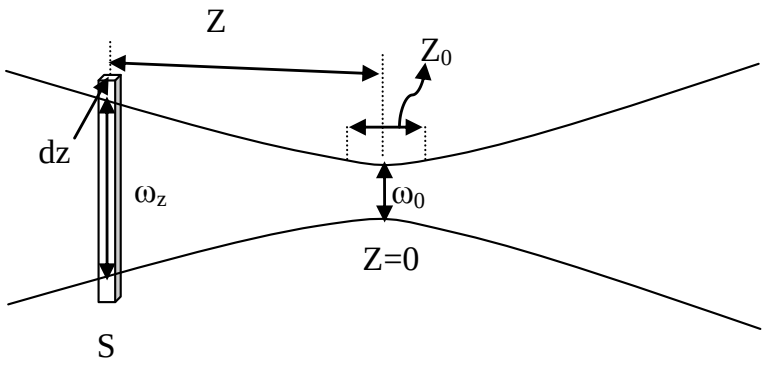

Figure 1.4 *Schematic diagram of focused laser beam.*

1.4.3 Excited state absorption (ESA)

Under high intensity light pumping, due to the significant population of the excited states, the excited state absorption becomes very important. The excited state's electrons can rapidly make a transition to higher excited states before it

decays back to the ground state. This phenomenon is obviously of paramount importance if the excited state absorption is resonant with another higher-lying state. As shown in figure 1.5, if the absorption cross-section of the excited state (σ_{ex}) is smaller than that of the ground state (σ_g), and if the excited state has a lifetime much longer than the excitation pulse duration, the transmission increases with the pump intensity, as more and more electrons are excited to the excited state N_2. This process leads to saturation of absorption (SA). Another situation is if the absorption cross-section of the excited state is larger than that of the ground state, then the system will be less transmissive when excited. This situation gives rise to the opposite result as saturable absorption and is thus called reverse saturable absorption (RSA). RSA gains special interest for the potential application such as optical limiting materials to protect human eyes and sensitive optical equipments. The concept is that this kind of materials can show high linear transmittance at low excitation level but display large nonlinear attenuation at high excitation level.

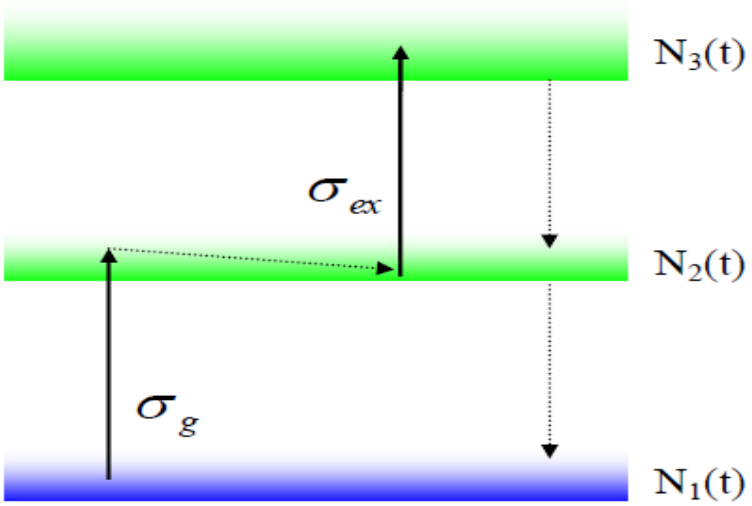

Figure 1.5 *Schematic diagram of excited-state absorption (SA or RSA).*

The ESA mechanism for organic molecular nonlinear absorption, usually understood by a five-level scheme that refers to five distinct electronic states as shown in figure 1.6. When an electron is excited from the ground state to the first excited singlet state S_1, the following situations can happen: (1) the electron can relax back to the ground state by radiative or nonradiative transition, with transition rate k_f; (2) the electron can undergo spin flip transition to a lower-lying triplet state T_1, with an intersystem crossing rate k_{isc}; or (3) the electron can transit to a higher-lying singlet state S_2 by absorbing another photon. The electron in the first triplet state T_1 also has two options. It can relax back to the ground state by another spin flip with a transition rate of k_{ph} or transit to a higher-lying triplet state T_2 by absorbing another photon.

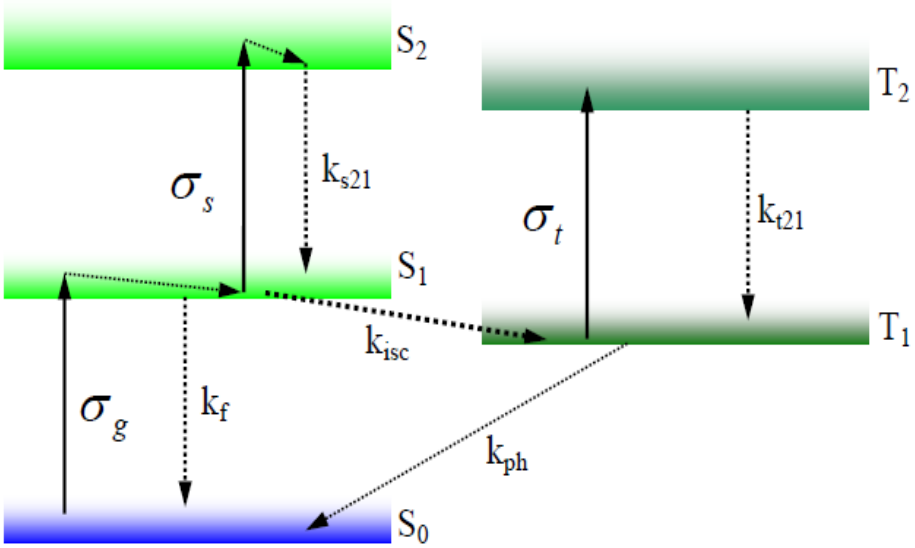

Figure 1.6 *Schematic diagram of a five-level model for organic molecular excited-state absorption.*

1.4.4 Free-carrier absorption (FCA)

Once carriers (electrons or holes) are optically generated by absorbing single photon in semiconductors or metals, these carriers can contribute to the current flow. They are also called free charge carriers or free carriers. When the electrons are excited to the conduction band, they will undergo ultrafast intraband carrier-carrier and carrier-optical phonon scattering and will come to the bottom of the conduction band. From there it will recombine with a hole in the valence band. At higher excitation intensities, before these excited carriers recombine, these free carriers have a very high probability to absorb another photon and make a transition to higher energy state within the bands. This process is called free-carrier absorption (FCA). It is analogous to excited-state absorption in a molecular system. It is clearly an accumulative nonlinearity, since it depends on the build up of carrier population in the bands as the incident optical pulse energy is absorbed.

1.5 Optical limiting concepts and Materials

High-powered pulsed lasers like nanosecond, picosecond and femtosecond laser sources found many applications in academic research as well as in many industrial and military applications. Semiconductor and solid-state lasers are portable, compact and efficient, and hence of special interest in the realm of laser weaponry. Tunable (wavelength and pulse width) high power laser sources is also available in modern research laboratories. To protect the optical components and human eye from such high power lasers one needs protectors like optical limiting materials. The function of optical limiting materials is transparent at low intensity and opaque at higher intensities. A lot of efforts have been paid to develop broadband and fast response optical limiting materials with low thresholds. An effective optical limiting materials should

possesses (i) low limiting threshold and high optical damage threshold and stability, leading to a large dynamic range, (ii) sensitive broadband response to long and short pulses, (iii) fast response time, and (iv) high linear transmittance, optical clarity, and robustness. Schematic representation of the behavior of an ideal optical limiter show in figure 1.7.

The limiting threshold ($I_{1/2}$) of the material is defined as the incident fluence where the transmission reduces by 50%. Clamping threshold of the material is defined as the input intensity/fluence at which the transmittance starts clamping. The threshold up to which material can provide effective limiting is called the damage threshold. The transmittance of the material increases with increasing intensity above the damage threshold.

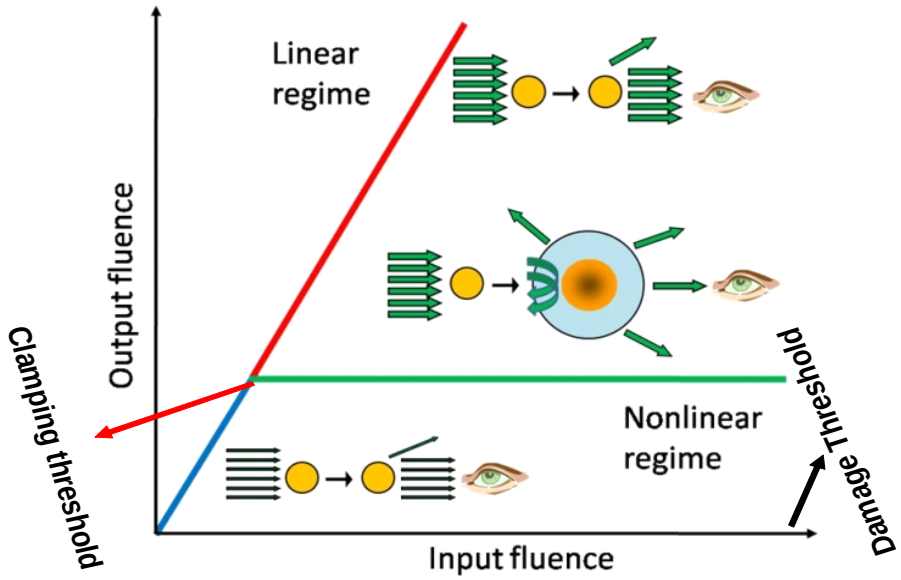

Figure 1.7 *Schematic representation of the behavior of an ideal optical limiter.*

The optical limiting materials can be designed based on energy absorbing and energy spreading. Combining two or more nonlinear optical effects one can achieve better limiting materials.

1.6 Materials for Optical Limiting

From last two decades, nonlinear optical properties of large wide variety of materials have been investigated for optical limiting applications based on different mechanisms. Optical limiting (OL) performance of various materials studied by various groups at continuous wave (CW) beams and ns/ps pulses; some of the materials show low limiting thresholds and low damage thresholds as well. Some of the materials show very high damage thresholds but high limiting thresholds. Some materials have a broad band spectral response with high $I_{1/2}$ and some have narrow band response with lower $I_{1/2}$. Improved nonlinear materials with negligible linear absorption with low limiting threshold are the prime consideration incorporation into sensitive optical components. Dyes lead to OL in selected portion of the visible band because of nonlinear absorption and refraction. Previously many research groups have studied the nonlinear optical properties of various quantum dots. Size and shape dependent optical limiting properties of quantum dots at visible and near IR region have also investigated. The optical limiting behavior of different shapes and sizes of nanocrystals studied at visible and near IR laser pulses, mainly occurs due to two-photon or multi-photon absorption processes.

The most extensively studied systems are phthalocyanines [13], Porphyrins, naphthalocyanines [21], fullerenes [22] and their derivatives in which long-lived triplet excited state can be produced conveniently. Fullerene and nanotubes-doped liquid crystals are another class of materials studied in the IR region and these materials exhibit optical limiting via TPA [23]. Other

materials such as photorefractive materials [24], photonic band gap materials, and nonlinear absorbers doped in xero-gels, sol-gel films [25], glasses [26], and double wall carbon nanotube-Fullerene hybrids [27] have been investigated and showed efficient optical limiting properties. The main objective of the present work has been to study better nonlinear optical limiting nano materials for eye-safe and as well as high damage thresholds for ns and ps pulses within the visible region of the spectrum.

Another of important goal of photonics research is generation of short wavelength or high energy photons from low energy photon through nonlinear optical absorption process. Harmonic generation, stimulated Raman scattering, and upconversion luminescence are three main methods for converting low energy photons to high energy photon. In the solid state, harmonic generation with a nonlinear crystal and multistep excitation in a rare-earth-ion-doped solid are well known and widely used for near-IR to visible upconversion. Among these processes, upconversion luminescence is perhaps the best known and most important. Upconversion luminescence (UCL) is a type of luminescence where the excitation wavelength is longer than the emission wavelength. Upconversion of photon energy is an interesting application in various multidisciplinary fields like laser technology, optical communications, storage, displays, imaging techniques, optical sensing and biological probing.

1.7 Outline of the thesis

The focus of this thesis is on the size-related spectroscopic (linear and nonlinear) investigations on single and multi phase oxide materials like bismuth silicon oxide ($Bi_{12}SiO_{20}$), cuprous oxide (Cu_2O) and cadmium sulphide (CdS). The aim of the thesis is two-fold. First is to prepare new nonlinear optical

nanomaterials with simple low cost chemical methods. Second is to explore the mechanisms leading to nonlinear absorption in these materials.

Chapter 2: Explains the experimental geometries and the general properties of the materials studied.

Chapter 3: In this chapter we observed enhanced linear and third order nonlinear optical properties of bismuth silicon oxide (BSO) nanocrystals as compared to their bulk materials due to confinement effects, which is explained in detail. The nonlinear optical properties are studied using a standard open aperture Z-scan which shows strong nonlinear absorption both with the nanosecond and picosecond pulsed excitations. In addition to the nonlinear absorption mechanism, nonlinear scattering was also observed to contribute to the reverse saturable absorption (RSA) behavior leading to a very high RSA behavior in both the time regimes. By combining the two nonlinear optical properties like nonlinear absorption and nonlinear scattering, we achieved a better limiting threshold in this type of materials at ns and ps regime.

Chapter 4: In this chapter we discuss about structural, linear and nonlinear optical properties of cuprous oxide with different morphologies. Cu_2O powders with different morphologies are prepared by simple chemical method. Due to confinement effects (enhanced band gap) we observed enhanced nonlinear optical absorption in the case of nano-clusters and micro-cubes compared to their micro-particles.

Chapter 5: In this chapter we discuss about the observation of confinement effects in CdS nano-morphologies and we explore its linear and nonlinear optical properties. Stokes and anti-Stokes luminescence was found higher for the 600 ºC heat treated powder samples as compared to the 400 ºC heat treated samples.

Chapter 6: The final chapter of the thesis summarizes the work carried out on the materials described above. Various processes leading to optical limiting,

enhanced RSA and optical nonlinearities are summarized. Future attempts towards the widely acceptable optical limiter and energy converting materials are proposed.

1.8 References

1. P.N. Prasad, Nanophotonics Wiley-Interscience, 2004
2. G. Cao, Nanostructures & nanomaterials: synthesis, properties & applications; Imperial College Pr, 2004.
3. G. Schmid, Nanoparticles: from theory to application; Wiley-VCH Weinheim, 2004.
4. S.B. Qadri, M. Kuno, C.R. Feng, B.B. Rath, M. Yousuf, App. Phys. Lett. 83 (2003) 4011.
5. A.N. Goldstein, C.M. Echer, A.P. Alivisatos, Science 256 (1992) 1425.
6. S.B. Qadri, E.F. Skelton, D. Hsu, A.D. Dinsmore, J. Yang, H.F. Gray, B.R. Ratna, Phys. Rev. B, 60 (1999) 9191.
7. P. Keblinski, S.R. Phillpot, S.U.S. Choi, J.A. Eastman, International J. Heat and Mass transfer 45(2002) 855.
8. S. Sengupta, H.S. Solanki, V. Singh, S. Dhara, M.M. Deshmukh, Phys. Rev. B 82 (2010) 155432.
9. P-C. Chen, G. Shen, C. Zhou, IEEE Transactions on Nanotechnology 7 (2008) 668.
10. K. Yu, J. Chen, Nanoscale Res Lett. 4 (2009) 1.
11. T. Pellegrino, S. Kudera, T. Liedl, A.M. Javier, L. Manna, W.J. Parak, Small 1 (2005) 48.
12. J. Eastoe, M.J. Hollamby, L. Hudson, Advances in Colloid and Interface Science 128-130 (2006) 5.

13. C. Yu, S. Yinglin, Q. Shiliang, W. Duoyuan, Optical materials 18 (2001) 219.
14. W. Ji, H. J. Du, S. H. Tang, S. Shi, J. Opt. Soc. Am. B 12 (1995) 876.
15. G.R. Allan, D.R. Labergerie, S.J. Rychnovsky, T.F.Boggess, A.L. Smirl, L. Tutt, J. Phys. Chem. 96 (1992) 6313.
16. P. Prem Kiran, S. Venugopal Rao, M. Ferrari, B.M. Krishna, H. Sekhar, S. Alee, D. Narayana Rao, Nonlinear Opt Quantum Opt 40 (2010) 223.
17. L.W. Tutt, T.F. Boggess, Prog. Quanr. Electr. 17 (1993) 299.
18. W. Nie, Adv. Mater. 5 (1993) 520.
19. N. Venkatram, R. Sathyavathi, D. Narayana Rao, Optics Express 15 (2007) 122258.
20. H. Sekhar, D. Narayana Rao, J. Nanopart. Res. 14 (2012) 976.
21. M. Hanack, T. Schneider, M. Barthel, J.S. Shirk, S.R. Flom, R.G.S. Pong, Coordination Chemistry Reviews 219–221 (2001) 235–258.
22. S. Subbiah, R. Mokaya, J. Phys. Chem. B 109 (2005) 5079.
23. N.V. Kamanin, P. Ya. Vasilyev, A.I. Vangonen, V.I. Studeonov, Yu. E. Usanov, E. Gondek, W. Wojcik, W. Imiolek, A. Danel, J. Non-Oxide Glasses 1 (2009) 205.
24. P.S. Aithal, P. Prem Kiran, D. Narayana Rao, J. Nonlinear Opt. Phys. Mater. 9 (2000) 217.
25. P. Prem Kiran, B.N.S. Bhaktha, D. Narayana Rao, G. De, J. Appl. Phys. 96 (2004) 6717.
26. J.M.P. Almeida, L. De Boni, A.C. Hernandes, C.R. Mendonça, Opt. Express 19 (2011) 17220.
27. K-S. Liao, J. Wang, D. Früchtl, N.J. Alley, E. Andreoli, E.P. Dillon, A.R. Barron, H. Kim, H.J. Byrne, W.J. Blau, S.A. Curran, Chemical Physics Letters 489 (2010) 207.

Chapter 2

Experimental Techniques

Experimental Techniques

Abstract

In this chapter, the details of various experiments carried out in this dissertation are explained. We also describe the different experimental techniques namely, X-ray powder diffraction, Fourier Transform Infrared (FTIR), micro-Raman, Absorption, Electro Paramagnetic Resonance (EPR) spectroscopy, Field emission scanning electron microscope (FESEM) with energy dispersive X-ray absorption spectroscopy (EDXAS), Transmission electron microscope (TEM), and Z-scan that form the basis of the studies presented in this thesis.

Chapter 2

The present chapter gives a brief description of different experimental techniques used in the present study. Very brief details of X-ray powder diffraction, Thermogravimetric analyzer (TGA), UV-Vis, FTIR, Raman, FE-SEM-EDAX, TEM and Z-scan experimental facilities used are given below.

2.1 X-Ray Diffraction (XRD)

X-ray Diffraction (XRD) is an analytical technique with a very broad range of applications in physics, materials science, geology, mineralogy, ceramics, etc. The powder diffraction is characteristic of the substance and forms a sort of fingerprint [1] of the substance and yield a great deal of structural information about the crystalline materials. Powder diffraction method involves the diffraction of monochromatic X-rays by a powder specimen. Monochromatic usually means a strong K_α characteristic component of the filtered radiation from X-ray tube operated above the K_α excitation potential of the target material. INEL X-ray diffractometer with Co target X-ray tube is used for the X-ray diffraction measurements. Position Sensitive Detector (PSD) filled with P10-gas (10% methane in Argon) is employed to record the counts.

The peaks of the X-ray diffraction pattern of the synthesized powders samples are compared with a standard available data for confirmation of the structure. We have used the standards like Willars Hand book, Joint Committee on Powder Diffraction Standards (JCPDS) Pcpdf win and National Bureau of Standards among the many available in the literature [2].

If the material under investigation is crystalline, then well-defined peaks will be observed while non-crystalline or amorphous systems show a hallow instead of well defined peaks. In X-ray diffraction the line broadening is caused by small crystallite size, the crystallite size can be estimated from the Scherrer's equation

$$d=k\lambda/\beta\cos\theta$$

where θ is the Bragg angle, λ is the wavelength of the X-rays, d is the mean dimension of the crystallite size composing the powder sample, β is the full width at half maximum of the pure diffraction profile on the 2θ scale in radians and k is a constant. In the determination of particle size by this method, it must be realized that instrumental effects might also increase the width of reflection and correction for instrumental broadening must be applied. This method can be used for the determination of approximate size of small crystals.

2.2 TGA-DTA

Thermal analysis is defined as a technique in which a physical property is recorded as a function of temperature. Thermo Gravimetric Analysis (TGA) is a technique where the change in mass of a sample is monitored under programmed heating. TGA measures the mass change (loss or gain) of a material with temperature. In Differential thermal analysis (DTA), the heat changes within a material are monitored by measuring the difference in temperature between the sample and a reference material, both of which are heated under identical conditions. These measurements provide qualitative and quantitative information about changes that involve endothermic (heat absorbed) and exothermic (heat evolved) processes via chemical reactions during the heating process. Generally speaking, phase transitions, dehydration, reduction and some decomposition reactions produce endothermic effects whereas crystallization, oxidation and some decomposition reactions produce exothermic effects. TGA/DTA measurements were carried out in the present investigation to study the decomposition pattern, thermal stabilities and phase transition temperature [3].

Chapter 2

In the present study, TGA/DTA analysis was carried out by Mettler Toledo TGA/DSC 1 at a heating rate of 10 ºC/min from 100 to 800 ºC in inert gas (N_2) atmosphere.

2.3 Fourier Transform Infrared (FT-IR) and Raman Spectroscopy

Raman and infrared spectroscopy are two complementary spectroscopic techniques employed to detect vibrations in molecules or semiconductors [4, 5]. A schematic of the different absorption and scattering processes are shown in figure 2.1. In FT-IR, infrared frequency of radiation energy is directed onto the sample. The loss of this frequency of radiation from the beam after it passes through the sample is then detected. Absorption occurs where the frequency of the incident radiation matches with the vibrational frequency of a molecule and the molecule is promoted to a vibrational excited state. They are widely used to get information on chemical structures and physical forms, and provide characteristic spectral patterns (‘fingerprinting’) of the molecule.

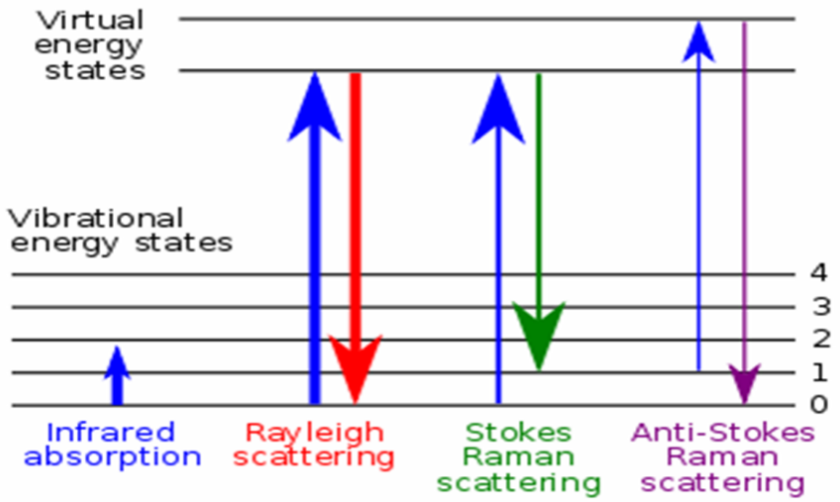

Figure 2.1 *Schematic representations of IR absorption and Raman scattering processes.*

In the present study, The IR spectra were measured from 400–4000 cm^{-1} with JASCO FT/IR-5300 model operating at a resolution of 4 cm^{-1}, for which the samples were admixed with KBr from Sigma-Aldrich and palletized.

Raman scattering is a nondestructive technique and does not require any special sample preparation techniques like KBr pellet method for IR studies. In the present work HR 800 Horiba Jobin Yvon confocal micro-Raman spectrometer equipped with grating having 1800 groves/mm was used to investigate the Raman peaks of oxide ($Bi_{12}SiO_{20}$, Cu_2O) and CdS nanocrystals. Calibration was performed with a silicon wafer by utilizing the first-order phonon band of Si at 520 cm^{-1} before and after recording. The spectrometer consists of three excitation laser sources; He: Ne laser which provides 632nm, Argon ion laser working at 514nm, and diode laser providing 785nm wavelengths. The detecting system is a CCD. A notch filter is used in the HR 800 for the rejection of the exciting line. It is specific for one wavelength and it is changed with excitation wavelength source is changed. A joy stick is provided to position the sample exactly under the illumination spot. The notch filter, in particular, is widely used. It is designed to absorb all light of the frequency of the incident laser light. The notch filter has a huge advantage when used; the spectra can be recorded very close to the excitation wavelength without saturating the detector. This reduces the size of Raman spectrometers and improved their efficiency.

2.4 Electron paramagnetic resonance spectroscopy

Electron paramagnetic spectroscopy (EPR) is also known as electron spin resonance (ESR) or electron magnetic resonance (EMR) and measures the transition frequency between electron spin states. EPR spectroscopy is a technique for studying chemical species that have one or more unpaired

electrons, such as free radicals or inorganic complexes possessing a transition metal ion. EPR is a powerful non-destructive analytical method and deals with the absorption of microwave radiation by an unpaired electron (namely free radicals, odd-electron molecules, transition metal complexes, rare earth ions, etc.) under a strong magnetic field [6,7].

EPR or ESR spectra can be generated by either varying the frequency of electromagnetic radiation incident on a sample while holding the magnetic field constant, or varying the magnetic field and keeping the frequency of electromagnetic radiation constant. Usually, the frequency of electromagnetic radiation is kept fixed and magnetic field is varied in order to obtain an absorption spectrum.

The electromagnet generates static/DC magnetic field when current is passed through it. Radiation source (microwave frequency) is a klystron. Sample is placed in EPR tube with typically 4 mm in diameter. The sample is placed in a resonant cavity which admits microwaves through an iris. The radiation may be incident on the sample continuously (i.e., continuous wave) or pulsed. The cavity is located in the middle of an electromagnet and helps to amplify the weak signals from the sample. The source is modulated and the resulting signal generated goes through a phase sensitive detector and the signal is amplified.

In this dissertation, we have used JEOL Company EPR spectrometer with model JES-FA 200, to investigate impurity (paramagnetic) spices in as synthesized nanopowders. In this model, the microwave unit is X band unit which provides (8.65-9.75) GHz range. Magnetic field strength can be varied from 0-1 tesla.

2.5 Microscopy

Microscopy involves the study of objects that are too small to be examined by the unaided eye. There are many types of microscopes, the most common and first to be invented is the optical microscope which uses light other electrons microscope which uses electron to image the sample [8].

2.5.1 Light Microscopy

Light-optical microscopes daylight or light from a lamp is directed via a lens or mirror through the specimen and into the microscope, which creates a real image on the retina of the eye or within an attached camera. A modern light microscope has a magnification of about 1000X and enables the eye to resolve objects separated by 200 nm. As scientists and inventors toiled to achieve better resolution, they soon realized that the resolving power of the microscope was not only limited by the number and quality of the lenses, but also by the wavelength of the light used for illumination. With visible light it was impossible to resolve points in the object that were closer together than a few hundred nanometers. Using light with a shorter wavelength (blue or ultraviolet) gave a small improvement. Immersing the specimen and the front of the objective lens in a medium with a high refractive index (such as oil) gave another small improvement, but these measures together only brought the resolving power of the microscope to just under 100 nm. This is an optical instrument containing one or more lenses producing an enlarged image of a sample placed in the focal plane.

2.5.2 Electron Microscopes

In the 1920s, it was discovered that accelerated electrons behave in vacuum much like light. They travel in straight lines and have wavelike properties, with a wavelength that is about 100,000 times shorter than that of visible light. Compared to conventional optical microscope, an electron microscope offers

advantages including high magnification, large depth of focus, great resolution and ease of sample preparation and observation. Today, electron microscopes have reached resolutions of better than 0.05 nm, more than 4000 times better than a typical light microscope and 4,000,000 times better than the unaided eye. The theoretical resolution limit of conventional optical imaging methodology (200 to 300 nanometers for visible light) was the primary factor motivating the development of recent higher-resolution scanning probe techniques, such as scanning tunneling microscope (STM), atomic force microscopy (AFM), transmission electron microscopy (TEM) and scanning electron microscopy (SEM). The specimen in an electron microscope is usually in a dry state, surrounded by a high vacuum.

Accelerated electrons in an FE-SEM or TEM carry significant amount of kinetic energy, and this energy is dissipated as a variety of signals produced by electron-sample interactions as the incident electrons are decelerated in the solid sample. These signals include secondary electrons (that produce SEM images), backscattered electrons (BSE), diffracted backscattered electrons (that are used to determine crystal structures and orientations of minerals), photons (characteristic X-rays that are used for elemental analysis and continuum X-rays), visible light, and heat. Secondary electrons and backscattered electrons are commonly used for imaging samples; secondary electrons are most valuable for showing morphology and topography on samples and backscattered electrons are most valuable for illustrating contrast in composition of multiphase samples (i.e. for rapid phase discrimination). In order to be observed with a FE-SEM, objects are first made conductive for current. This is done by coating them with an extremely thin layer (1.5 - 3.0 nm) of gold. In this dissertation, we have used Carl ZEISS, FEG, Ultra 55 FE-SEM model and Tecnai 20 G2 Stwin, FEI electron microscope operated at 20 kV using Gatan

CCD camera to analyze particle morphology, crystallinity and elemental analysis.

2.6 UV-Visible Absorption Spectroscopy

If the energy of an incident photon corresponds to the energy gap between the ground state of a molecule and an excited state, the photon may be absorbed and the molecule is promoted to the higher energy excited state. It is this change which is measured in absorption spectroscopy by the detection of the loss of that energy of radiation from the light. UV-Vis spectrophotometer is used to characterize the absorption, transmission, and reflectivity of a variety of technologically important materials.

Samples for UV-Vis spectrophotometers are most often liquids, although the absorbance of gases and even of solids can also be measured. Samples are typically placed in a transparent cell, known as cuvette. Cuvettes are typically rectangular in shape; commonly with an internal width of 1 cm. Sample container used must allow radiation to pass over the spectral region of interest. The most widely applicable cuvettes are made of high quality fused silica or quartz glass because these are transparent throughout the UV, visible and near infrared regions. Glass and plastic cuvettes are also common, although glass and most plastics absorb in the UV, which limits their usefulness to visible wavelengths. In the present thesis we performed UV–Vis absorption studies by using JASCO UV-Vis spectrophotometer.

2.7 Z-Scan Technique

The Z-scan technique is used to investigate nonlinear optical properties of materials. The Z-scan technique is a single beam technique, which allows the determination of the real and imaginary parts of the third order nonlinear

susceptibility [9]. This technique is a simple, sensitive, single beam method that uses the principle of spatial beam distortion to measure both the sign and the magnitude of refractive nonlinearities of optical materials. The experiment uses a Gaussian beam from a laser in tight focus geometry to measure the transmittance of a nonlinear medium through a finite aperture in the far field as a function of the sample position Z, from the focal plane. Analysis of the transmitted intensity through the sample as the function of sample position (known as Z-scan curve), gives the real and imaginary parts of the third order susceptibility. In addition to this, the sample transmittance without an aperture is also measured to extract complementary information about the absorptive nonlinearities of the sample.

The sensitivity of the experiment to refractive nonlinearities is entirely due to the aperture. The removal of the aperture will make the Z-scan sensitive to absorptive nonlinearities alone. Thus by doing the Z-scan with and without aperture, both the refractive and absorptive nonlinearities of the sample can be studied. The schematic of an open aperture Z-scan is as shown in figure 2.2. Spatially filtered input beam is focused using a lens. The sample is scanned across the focus using a stepper motor controlled by PC. The transmitted light is then collected using another lens (large area) of f ~ 100 mm and fast photodiode (FND100). Different neutral density filters are used for attenuation to ensure that the photodiode does not get saturated. The photodiode output is fed to a lock-in amplifier or a boxcar averager/gated integrator and is finally recorded. The averaged signal is then sent to an interfaced ADC card and then to a computer.

Z-scan technique has the following advantages

- Simplicity of the experimental scheme.
- As a single-beam technique, it has no difficult alignment other than keeping the beam centered on the aperture.
- It can be used to determine both the magnitude and the sign of n_2. The sign is obvious from the shape of the transmittance curve.
- Under rather general conditions that are easily fulfilled, the data analysis is quick and simple, making it a good method for screening new nonlinear materials. Under certain conditions, it is possible to isolate the nonlinear refractive and nonlinear absorptive contributions to the far-field transmittance.
- The technique is also highly sensitive, capable of resolving a phase distortion of ~ λ /300 in samples of high optical quality.
- Finally, the Z-scan can also be modified to study nonlinearities on different time scales as well as higher order contributions.

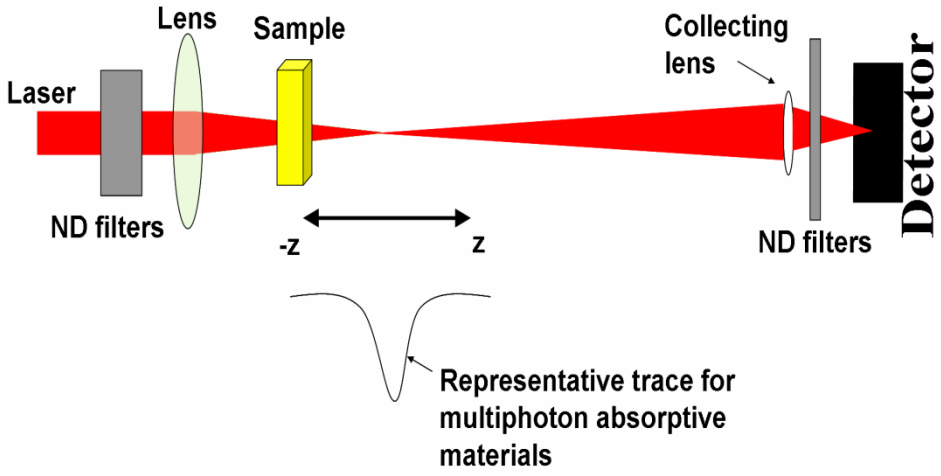

Figure 2.2 *Schematic of the experimental setup of the Z-scan technique.*

Chapter 2

The Z-scan technique has been used extensively to study different materials like semiconductors, nano-crystals, semiconductor-doped glasses, liquid crystals, organic materials, biomaterials etc. To enhance its sensitivity and applicability new extensions have been added. A two color Z-scan is used to perform the studies of non-degenerate optical nonlinearities. A much more sensitive technique, EZ-scan (eclipsed Z-scan), has been developed which utilizes the fact that the wings of a circular Gaussian beam are much more sensitive to the far-field beam distortion. A reflection Z-scan technique was introduced to study the optical nonlinearities of surfaces. Z-scan with top-hat beams, elliptical Gaussian beams have been performed resulting in better sensitivity. The Z-scan technique is used to measure two kinds of nonlinear optical properties. Open aperture Z-scan is used for absorptive nonlinearity and the closed aperture Z-scan is used for sign of the refractive nonlinearity.

2.8 Stokes and anti-Stokes luminescence

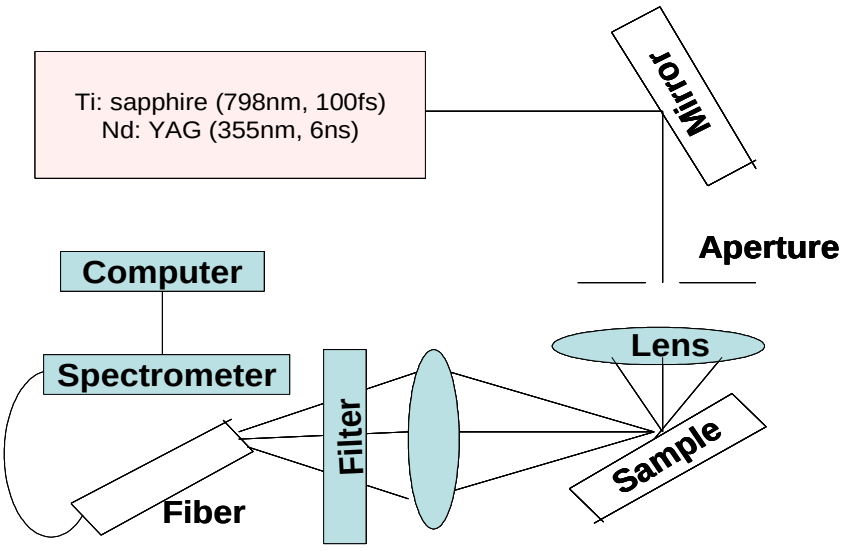

Figure 2.3 *Experimental setup for Stoke and anti-Stokes luminescence measurements.*

The experimental setup for the Stokes and anti-Stokes luminescence measurement is shown in figure 2.3. For Stokes luminescence (down conversion) samples were excited with 6 ns pulse duration third harmonic at 355 nm of the Nd: YAG laser with a repetition rate of 10Hz. For recording the anti-Stokes (Up-conversion) luminescence of solid samples, 100-fs pulses delivered by a Ti: sapphire laser at 798 nm with a repetition rate of 80 kHz was employed for excitation. Excitation power was varied by using a continuously adjustable neutral density filter and keeping a fixed distance between the sample and the focusing lens. Up and down conversion luminescence spectra were collected by Ocean Optics fiber spectrometer connected with a computer.

2.9 Reference

1. B.D. Cullity, Elements of X-Ray Diffraction (Ind. Ed.) (Addison-Wesley, 1977).
2. Theo Hahn, International Tables for Crystallography, Volume A: Space-Group Symmetry, Published for The International Union of Crystallography by Springer (2005).
3. M.E. Brown, Introduction to Thermal Analysis, Kluwer Academic Publisher, London, 2001.
4. Ewen Smith and Geoffrey Dent, Modern Raman Spectroscopy – A Practical Approach (John Wiley & Sons Ltd, 2005)
5. Bernhard Schrader, Infrared and Raman Spectroscopy (VCH Publishers. Inc., New York, 1995)
6. J.R. Pilbrow, Transition Ion Electron Paramagnetic Resonance, Clarendon Press, Oxfor, 1990.
7. F.E. Mabbs and D. Collison, Electron Paramagnetic Resonance of d Transition Metal Compounds, Elsevier, Amsterdam, 1992.
8. Ray F. Egerton, Physical Principles of Electron Microscopy, Springer, 2005.

Chapter 2

9. M. Sheik-Bahae, A.A. Said, T.H. Wei, D.J. Hagan, E.W. Van Stryland, IEEE J Quantum Electron 26 (1990) 760.

Chapter 3

Preparation, characterization and nonlinear optical absorption studies in $Bi_{12}SiO_{20}$ nanocrystals

$Bi_{12}SiO_{20}$ Nanocrystals

Abstract

In this chapter we discussed about stabilization of the sillenites phase by impurity doping (Si) and what temperature it needs to evolve in to single sillenite phase, was studied by using different spectroscopic techniques like XRD, FT-IR and Raman studies. The X-ray diffraction, FT-IR and micro-Raman studies revealed the formation of pure single phase cubic structured $Bi_{12}SO_{20}$ (BSO) nanocrystals at 700 ºC of calcination temperature. TEM studies have confirmed that as synthesized BSO powders were crystalline into nano meter size. We observed the enhanced Linear and nonlinear optical properties of sillenites nanocrystals compare to their bulk sillenite single crystals due to enhanced band gap.

The results of this chapter are published in Materials Chemistry and Physics 130 (2011) 113– 120, "Structural, linear and enhanced third-order nonlinear optical properties of $Bi_{12}SiO_{20}$ nanocrystals "by ***H. Sekhar****, P. Prem Kiran and D. Narayana Rao*

Chapter 3

3.1 Introduction

The synthesis and characterization of nanostructures of various oxides have become extremely important from both the fundamental and applications point of view [1-3]. Bismuth Oxide (Bi_2O_3) exists in several polymorphic forms. At low temperature it forms monoclinic (α-Bi_2O_3). At 730 °C α-Bi_2O_3 converts to a cubic structure (δ-Bi_2O_3) that remains stable up to the melting point 825 °C. Depending on the cooling rate δ-Bi_2O_3 goes to two metastable phases: tetragonal (β-Bi_2O_3) or body centered cubic (γ-Bi_2O_3). This γ-Bi_2O_3 phase is called sillenite, which is stabilized by the presence of a small amount of wide variety of impurities forming a compound of bismuth sillenite with a structure of ($Bi_{12}MxO_{20\pm\delta}$). Here M is an element from the II–V groups (Zn, Pb, Al, Si, Ge, etc.) of the periodic table. The oxidation state of the M cation ranges from +2 to +5. In this type of sillenites charge compensation is preserved by means of local distortion of the bismuth-oxygen frame work [4]. This body centered cubic structure of sillenite compounds facilitate the solubility of novel metal ions in the crystals, because the tetrahedron of oxygen atoms surrounding the M atoms is able to expand or contract without a major effect on the remaining atomic arrangement. The unit cell of the body-centered cubic compound and the X-ray powder diffraction pattern are very similar to those for metastable γ-Bi_2O_3 and it has been customary to refer to these compounds as γ-Bi_2O_3 structure. The overall structure of $Bi_{12}SiO_{20}$ can be described as seven oxygen coordinated Bi polyhedron, which shares corners with other identical Bi polyhedron and with SiO_4 tetrahedron. The four oxygens in the tetrahedral are generally labeled as O(3), the oxygen atoms in the diagonals of the unit cell O(2), and the oxygens placed in the lowest-symmetry positions O(1). The structural study of bismuth germinate by Abrahams et al [5] shows that the sillenite phase belongs to the polar space group T3 (I 23) and has the point

symmetry group T (23). Though many nanostructures like nanocrystals, nanorods and nanosheets of binary oxides like Bi_2O_3 [6,7] and SiO_2 [8-10] were synthesized successfully, the synthesis of ternary oxide nanostructures is still a formidable challenge due to their metastable property. Even though, many ternary oxides containing bismuth oxide were synthesized and their photocatalytic properties were studied [11,12], synthesis of nanostructures of $Bi_{12}MO_{20}$ where M is Si, Ge, Ti etc., has been a very recent phenomenon [13-15]. In the past, preparation of $Bi_{12}SiO_{20}$ (BSO) has been achieved in both the bulk and thin film forms by a variety of means [16,17]. Though few aspects of the photo-induced second-order nonlinear optical properties of nanocrystallites of $Bi_{12}TiO_{20}$ were studied [14,15], there are no studies in the literature, to the best of our knowledge, on thorough characterization of nanocrystals of $Bi_{12}SiO_{20}$. The chemical solution decomposition (CSD) method can provide better control of the texture of the resulting materials and ensures an increased uniformity of the product.

Nonlinear optical properties like nonlinear absorption, refraction and their application towards optical limiting applications were investigated in pure and doped sillenite family of bulk single crystals over visible and infrared ranges suggesting that in sillenites nonlinear absorption plays a significant role in the carrier generation process induced by short laser pulses [18-21]. Though the bulk single crystals have significant nonlinear optical properties, their major drawback is the growth process leading to the defects eventually introducing the trap states between the valence and the conduction band modifying the energy band structure significantly [22,23], in turn slowing down their optical response. We aim at understanding modification to the inherent nonlinearities of these crystals by reducing the defects and to remove the trap states by synthesizing the nanocrystals. Most of the nanoparticles exhibit interesting

nonlinear optical properties like two- and three-photon absorption, switching of the nonlinear optical properties compared to their bulk counterparts due to enhanced band gap [24,25]. In addition, the nanoparticles show nonlinear scattering that assist the nonlinear absorption processes [26,27].

3.2 Synthesis of BSO nanopowders

The $Bi_{12}SiO_{20}$ powders were prepared by using chemical solution decomposition (CSD) technique. Bismuth nitrate ($Bi(NO_3)_3.\ 5H_2O$) (Sisco Research Laboratories (AR Grade)) and tetraethyl orthosilicate ($(C_2H_5O)_4Si$) (Sigma-Aldrich 99%) were selected as the precursor materials. Glacial acetic acid (HPLC) and 2-methoxyethanol (HPLC) were used as co-solvents. Bismuth nitrite and tetraethyl orthosilicate (TEOS) are taken in 12:1 moles ratio. Initially, bismuth nitrate was dissolved in glacial acetic acid. Stoichiometric amount of tetraethyl orthosilicate was then added drop wise to the above solution under constant stirring. The resulting solution was diluted with 2-methoxyethanol to adjust the viscosity and surface tension of the solution, and was further stirred for 8 hours to yield a homogenous transparent sol. Prior to calcinations, the resultant sol was preheated at 100 ºC for 16 hours to remove the solvents. The dried mass, which was the so-called precursor, was then moved into a furnace and calcined at 500, 600 and 700 ºC for 1 hour. The phase purity of this calcined powder samples were characterized systematically by using different spectroscopic techniques.

3.3 Results and Discussion

3.3.1 TG-DTA measurements

Thermal analysis of the dried precursors (100 ºC) 10.5 mg was used for TG–DTA thermal analyzer at the heating rate of 15 ºC/min from 100 to 800 ºC

under ambient atmosphere to know the possible changes occurring when the materials were subjected to heat treatment. Differential thermal analysis and thermo gravimetric (TG-DTA) measurements indicated exothermic effect between 260 and 400 ºC (figure 3.1(a)) is attributed to the oxidation of organic residues and decomposition of nitrates. This leads to a major weight loss of approximately 21% in TG curve (figure 3.1(b)) at the same temperature. The second small exothermic peak at 510 ºC, with a small weight loss, is associated with the combustion of the remaining organic constituents in the precursor.

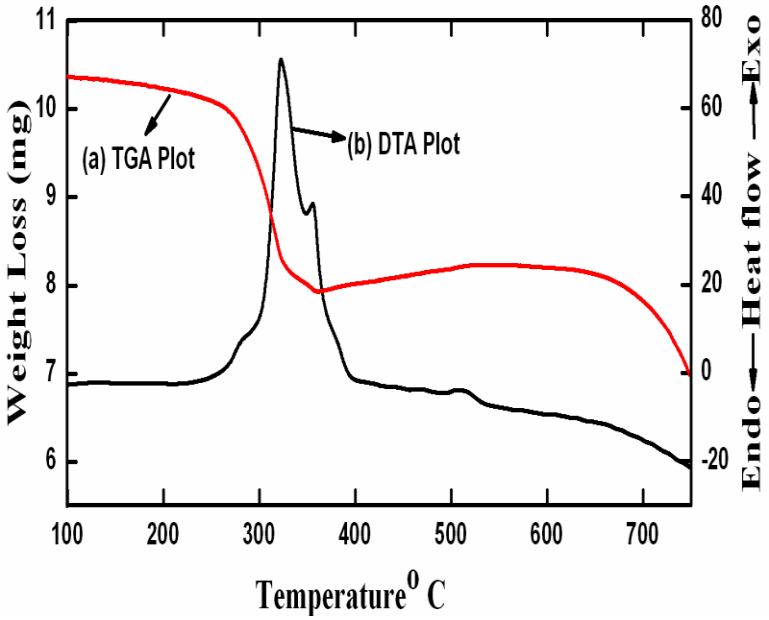

Figure 3.1 *(a) TGA curve and (b) DTA curve of BSO precursor powders.*

3.3.2 X-ray powder diffraction studies

The structural properties of the samples calcined at 500, 600 and 700 ºC were studied by X-ray powder diffraction technique as shown in figure 3.2. X-ray powder diffraction results of the nanopowders calcined at 500 and 600 ºC for 1 hour suggest that sillenite phase begins to form around the calcination

temperatures of 500 and 600 ºC, though it is not pure single phase and shows the presence of multiple phases like BSO and α-Bi_2O_3. At 600 ºC temperature peaks at 25.7° and 48.5° belonging to α-Bi_2O_3 (JCPDF Card 71-0465) (002), ($\bar{1}$04) crystal planes were observed. With the increase of calcination temperature to 700 ºC, the intensity of the diffraction peaks of $Bi_{12}SiO_{20}$ increases while those of α-Bi_2O_3 decrease.

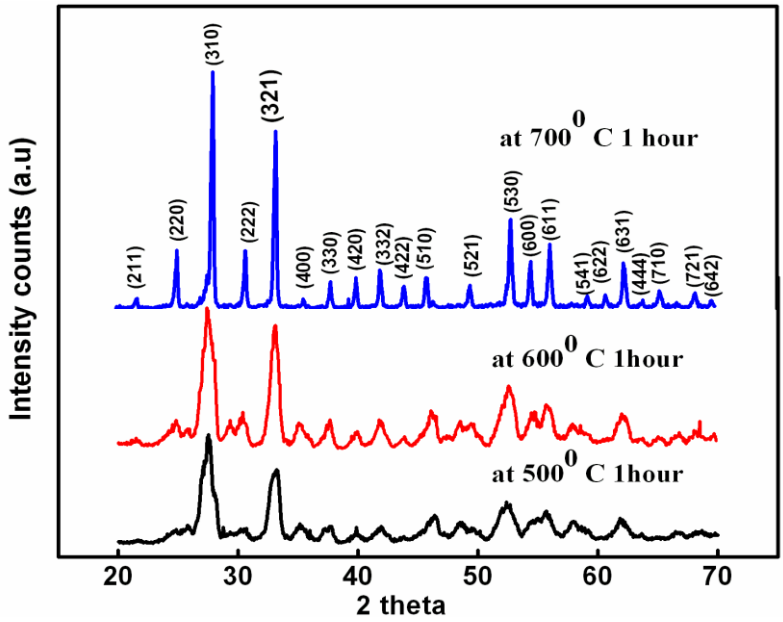

Figure 3.2 *XRD data of BSO precursor powders calcinated at 500, 600 and 700 ºC for 1 h.*

As the calcination temperature reaches 700 ºC, the peaks of α-Bi_2O_3 disappear completely and the peaks belonging to the pure $Bi_{12}SiO_{20}$ in single phase without any impurities were observed. The XRD pattern of as-prepared BSO sample calcined at 700 ºC for 1 hour is body centered cubic structure and good agreement with the JCPDF Card 37-0485. The XRD data were also analyzed by XRDA software and using the data, we find the lattice parameter *'a'* as 10.0886

Å. The average grain size of $Bi_{12}SiO_{20}$ calcined at 700 ºC, was calculated using the (310) diffraction peak as reference according to the Scherrer's formula. The average grain size was found to be around 46 nm.

3.3.3 Infrared spectroscopy

The infrared spectra (IR) were measured using KBr pellets made from a mixture of BSO powders calcined at 500, 600 and 700 ºC in transmission mode at room temperature. The pellet thickness varied from 0.5–0.6 mm. FT-IR spectra of BSO calcined at 500, 600 and 700 ºC are shown in figure 3.3. With increasing temperature up to 700 ºC, the spectrum showed sharper absorption peaks, indicating a better alignment of the cubic sillenite structure.

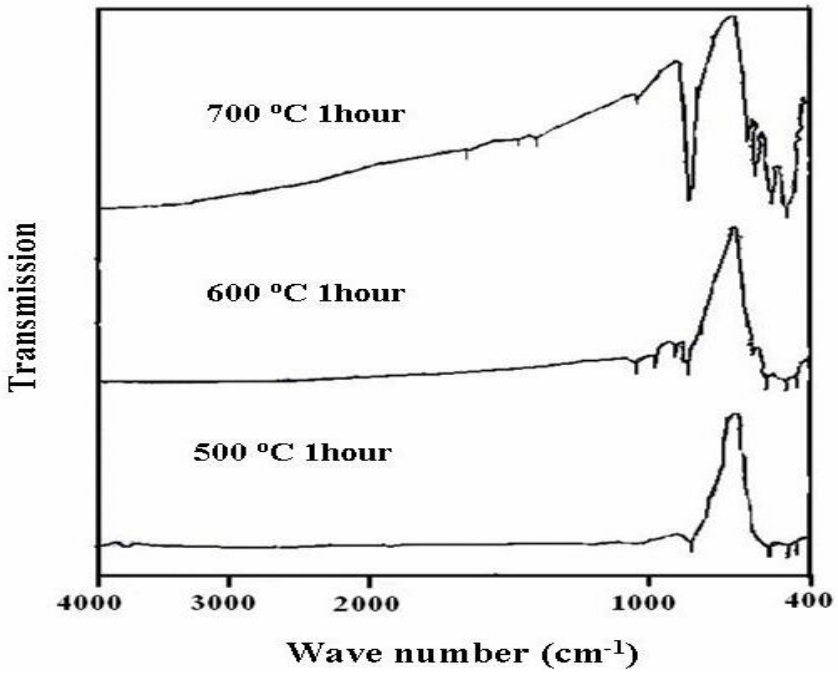

Figure 3.3 *FTIR spectrum of BSO precursor powders calcinied at 500, 600 and 700 ºC*

Table 3.1 lists all the modes observed in FTIR spectrum and compares them with that of literature [16,28]. The peaks observed match well the literature [16,28]. The characteristic peaks of sillenite phase at 474, 532, 576 and 831 cm^{-1}, corresponding to Bi–O and SiO_4 vibration modes, as reported by Vasconcelos *et al*. [16] confirmed the presence of single phase of nanopowders. It should be noted that the FT-IR absorption mode at 817 cm^{-1} was not identified in the work of Burattni *et al* [28]. One possible reason is that BSO samples were powdery polycrystalline materials. We have indicated the positions of the prominent peaks, which belongs to the sillenite phase.

Table 3.1 Comparison of the IR peaks observed in our work with that reported in the literature.

IR peaks observed in this work (cm^{-1})	From Ref. 16 for BSO (54 hours) (cm^{-1})	From Ref. 28 for BSO (54 hours) (cm^{-1})
474	473	453
532	527	526
576	575	580
831	836	833
---	901	---
1018	---	---
1390	1342	1375
1462	1400	1415
1653	1653	1650

3.3.4 Raman spectroscopy

Raman spectra were recorded using 633 nm radiation from the He-Ne laser as excitation source. The group theory analysis predicts that there are 8A (totally symmetric), 8E (doubly degenerate) and 24F (triply degenerate) zone-center optical phonons for the sillenite structure. The spectrum of BSO powders can be separated into two distinct regions. Raman spectrum of sillenite compounds, low frequencies (below 200 cm^{-1}) Raman bands are very sharp, high frequency (above 200 cm^{-1}) Raman bands are quite broad. This is interpreted in terms of an orientational disorder of the lone-pair bonding orbital of Bi^{3+} in the bismuth-oxygen framework. Although an isolated regular tetrahedron, MO_4 exists in the structure, internal modes from the tetrahedron are identified. The main contribution to the vibrational spectrum of sillenites in the region below 650 cm^{-1} is due to the bismuth-oxygen sublattice above 650 cm^{-1} is due to tetrahedron (MO_4). The Raman intensities of the lines corresponding to the vibrations of the bonds in (MO_4) are weaker than the intensities for the lines due to Bi-O vibrations. We observed weak Raman bands at frequencies at 789 and 829 cm^{-1} are belongs to the vibration of tetrahedron. Current assignment for the observed peaks is made based on the detailed Raman study of $Bi_{12}SiO_{20}$ single crystals at low and room temperatures carried out by Venugopalan and Ramdas [29]. Figure 3.4 shows the room temperature micro-Raman spectra of as prepared samples calcined at different temperatures 500, 600, and 700 ºC powders. At 500 and 600 ºC calcined powder's Raman spectrum has α-Bi_2O_3 (monoclinic) and $Bi_{12}SiO_{20}$ phase. At 600 ºC the peaks located at wave numbers, 68, 84, 88, 95, 102, 119.2, 129, 139, 152, 184, 210, 277, 316, 411, 448, 537 and 622 cm^{-1} match with the α-Bi_2O_3 phase [30]. Comparison of

Raman studies with FTIR and XRD confirms the formation of pure phase of BSO at 700 ºC calcination temperature. The Raman spectrum of BSO nanopowders calcined at 700 ºC matches well with that of its single crystal counterpart [31,32]. To the best of our knowledge this is the first report of the Raman spectrum of BSO nanopowders. Table 3.2 shows the comparison of the Raman peaks obtained for nanoparticles with the bulk single crystal counterparts. As prepared BSO nanopowders calcined at 700 ºC were dispersed in PMMA matrix for the nonlinear absorption and scattering measurements. The Raman spectrum of the BSO nanoparticle dispersed in PMMA film shown in figure 3.5(a) & (b) matches quite well with that of the as prepared nanopowders indicating that the nanopartcles retain their crystalline phase in polymer matrix.

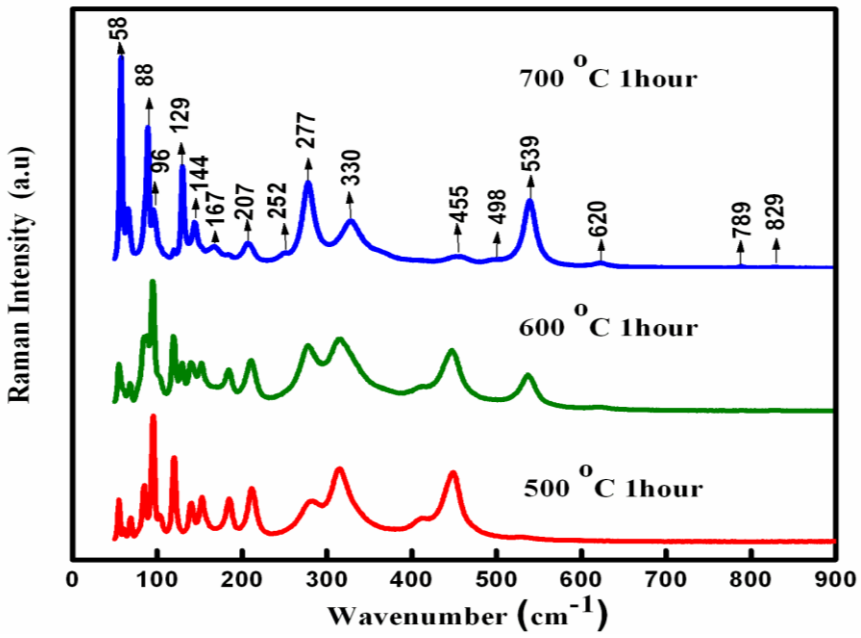

Figure 3.4 *Micro-Raman spectrum of BSO precursor powders calcinied at 500, 600 and 700 ºC.*

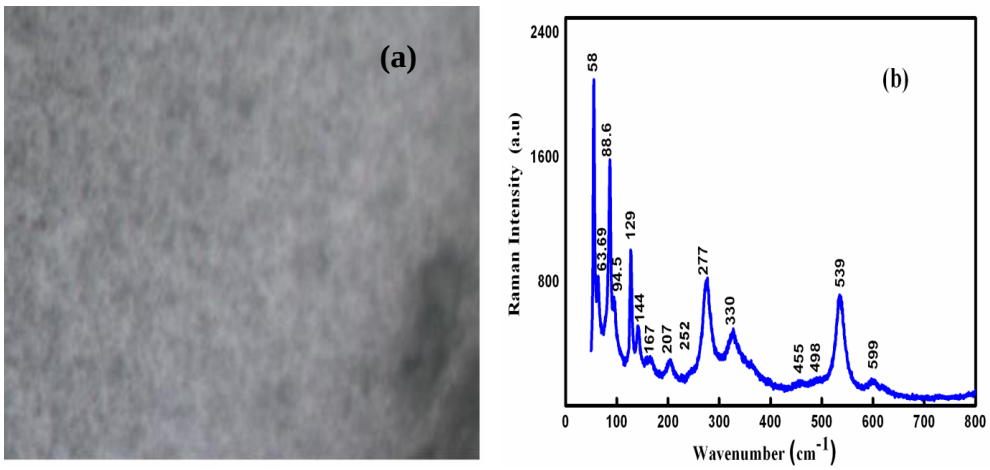

Figure 3.5 *(a) Micro-Raman image of BSO film with 10X objective microscope (b) Raman spectrum of BSO film with 50X objective Microscope.*

Table 3.2 Comparison of the Raman peaks observed in our work with that reported in the literature. (str, bond stretching; bnd, bond bending)

Pure BSO nano powders (cm^{-1})	From Ref#14	From Ref#29	Type of Vibration
829	823	828	Anti-Symmetric stretching of SiO_4 tetrahedra
789	---	789	Symmetric stretching of SiO_4 tetrahedra
620	---	623	O(1) and O(3) vibrations elongating the cluster
539	520	540	"Breathing" of O(1) atoms
498	---	498	Bi-O1 stretching and deformation of SiO_4
455	---	461	O(3)-Si-O(3) bnd, Bi-O(2) str and O(2)-Bi-O(2) bnd, Bi-O(1) str
330	326	328	Bi-O(1) str and O(1)-Bi-O(1)bnd
277	266	278	O(2)-"breathing"
252	---	250	Bi-O(1) str and O(1)-Bi-O(1) bnd, O(3)-Si-O(3)bnd
207	---	208	Bi-O(2) stretching and Bi-O(2)-Bi bending and weak Bi-O(1) rocking
167	---	166	"Breathing" of Bi and all O atoms
144	151	145	"Breathing" of Bi and O(2) atoms
129	125	130	Vibrations of Bi, O(1), O(2) and O(3)
96	---	97	Libration of Bi-O(1) bonds and "breathing" of O(2) atoms
88	81	88	Bi, O(2) and O(3) vibrations elongating the cluster
58	54	57	Bi, O(1) and O(2) vibrations

3.3.5 EPR spectral studies

From EPR experiments one obtains the information on total number of unpaired spins (Ns =1.257×10^{7}) participating in the resonance, g-value (2.01185) and the line widths (101 G). In pure BSO sample only one intense band was observed and no other bands arising from paramagnetic impurity ions such as iron, chromium or manganese were observed at room temperature and as shown in figure 3.6. This band belongs to a center with effective spin of 1/2, such as an electron or hole of oxygen vacancy or a related defect without hyperfine interaction. The measured value of g is 2.0112, which is slightly greater than the free electron value (2.0023). This indicates that this spectrum is due to a hole center. A similar spectrum was observed by Baquedano et al for pure BSO single crystal [33].

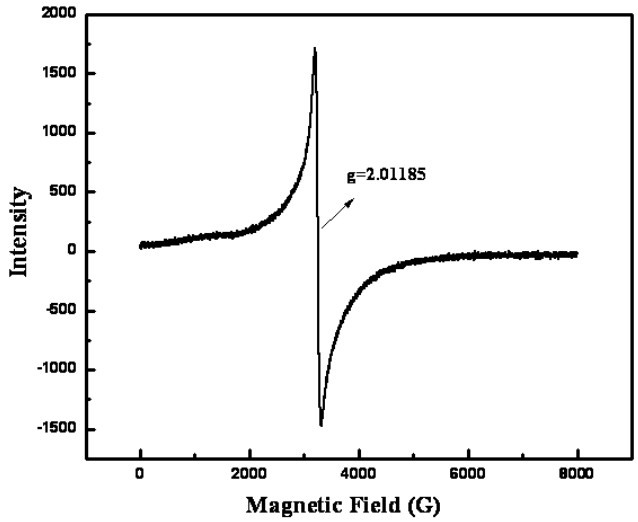

Figure 3.6 *EPR spectrum of as synthesized BSO nanopowders at 700 ºC.*

3.3.6 FE-SEM and TEM studies

FE-SEM-EDX and TEM studies were carried out on the $Bi_{12}SiO_{20}$ powders calcined at 700 ºC for 1 hour. Normalized elemental composition of BSO nanopowders was inferred from the FE-SEM-EDAX studies as shown in figure 3.7. The compositional ratio, as calculated from chemical formula and EDAX analysis, are compared in Table 3.3. From this table it is noted that our sample contains all the compositional elements and there is a difference of about 20% between the calculated value from chemical formula and that from EDAX analysis.

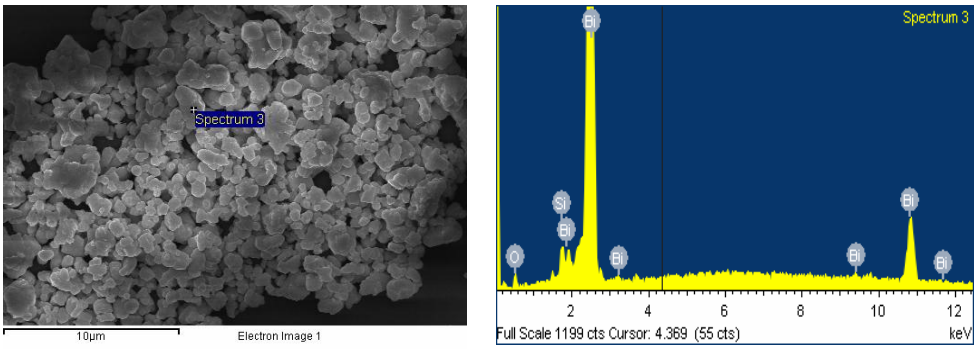

Figure 3.7 *FE-SEM EDAX analysis.*

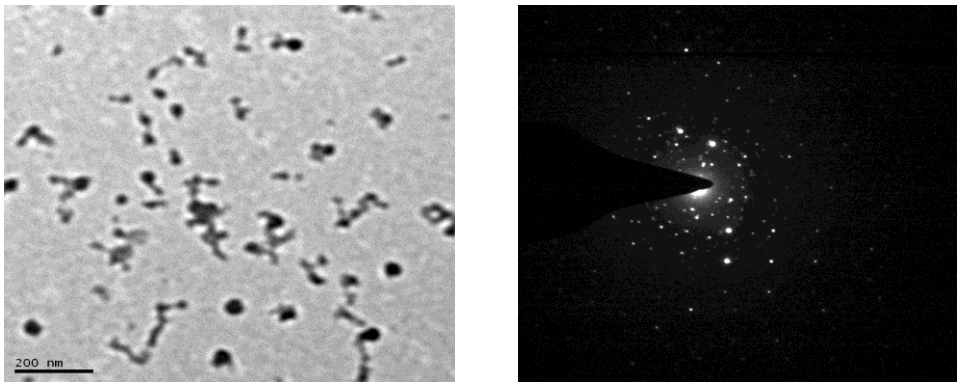

Figure 3.8 *(a) TEM pictures of BSO powders calcined at 700 ºC for 1 h taken at two different areas and (b) its selected area electron diffraction (SAED) pattern.*

We have repeated the experiment at several points with the result of approximately same composition ratio. TEM studies, shown in figure 3.7, were carried out on the BSO powders dispersed in PMMA solution by ultrasonication. This solution was loaded over carbon coated copper grids for recording the TEM. From TEM results the particle size was estimated to be in the 60-150 nm range as shown in figure 3.8 (a) & (b). This particle size through TEM studies differs from that obtained using Scherer's formula from XRD. From the selected area electron diffraction (SAED), the particles were found to be well crystalline as shown in figure 3.8(b).

Table 3.3 *The compositional ratio of $Bi_{12}SiO_{20}$, calculated from chemical formula and EDAX analysis*

Element	From Chemical Formula At%	From EDAX At%
Bi	36.36	29.53
Si	3.03	4.04
O	60.66	66.43

3.3.7 UV-Visible spectroscopy

It is well-known that in nanocrystals, the electronic energy levels are not continuous as in the bulk but are discrete (finite density of states), because of the confinement of the electronic wave function to the physical dimensions of the particles. BSO nanopowders calcined at 700 ºC are dispersed in methanol and ultrasonicated for recording the transmission spectrum. The UV-Visible transmission spectrum of BSO nanocrystals in methanol and 1 mm thick BSO

single crystal as shown in figure 3.9. The transmission spectrum had a dip at ~ 270 nm, indicating that the band gap of the BSO nanocrystals is ~ 4.6 eV, clearly indicating a blue shift in the energy gap compared to that of BSO single crystal ~ 3.25 eV [22,23,34].

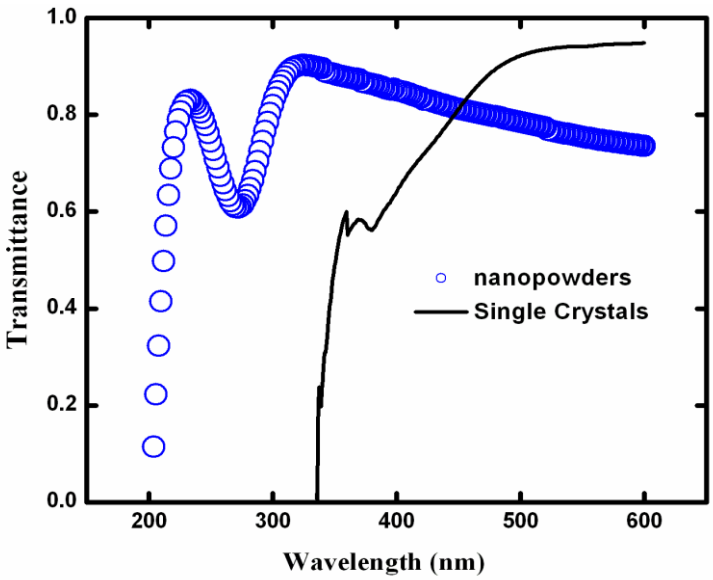

Figure 3.9 *UV-Visible transmission spectrum of BSO nanoparticles calcinied at 700 ºC dispersed in methanol (circles) and of 1 mm thick BSO single crystal (solid line).*

3.3.8 Nonlinear Optical properties

Second harmonic from the Nd: YAG laser with 6 nsec (Spectra-Physics INDI-40) and 30 psec (EKSPLA-PL2143-SH) pulse duration and 10 Hz repetition rate were used as the excitation sources for nonlinear absorption (NLA) and nonlinear scattering (NLS) measurements in the ns and ps regime respectively. The laser pulses were focused onto the sample with a lens of 120 mm focal length with beam waist at focus of 27 μm corresponding to a Rayleigh length of 3–3.8 mm. The film thickness was ~13 μm. It was optically transparent with a very small

absorbance of 0.07 at 532 nm. The thickness of the film is smaller than the Rayleigh length and, hence, the thin sample approximation is valid [35]. The input laser intensity is varied in the range of 0.1–10 $GWcm^{-2}$. Figure 3.10 and 3.11 shows the normalized transmittance of the BSO nanocrystals (normalized with the far-field transmittance) with ns and ps pulse excitations respectively. The Z-scan curves were recorded over different portions of the film in order to ensure the reproducibility of the observed results. PMMA films coated on a glass substrate without BSO nanopowders have shown no measurable nonlinear response under the same excitation conditions in both the ns and ps time regimes. The normalized transmittance at z = 0 of the BSO nanocrystals is ~0.24 at an input intensity of 50 $MWcm^{-2}$ compared to that of 0.7 at an intensity of 204 $MWcm^{-2}$ for 1-mm thick BSO single crystal [18] at ns regime, showing the enhanced NLA of the BSO nanocrystals compared to that of the single crystals.

The nanocrystals showed reverse saturable absorption (RSA) behavior in both temporal regimes within the range of intensities used in the study as shown in figure 3.10 and 3.11. The transmittance has decreases considerably with increasing input laser intensity, indicating a strong nonlinear absorption (NLA) increasing with increasing input intensity. As the incident photon energy corresponding to 532 nm excitation is 2.33 eV, and the band gap of BSO nanoparticles being 4.6 eV corresponding to the absorption peak at 270 nm, resonant two-photon absorption (2PA) appears to be the most plausible absorptive mechanism leading to the observed NLA behavior. Assuming the linear absorption and the resonant two-photon absorption being the only processes, the change in the transmitted intensity through the sample can be given by $dI/dz = -\alpha I - \beta I^2$, where α is the linear absorption co-efficient, β the two-photon absorption co-efficient and I is the intensity of the incident laser

pulse. The normalized transmittance for the standard open aperture Z-scan is expressed by [36]

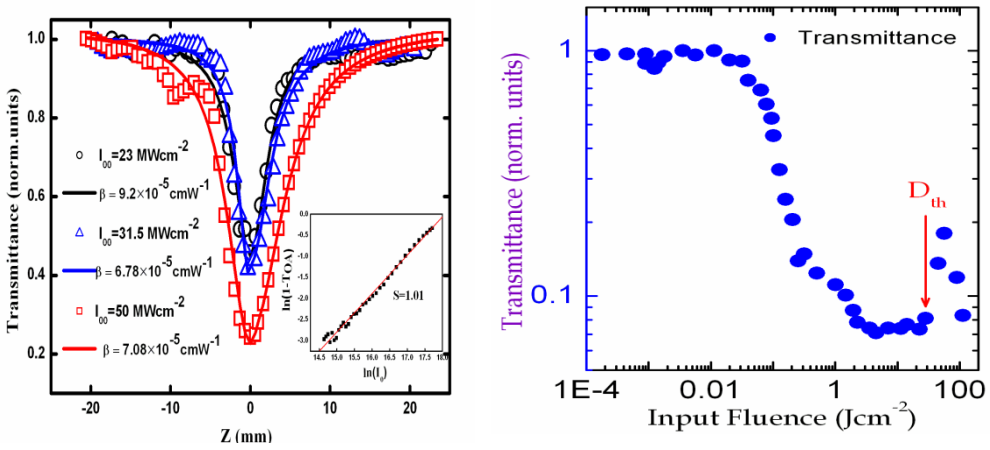

Figure 3.10 *At 532 nm, 6 ns Nd: YAG laser excitation (a) Nonlinear transmittance curves of BSO nanocrystals embedded in PMMA matrix recorded at different input intensities. The lines show the theoretical fits showing the saturation of the two-photon absorption (b) Optical limiting curve of BSO nanocrystals.*

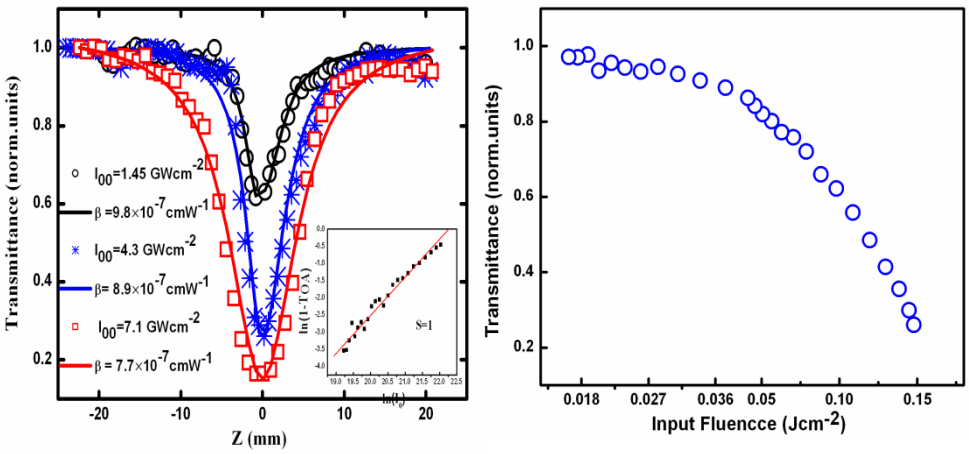

Figure 3.11 *At 532 nm, 30 ps Nd: YAG laser excitation (a) Nonlinear transmittance curves of BSO nanocrystals embedded in PMMA matrix recorded at different input intensities. The lines show the theoretical fits showing the saturation of the two photon absorption. (b) Optical limiting curve of BSO nanocrystals.*

$$T(z, s=1) = 1 - \left[\frac{q_o(z)}{1 + \left(\frac{Iz}{Is} \right)^2} \right] \qquad \text{for } |q_0(0)| < 1, \qquad (3.1),$$

Where $q_o(z) = \beta I_Z L_{eff} / (1 + z^2/z_0^2)$, z_0 being the Rayleigh range of the focused incident laser beam, I_S is the saturation intensity of the excited state. We explored the possibility of fitting the data to different models. A simple 2-photon absorption model gave a very poor fitting. Since there is a resonant two photon absorption, we can expect saturation of the level. The fitting through equation 3.1 assuming TPA and saturation of the level leads to a good fit and the fit indicates that the possible mechanism here is two photon absorption followed by saturable absorption. The inset of the figure. 3.10 & 3.11 show the plot between $\ln(1-T_{OA})$ vs $\ln(I_0)$ with a slope of ~ 1, confirming the presence of a strong two-photon absorption as the major NLA mechanism [24]. The values of β and I_S determined for nano and pico second regime and compared with literature are shown in Table 3.4. The value of β for BSO nanocrystals is found to be four orders of magnitude higher for 6 ns excitation and two orders of magnitude higher for 30 ps excitation when compared to the single crystal data [18,20]. The observed increase in the β can be attributed to the resonant saturable two-photon absorption of the nanoparticles. Table 3.4 compares the β observed in our work with that of metal, semiconductor nanoparticles and that of metalloporphyrins. The observed β is found to be two orders of magnitude higher in ns regime when compared to the earlier studies [26,27,37] while it is comparable to the earlier studies in the ps regime [25,38]. The observed value of β is also found to be higher than that of metalloporphyrins [39], a well known organic molecule for NLO applications.

For the BSO single crystal, the NLA is due to the combination of many processes (a) 2PA between the extrinsic silicon vacancy centre and conduction band (b) valence band and conduction band (c) trap assisted charge carrier absorption from the trap levels arising due to the defects from the crystal growth and (d) the relaxation of the excited charge carriers from the conduction band to different low lying bands [18-20,22]. The intrinsic trapping levels within the energy gap of BSO bulk single crystals are well known to appear due to the complex growth process which leaves vacant sites within the crystal lattice and play a dominant role in the NLA of bulk single crystals in the ns regime [18,22]. However, in the case of BSO nanocrystals, owing to the simple CSD growth, the presence of the intrinsic trap levels will be minimal. And the nano-confinement effect is observed to be dominant in a clear shift of the energy gap localized at 4.6 eV. Clear dominant two-photon absorption (inset of figure 10 & 11) also rules out the contribution from the intrinsic trapping levels to the observed nonlinear absorption mechanism in BSO nanocrystals. Moreover the excitation wavelength (532 nm/2.3 eV) being in two-photon resonance with the band gap (HOMO-LUMO level) confirms the dominant contribution of the TPA to the NLA. The saturation of the nonlinear absorption properties due to resonant excitations has been reported earlier in semiconductors [40-42], nanolayered thin film structures [43] and quantum well structures [44].

In addition to the nonlinear absorption, we observed nonlinear scattering (NLS) in the far-field of the transmitted laser beam in both the ns and ps time regimes. With the 6ns pulse excitation, a good optical limiting response with a limiting threshold of 0.1 Jcm^{-2}, a dominant scattering was observed for fluences greater than 0.3 Jcm^{-2} (50 $MWcm^{-2}$) and the film got damaged at fluences larger than 4 Jcm^{-2}(~600 $MWcm^{-2}$) and as shown in figure 3.10(b). With 30 ps pulse

excitation, a good optical response with a limiting threshold of 0.078 Jcm^{-2} is observed and as shown in figure 3.11(b). However, with 30 ps pulse excitation, the contribution from the nonlinear scattering was observed to be much smaller in comparison to the 6 ns pulse excitation. Figure 3.12 shows the far-field scattering distribution the transmitted light through the film containing BSO nanocrystals observed with 6 ns pulse excitation.

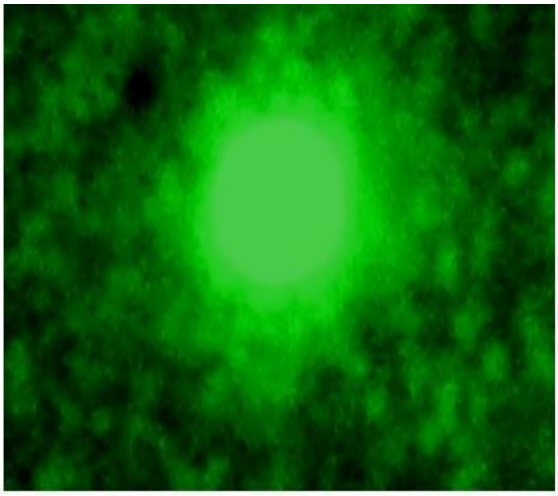

Figure 3.12 *Snapshot of the far-field scattering distribution of the transmitted light through the BSO nanocrystals dispersed in PMMA matrix at higher intensities with 6 ns laser pulse excitation. The central bright portion is mainly due to the reflection from the white paper. Actual intensity at the center is much smaller than that is seen in the picture.*

Table 4. Nonlinear optical characteristics of the BSO film obtained by analysis of the open aperture z-scan using nano and picosecond regime at 532 nm. Effective two

photon absorption coefficients reported in the literature for metal, semiconductor nanoparticles and metalloporphyrins at 532 nm wavelength excitation.

[a]*Effective nonlinear absorption coefficient*

Material	Size (nm)	Laser pulses	I_{00} ($MWcm^{-2}$)	I_s ($MWcm^{-2}$)	[a]β (cmW^{-1})	Ref
BSO (present work)	60–150	6 ns	23	40	9.2×10^{-5}	
,,		6 ns	32	60	6.8×10^{-5}	
,,		6 ns	50	60	7.1×10^{-5}	
,,		30 ps	1.45×10^{3}	3×10^{3}	9.8×10^{-7}	
,,		30 ps	4.3×10^{3}	4×10^{3}	8.9×10^{-7}	
,,		30 ps	7.1×10^{3}	4×10^{3}	7.7×10^{-7}	
CdS	5	6 ns			3.5×10^{-8}	[26]
ZnO/PMMA	10	6–7 ns			6.82×10^{-7}	[37]
Ag/PVP	15–50	38 ps			6.19×10^{-7}	[38]
Sn–Sn(TTP)$_2$		25 ps			1.5×10^{-9}	[39]
BSO single crystal		6 ns			12.42×10^{-9}	[18]
BSO single crystal		55 ps			2×10^{-9}	[20]

As the nanoparticles showed strong nonlinear absorption, the nonlinear refractive index had a strong thermal contribution at higher fluences that

increases with increasing fluence, due to the thermalization of the nanoparticles. Resonant excitation with longer pulses is known to result in thermally induced transient refractive index changes, in turn depending on the thermo-optic co-efficient, the input fluence and the medium density. In the case of nanoparticles, nonlinear scattering phenomenon was proposed to be due to induced pseudo-absorbance leading to the vaporization or fragmentation of the nanoparticles inducing a large light-scattering center around the initial particles. Such vaporization or fragmentation induced by a thermal effect has been reported in nanoparticles earlier [27,44-50]. In case of nanoclusters suspended in solutions, at high fluences the scattering centers produce more numerous fragments confined in the same scattering center. This increases the probability of recombination with the solvent and a more efficient cooling of the scattering centers. Such effects can be efficient in case of nanoclusters in solution state, where as in thin films such a process can lead to an irreversible damage, which was observed at higher fluences. As the preparation of thick films containing uniformly dispersed nanoparticles is a challenge in itself, nanoparticles in solution state would be ideal candidates for NLS purposes at lower input fluences. Nanoclusters dispersed in viscous solutions or polymer solutions may offer better NLS and provide advantage offered by both solution state and films.

3.4 Conclusions

$Bi_{12}SiO_{20}$ nanocrystals with perfect sillenite structures were prepared by a simple CSD method. XRD, micro-Raman and FTIR studies suggest that crystalline sillenite phase of BSO is forming at a temperature of 700 °C. Open aperture Z-scan experiments reveal large two photon saturable absorption coefficient of the order of 10^{-5} cm/W and 10^{-7} cm/W at nano and picosecond regime due to nanosize effect. BSO nanocrystals show two orders of

enhancement in nonlinear absorption properties compared to that of bulk single crystals, metal, and semiconductor nanoparticles and are also larger than the well known organic molecules.

3.5 References

1. C.N.R. Rao, F.L. Deepak, G. Gautam, A. Govindaraj, Prog. *Solid State Chem.* 31 (2003) 5.
2. M. Willander, O. Nur, Q.X. Zhao, L.L. Yang, M. Lorenz, B.Q. Cao, J. Zuniga Perez, C. Czekalla, G. Zimmermann, M. Grundmann, A. Bakin, A. Behrends, M. Al-Suleiman, A El-Shaer, A. Che Mofor, B. Postels, A. Waag, N. Boukos, A Travlos, H.S. Kwack, J. Guinard, D. Le Si Dang, *Nanotechnology* 20 (2009) 332001.
3. Y. Deng, J. Zhou, D. Wu, Y. Du, M. Zhang, D. Wang, H. Yu, S. Tang, Y. Du, *Chem. Phys. Lett.* 496 (2010) 301.
4. A.V. Egorysheva, T.I. Milenov, P.M. Rafailov, C. Thomsen, R. Petrova, V.M. Skorikov, M.M. Gospodinov, *Solid State Commun.* 149 (2009) 1616.
5. S.C. Abrahams, P.B. Jamieson, J.L. Bernstein, *J. Chem. Phys.* 47 (1967) 4034.
6. C. Wang, C. Shao, L. Wang, L. Zhang, X. Li, Y. Liu, *J. Colloid Interface Sci.* 333 (2009) 242.
7. T.P. Gujar, V.R. Shinde, C.D. Lokhande, Sung-Hwan Han, *Mater. Sci. Eng., B* 133 (2006) 177.
8. K. Kim, J.H. Park, S.G. Doo, T. Kim, *Thin Solid Films* 518 (2010) 6547.
9. G. Zhu, X. Zou, J. Cheng, M. Wang, Y. Su, *Solid State Commun.* 148 (2008) 243.

10. R. Sharma, D.V. Sridhara Rao, V.D. Vankar, *Mater. Lett.* 62 (2008) 3174.
11. R. Chen, J. Bi, L. Wu, W. Wang, Z. Li, X. Fu, *Inorg. Chem.* 48(19) (2009) 9072.
12. R. Chen, J. Bi, L. Wu, Z. Li, X. Fu, *Cryst. Growth Des.* 9(4) (2009) 1775.
13. X. Zhu, J. Zhang, F. Chen, *Chemosphere* 78 (2010) 1350.
14. I.V. Kityk, A. Majchrowski, J. Ebothe, B. Sahraoui, *Opt Commun.* 236 (2004) 123.
15. I.V. Kityk, A. Majchrowski, B. Sahraoui, *Optics and Lasers in Engg.* 43 (2005) 75.
16. I.F. Vasconcelos, M.A. Pimenta, A.S.B. Sombra, *J. Mater. Sci. Lett.* 36 (2001) 179.
17. J.C. Alonso, R. Diamant, E. Haro-Poniatowski, M. Fernandez-Guasti, G. Munoz, I. Camarillo, M. Jouanne, J.F. Morhange, *Appl. Surf. Sci.* 109/110 (1997) 359.
18. D. Narayana Rao, P. Prem Kiran, *Nonlinear Opt.* 27 (2001) 347.
19. P.S. Aithal, P. Prem Kiran, D. Narayana Rao, *J. Nonlinear Opt. Phys. Mater.* 9(2) (2000) 217.
20. R.A. Ganeev, A.I. Ryasnyansky, R.I. Tugushev, M.K. Kodirov, F.R. Akhmedjanov, T. Usmanov, *Opt. Quantum Electron.* 36 (2004) 807.
21. R.A. Ganeev, A.I. Ryasnyansky, B. Palpant, S. Debrus, *J. Appl. Phys.* 97 (2005) 104303.
22. I.V. Kityk, M.K. Zamorskii, J. Kasperczyk, *Physica B* 226 (1996) 381.
23. S.L. Hou, R.B. Lauer, R.E. Aldrich, *J. Appl. Phys.* 44(6) (1973) 2652.
24. A.D. Lad, P. Prem Kiran, D. More, G. Ravindra Kumar, S. Mahamuni, *Appl. Phys. Lett.* 92 (2008) 043126.

Chapter 3

25. A. Nag, Akshay Kumar, P. Prem Kiran, S. Chakraborty, G. Ravindra Kumar, D. Sarma, *J. Phys. Chem. C* 112 (2008) 8229.
26. N. Venkatram, M.A. Akundi, D. Narayana Rao, *Opt. Express* 13 (2005) 867.
27. P. Prem Kiran, B.N. ShivaKiran Bhakta, Goutam De, D. Narayana Rao, *J. Appl. Phys.* 96 (2004) 6717.
28. E. Burattini, G. Cappuccio, M.C. Ferrari, M. Grandolfo, P. Vecchia, S.H.M. Efendiev, *J. Opt. Soc. Am. B* 5 (1988) 7149.
29. S. Venugopalan, A.K. Ramdas, *Phys. Rev. B* **5** (1972) 4065.
30. A.J. Salazar-Pérez, M.A. Camacho-López, R.A. Morales-Luckie, V. Sánchez-Mendieta, F. Ureña-Núñez, J. Arenas-Alatorre, *Superficies y Vacío* 18(3) (2005) 4.
31. B. Mihailova, M. Gospodinov, L. Konstantinov, *J. Phys. Chem. Solids* 60 (1999) 1821.
32. R.N. Panda, A. Pradhan, Mater. *Chem. Phys.* 78 (2002) 313.
33. J.A. Baquedano, F.J. Lopez , J.M. Cbrera, *Solid State Commun.* 72(3) (1989) 233.
34. E.V. Mokrushina, M.A. Bryushinin, V.V. Kulikov, A.A. Petrov, and I.A. Sokolov, *JOSAB* 16 (1999) 57.
35. M. Sheik-Bahae, A.A. Said, T. Wei, D.J. Hagan, E.W. Van Stryland, *IEEE J. Quantum Electron.* 26(4) (1990) 760
36. G.S. He, Q. Zheng, A. Baev, P.N. Prasad, *J. Appl. Phys.* 101 (2007) 083108.
37. R. Sreeja, Jobina John, P.M. Aneesh, M.K. Jayaraj, *Opt. Commun.* 283 (2010) 2908.
38. T. He, C. Wang, X. Pan, Y. Wang, *Phys. Lett. A* 373 (2009) 592.

39. P. Prem Kiran, D. Raghunath Reddy, B.G. Maiya, A.K. Dharmadhikari, G. Ravindra Kumar, D. Narayana Rao *Opt. Commun.* 252 (2005) 150.
40. J.F. Lami, P. Gilliot, C. Hirlimann, *Phys. Rev. Lett.* **77** (1996) 1632.
41. B. Gu, J. He, W. Ji, H. Wang, *J. Appl. Phys.* 103 (2008) 073105.
42. B. Gu, Y. Fan, J. Chen, H. Wang, J. He, W. Ji, *J. Appl. Phys.* 102 (2007) 083101.
43. K.V. Adarsh, K.S. Sangunni, C.S. Suchand Sandeep, R. Philip, S. Kokenyesi, V. Takats, *J. Appl. Phys.* 102 (2007) 026102.
44. D.N. Christodoulides, Iam Choon Khoo, G.J. Salamo, G.I. Stegeman, E.W. Van Stryland, *Advances in Opt. and Photonics* 2 (2010) 60.
45. S. Link, M.A. El-Sayed, *J. Phys. Chem. B* 103 (1999) 8410.
46. A. Takami, H. Kurita, S. Koda, *J. Phys. Chem. B* 103 (1999) 1226.
47. H. Fujiwara, S. Yanagida, P.V. Kamat, *J. Phys. Chem. B* 103 (1999) 2589.
48. G.S. Maciel, N. Rakov, Cid B. de Araújo, *Opt. Lett.* 27(9) (2000) 740.
49. L. Francois, M. Mostafavi, J. Belloni, J.F. Delouis, J. Delaire, P. Feneyrou, *J. Phys. Chem. B* 104 (2000) 6133.
50. P. Prem Kiran, S. Venugopal Rao, M. Ferrari, B.M. Krishna, H. Sekhar, S. Alee, D. Narayana Rao, *Nonlinear Opt. Quantum Opt.* 40 (2010) 223.

Chapter 4

Preparation, characterization and nonlinear optical absorption studies in Cu_2O nanomorphologies

Abstract

In this chapter we discussed about the preparation, characterization and nonlinear optical properties of cuprous oxide with different nano morphologies. Cuprous oxide nano clusters, micro cubes and micro particles were successfully synthesized by reducing copper (II) salt with ascorbic acid in the presence of sodium hydroxide via a co-precipitation method. As synthesized powders were characterized by using different spectroscopic techniques, and shows the presence of CuO in as-synthesized powders of Cu_2O. Linear optical measurements shows absorption peak maximum shifts towards red with changing morphology from nano clusters to micro cubes and micro particles. The nonlinear optical properties were studied using open aperture Z-scan technique with 532 nm 6ns and 30ps laser pulses. Samples exhibited both saturable as well as reverse saturable absorption. Due to confinement effects (enhanced band gap) we observed the enhanced nonlinear absorption coefficient (β) in the case of nano-clusters compared to their micro-cubes and micro-particles.

The results of this chapter are published in

J. Nanoparticle Research 14 (2012) 976 *"Preparation, characterization and nonlinear absorption studies of cuprous oxide nanoclusters, micro-cubes and micro-particles"* by **H. Sekhar** and D. Narayana Rao

Chapter 4

4.1 Introduction

Cuprous (Cu_2O) and cupric (CuO) oxides (cuprite and tenorite, respectively) are the two most important stoichiometric compounds in the copper-oxygen (Cu-O) system. Both materials are intrinsic p-type semiconductors with narrow energy band gaps (2.1 eV for Cu_2O, 1.2 eV for CuO). Metal oxides like Cu_2O with well-controllable size and shape at the nano/micrometer dimensions have received increasing attention in current material synthesis and devices fabrication. Many fields including, solar cells [1], catalysis [2], lithium ion batteries [3] and sensors [4,5] could greatly benefit from advances in the synthesis of well-defined nanostructures. It is also an ideal compound used as a dilute magnetic semiconductor (DMS) [6]. It is also found to be a stable photocatalyst for splitting water for hydrogen generation or degradation of organic contamination [7,8]. Cu_2O is low cost, with low toxicity and the natural abundance of its source materials favors the fundamental and practical research on Cu_2O. Cu_2O is a p-type semiconductor having simple and highly symmetric cuprite structure (space group O_h) with six atoms in a unit cell and a direct band gap of about 2.1 eV with high optical absorption coefficient, making it a promising material for low-cost photovoltaic applications and the conversion of solar energy into electrical or chemical energy [9]. Engineering the band gap and influencing the physical, chemical and electronic properties of the semiconductors are possible by the use of changing particle size from nano to even submicron scale or doping with transition metal ions [9-11]. Spacing between nano morphologies is also important factor influencing its physical properties [12]. This would lead to properties that are different from those of their bulky counterparts and makes them candidates for various important applications in the field of material research. For photonic applications, materials with tunable optical responses over broad spectral ranges are highly

desirable in many cases, and how to achieve such optical tunability is been a key challenging issue.

X-ray diffraction studies on Cu_2O shows the formation of single phase cubic but XPS studies shows CuO phase forming on the surface of Cu_2O [13]. Borgohain et al [14] reported that Cu_2O phase stabilized by a controlled oxidation and the formation of a thin protecting film of CuO. Bulk Cu_2O is a diamagnetic material at room temperature. Recent studies have shown that nanoparticles of non-stoichiometric Cu_2O_{1+x} of size 15 nm exhibit a hysteresis loop at low temperatures. The weak ferromagnetism of Cu_2O nanoparticles is ascribed to the presence of Cu^{2+} in the nonstoichiometric composition [15]. The size dependent ferromagnetic properties of Cu_2O nanoparticles capped with glucose, show super paramagnetic behavior with increased magnetization as well as coercivity with decreasing particle size [16].

Intense research is currently being pursued in the field material preparation, characterization and its linear, nonlinear optical properties of nanoparticles by various laboratories, motivated by the fundamental question of how the material properties evolve with size. Nonlinear interaction of electromagnetic radiation with matter can induce various nonlinear optical effects, in particular, related to optical switching [17], fluorescence imaging [18], up-conversion [19] and optical limiting [20]. To find the nonlinear optical parameters such as nonlinear absorption (NLA) and nonlinear refraction (NLR), we utilized the standard Z-scan technique, which is a simple single beam nonlinear transmission experiment [21]. Most of the materials will show two types of nonlinear absorptions, i.e. saturable absorption (SA) or reverse saturable absorption (RSA). SA types of materials are used for optical pulse compression, optical switching and laser pulse narrowing. RSA types of materials are used as optical limiters to protect eyes and sensors against the

damage of exposure to sudden high-intensity light and it still remain a challenging problem. The selection of efficient materials is still the key point for optical power limiters and it has led to the study of materials that exhibit strong two photon or excited state absorption [22].

4.2 Experimental Section

4.2.1 Preparation method

It is still a challenge for chemists and material scientists to find some convenient, economical, less energy consuming and environmentally friendly synthesized routes to these semiconductor nanocrystals. Synthesis of inorganic nanoparticles still remains a challenging task owing to intrinsic difficulties in the control of composition and morphology. Cu_2O powders with tunable linear and nonlinear optical properties have been successfully synthesized by a simple co-precipitation technique by varying NaOH concentration. Nanoclusters, micro cubes and micro particles were obtained by slightly modifying the preparation conditions given by Zhang et al [8]. By reducing copper (II) salt with ascorbic acid in the presence of sodium hydroxide. In the typical synthesis, $CuSO_4$. $5H_2O$ (2.5g) was dissolved in milli Q water (20ml). Then NaOH (0.8g, 0.5 $molL^{-1}$) was dissolved in 40 ml milli Q water and added to the 20 mL aqueous solution of $CuSO_4$ by constant stirring. A blue $Cu(OH)_2$ precipitate appeared immediately. Then 0.88 g ascorbic acid dissolved in 50 mL milli Q water was added drop wise to the above solution with vigorous stirring at room temperature. After 60 minutes of stirring, the precipitate particles were isolated from the solution by centrifugation at 2000 rpm for 15 min. The product was washed by milli Q water and absolute ethanol through multiple cycles of centrifugation and redispersion. The final product was dried in silicon oil bath at 80 °C for 7 hours. In the preparation process, morphology and color of the

particles strongly depends on the NaOH concentration. 0.5 M NaOH gives yellow nanoparticles, 0.75 M leads to orange yellow micro-cubes and for 1M or above 1M, the product gives light brick red micro-particles. The sample codes of the Cu_2O powders obtained by varying the concentration of NaOH as 0.5, 0.75, and 1.5 M are referred as Cu_2O-I, Cu_2O-II, and Cu_2O-III respectively.

4.3 Results and Discussion

4.3.1 X-ray powder diffraction studies

The structural and phase purity of as synthesized Cu_2O powders studied by X-ray powder diffraction technique and the XRD pattern is shown in figure. 4.1. Diffraction peaks of all the samples could be assigned to the crystalline cuprous oxide in a cubic structure with a space group Pn3m (a body centered cubic packing of oxygen atoms with copper atoms occupying one-half of the tetrahedral sites). No impurity phase such as CuO could be detected in this pattern, indicating that a pure phase of cuprous oxide can be readily synthesized. XRD data were analyzed by XRDA software. Table 4.1 showing the lattice parameters for all samples, was calculated from the XRDA software and is compatible with the literature standard values (standard JCPDF file no. 05-0667). A change in color from yellow to brick red with increasing the concentration of NaOH from 0.5 to 1.5 M could also be seen through the peak narrowing indicating particle size increase. The average grain size of Cu_2O-I (0.5M), was calculated using the (111) diffraction peak as reference according to the Scherrer's formula. The average grain size was found to be around 20 nm.

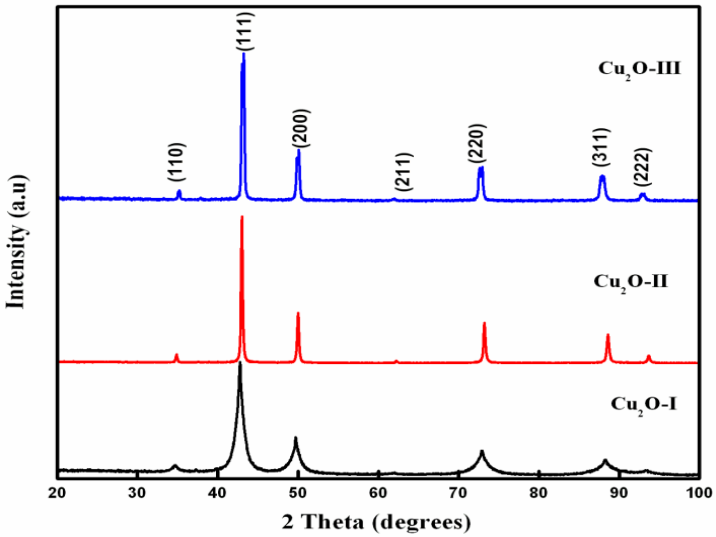

Figure 4.1 *XRD pattern of as synthesized Cu_2O powders at different NaOH concentrations.*

Table 4.1 *Lattice parameter of Cu_2O powders with different morphologies.*

Sample code	Lattice parameter "a" (Å)
Cu_2O – I	4.2242
Cu_2O – II	4.2584
Cu_2O – III	4.2599

4.3.2 FTIR

Metal oxide generally gives absorption bands below 1000 cm^{-1} that arise from interatomic vibrations. Infrared spectra of the samples prepared with different NaOH concentration is as shown in figure 4.2. In the higher energy region the broad peak at 3420 cm^{-1} is assigned to O-H stretching of absorbed water on the surface of Cu_2O. The presence of water is confirmed by its bending vibration at

1625 cm^{-1}. Bands at 1130, 798 and 621 cm^{-1} are attributed to the stretching of copper (I)-O in Cu_2O [23].

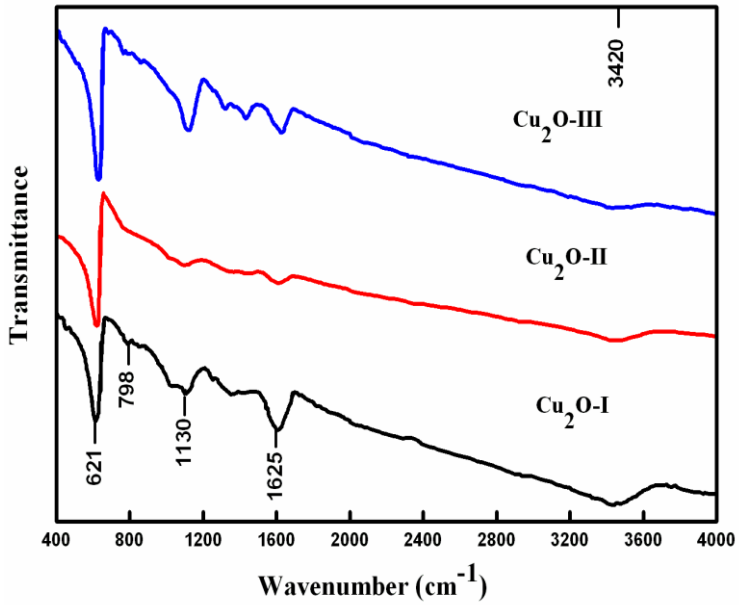

Figure 4.2 *FTIR spectrum of as synthesized Cu_2O powders at different NaOH concentrations.*

4.3.3 Raman Studies

The surface to volume ratio increases for a nanoparticle, Raman scattering can provide information on the surface vibrational states of the nanocrystals. The Raman spectrum of the as synthesized powders is shown in figure 4.3. The peaks at 218, 620 cm^{-1} are assigned Cu_2O phase, whereas the peak at 280 cm^{-1} belongs to CuO phase [24].

The X-ray powder diffraction studies on Cu_2O powders shown in figure 4.1 do not show the peaks of CuO phase. Hence from the Raman peak at 280 cm^{-1} belonging to CuO and the XRD spectrum showing only the peaks belonging to the pure Cu_2O single phase, we conclude that as synthesized

nanopowders consists of multiple phases like Cu_2O and CuO. Earlier reports using X- ray photoelectron spectroscopy (XPS) technique show that CuO phase is present on Cu_2O nanoparticles as a surface layer [13,14].

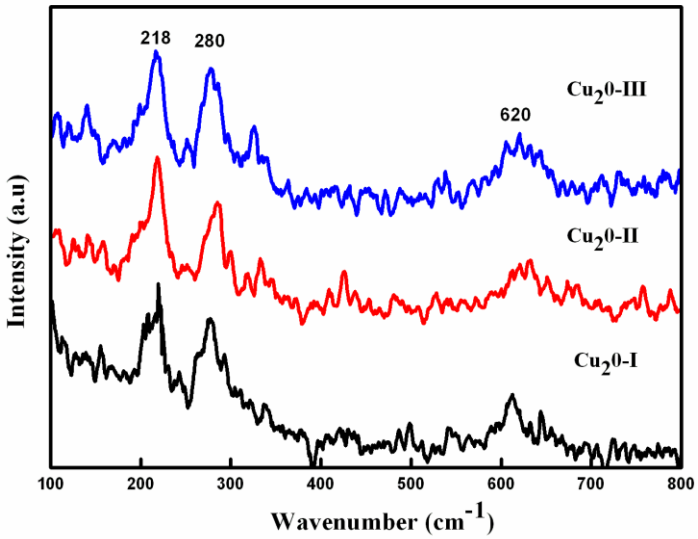

***Figure** 4.3 Raman spectrum of as synthesized Cu2O powders at different NaOH concentrations.*

4.3.4 EPR

The phase purity of as-synthesized Cu_2O powders was further examined by EPR technique and is shown in figure 4.4. Cu_2O is expected to have an essentially full Cu 3d shell. Cu^{+2} ions have an electron configuration of d^9 and are paramagnetic over a wide range of temperatures. At room temperature, the observed resonance signal is assigned to the paramagnetic Cu^{+2} ion [25]. The broadness of the resonance peak is attributed to the superposition of closely-spaced peaks of Cu^{+2} ion. Table. 4.2 show the observed g value which is characteristic of d^9-Cu (II) cation. In the as synthesized powders, some of the unreacted Cu^{2+} species reacts with oxygen forming CuO. Raman and EPR

studies show that CuO is present in as synthesized Cu_2O powders. SAED and XRD studies show only Cu_2O phase, which means that CuO could be in the non-crystalline form [14]. From these results we conclude that the as synthesized nanopowders consist of multiphase like Cu_2O and CuO.

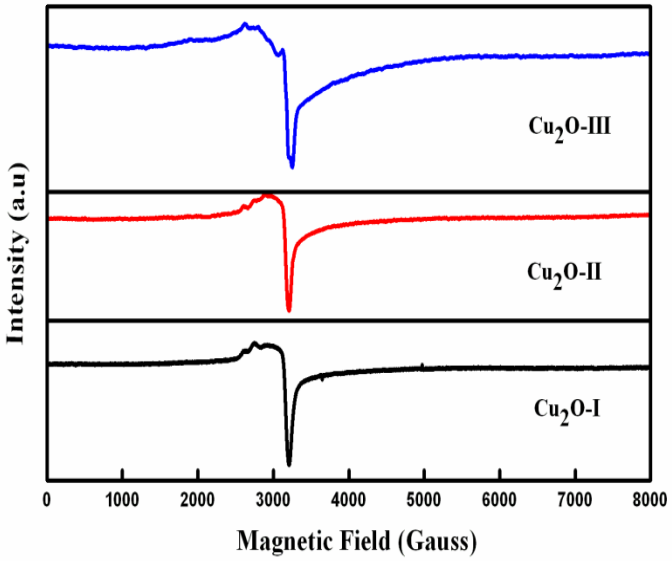

Figure 4.4 *EPR spectrum of as synthesized Cu_2O powders at different NaOH concentrations.*

Table 4.2 *Calculated g values of Cu_2O nanopowders from EPR spectra.*

Sample	g value		
	Cu_2O-I	Cu_2O-II	Cu_2O-III
Cu_2O	2.12367	2.15617	2.17815

4.3.5 UV-Visible absorption spectra

The optical absorption spectra of as prepared Cu_2O powders of different sizes are recorded by dispersing them in iso-propanol by ultrasonication for 15 minutes are shown in figure 4.5. The samples were synthesized several times and they all show an identical absorption spectrum. UV-Vis absorption spectra of Cu_2O-I, Cu_2O-II are broad and have multiple peaks. The spectra were deconvoluted to three Gaussian functions with maxima at 329, 474 and 547nm for the Cu_2O-I, and peaks at 353, 540 and 673nm for the Cu_2O-II. The peak at 474 nm in Cu_2O-I and the peak at 540 nm in Cu_2O-II are attributed to the band-to-band (band gap) transition in the nanocrystalline Cu_2O [14]. Peak at 547nm in Cu_2O-I and peak at 673nm in Cu_2O-II belongs to surface defects (CuO) [14,26]. A spectrum of Cu_2O-III has a very broad absorption band in the longer wavelength region. Cu_2O-I, Cu_2O-II and Cu_2O-III are direct band gap materials [27], and their calculated optical band gaps are 2.6, 2.3 and 2.1 eV respectively. Cu_2O-I (2.6 eV) optical band gap shifts towards higher energy (blue shift) compared to the bulk Cu_2O band gap at 2.1 eV. The confinement of charge carriers (electron or hole) in a restricted volume of small particles leads to splitting of continuum of electronic energy levels into discrete states with the effective band gap energy blue shifted from that of the bulk due to quantum confinement. The increase in band gap with decreasing particle size is due to quantum size effect. The observed spectrum matches well with the earlier reported Cu_2O spectrum [28,29].

Another prominent feature in the absorption profiles of the Cu_2O-III samples is the appearance of one or multiple absorption bands in the red and near-infrared (NIR) regions. Such a feature has been previously reported in Cu_2O micro-cubes [30] with a dimension of hundreds of nanometers to a few micrometers.

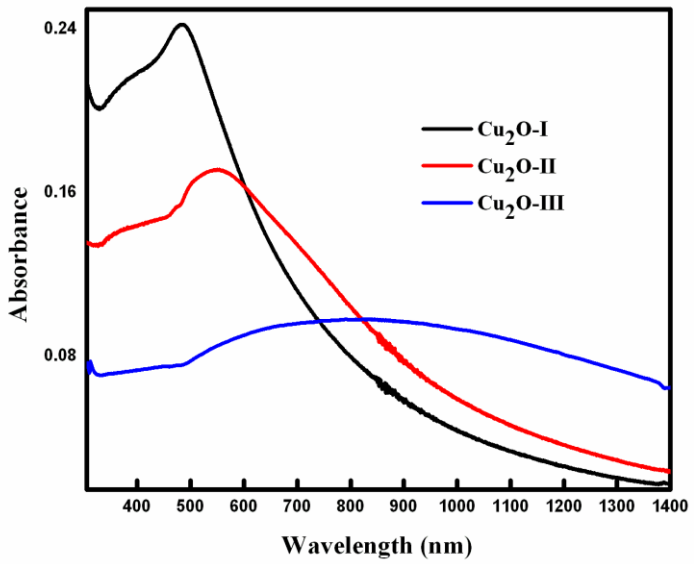

Figure 4.5 *UV-Vis absorption spectrum of as synthesized Cu_2O powders at different NaOH concentrations.*

4.3.6. FE-SEM EDAX, TEM Analysis

Particle crystallinity, powder morphology, elemental analysis, and stoichiometric ratio of freshly prepared Cu_2O powders were inferred from TEM, FE-SEM-EDAX studies. Figures 4.6, 4.7 and 4.8 shows a set of typical FE-SEM and TEM images of Cu_2O powders dispersed in iso-propanol with 15 minutes ultrasonication. Figure 4.6(a) & (b) shows FE-SEM images of Cu_2O-I at lower and higher magnification. At lower magnification (figure 4.6(a)) the particles appear to be in microns (100-150nm). At higher magnification (figure 4.6(b)) the particles were very small with size varying between 15-20nm and agglomerated with 100 to 150nm size. To confirm this we carried out TEM analysis and as shown in figure 4.6(c). From FE-SEM and TEM analysis we conclude that Cu_2O-I particle size varies from 15-20nm.

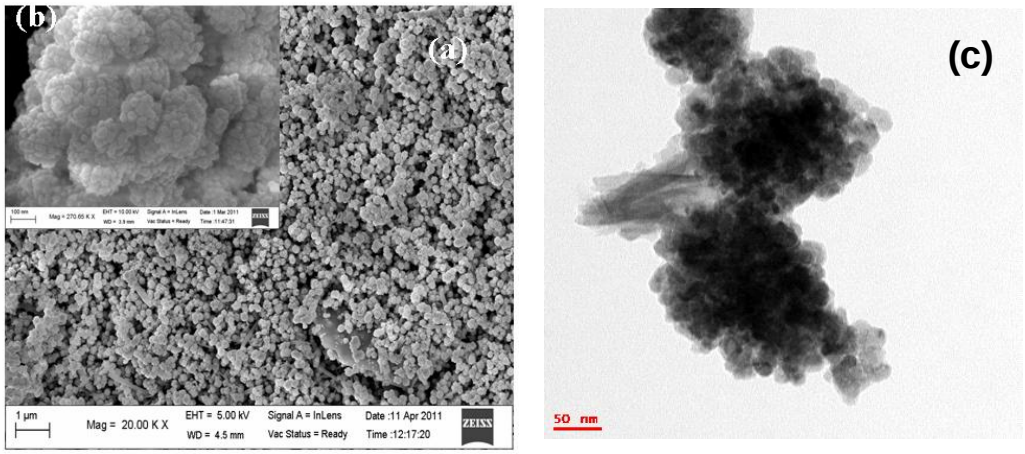

Figure 4.6 *(a&b) FE-SEM Cu_2O-I powders with lower and higher magnification (c) TEM image of Cu_2O-I powders.*

Figure 4.7(a&b) shows the FE-SEM images and figure 4.7(c&d) shows the TEM images of Cu_2O-II powder. Cu_2O-II powder morphology indicates that it is an aggregation of many cubes with varying sizes from 100-150nm. Figure. 4.8 shows FE-SEM images of Cu_2O-III powders, are in micron size. Above result clearly shows that the size and shape of Cu_2O powders can strongly depend on the NaOH concentration. It is concluded by several authors, that the preferential absorption of molecules and ions in solution to different crystal faces makes nanoparticles grow into various shapes [31,32]. In case of Cu_2O-II, OH^- ions affect the stability of {100} leading to a cubic morphology [8].

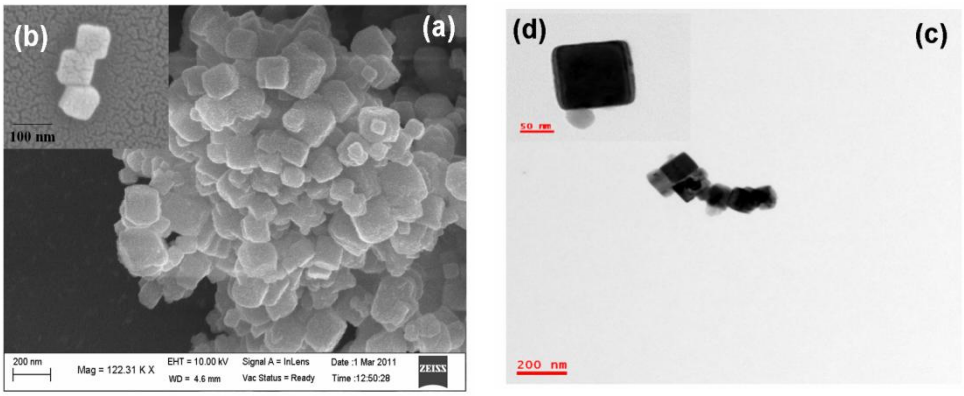

Figure 4.7 *(a&b) FE-SEM images of Cu_2O-II powders with lower and higher magnification (c&d) TEM image of Cu_2O-II powders with lower and higher magnification*

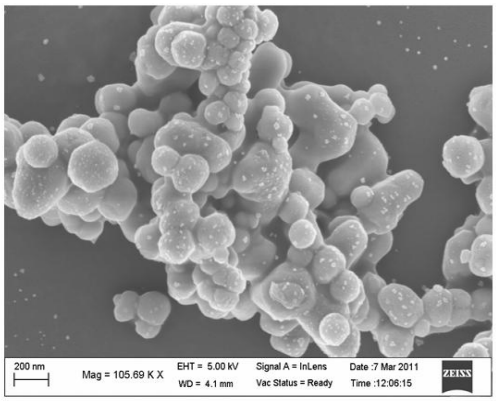

Figure 4.8 *FE-SEM images of Cu_2O-III powders*

Figure 4.9 shows high resolution TEM images of Cu_2O nano-clusters and micro-cubes, exhibits visible lattice fringes with interplanar spacing of 0.25 nm, corresponding to (111) reflection of the cubic crystal structure of Cu_2O. Figure 4.10(a),(b)&(c) show selected area electron diffraction SAED patterns of Cu_2O-I, Cu_2O-II and Cu_2O-III powders. From figure 4.10(a) one can observe the concentric ring structure in the SAED pattern, clearly verified the

polycrystalline nature of the Cu_2O-I. This SAED pattern completely indexed as lattice planes of cubic Cu_2O (standard JCPDF file no. 05-0667), which is in good agreement with the XRD pattern. Raman and ESR studies show that CuO phase is present in as synthesized powders. From XRD and SAED pattern we conclude that CuO may be present in non-crystalline form (Borgohain et al 2002). For EDAX analysis Cu_2O powder mounted on double-sided carbon tape and gold (Au) coating was done for 60 sec to avoid specimen's charging. The observed data is shown in figure 4.11. The compositional ratio of as synthesized powders is shown inset of figure 4.11. From this compositional analysis we conclude that our samples do not show any trace of elements other than copper and oxygen and their elemental ratio is ~2:1.

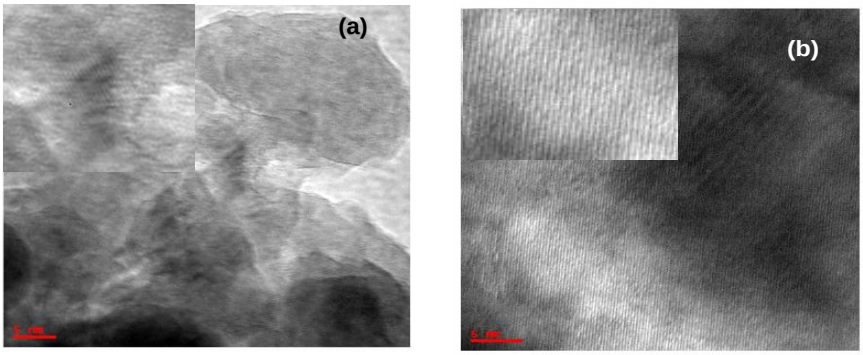

Figure 4.9 *HR-TEM pattern of (a) Cu_2O-I and (b) Cu_2O-II*

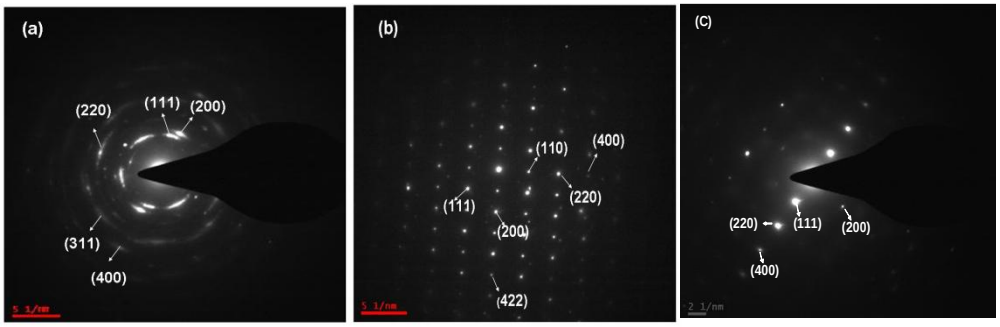

Figure 4.10 *SAED patterns of (a) Cu_2O-I (b) Cu_2O-II and (c) Cu_2O-III powders*

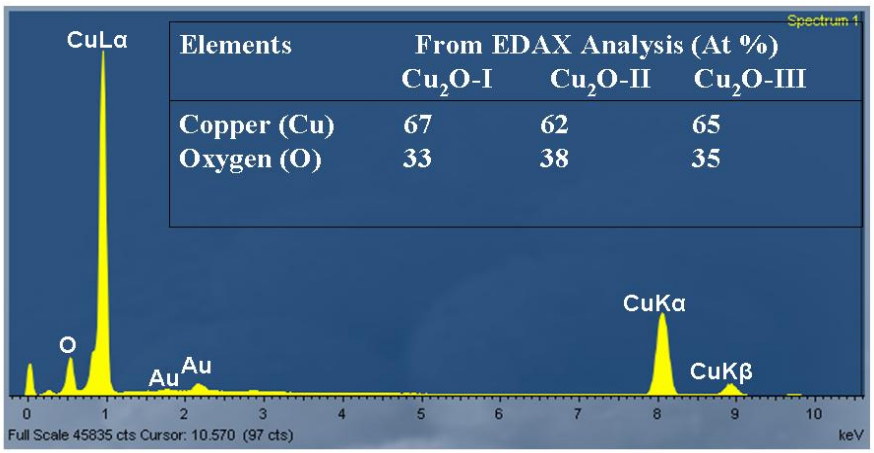

Figure 4.11 *EDAX analysis of Cu_2O-I (peak at 0.93 KeV belongs to Lα, peak at 8.048 and 8.906 KeV belongs to K_α and K_β lines of Copper (Cu) element) powders.*

4.3.7 Nonlinear optical properties

Furthermore, the linear absorption coefficient of the samples was measured by the conventional method on the basis of $\alpha_0 = -(1/L)\ln(T_0)$ is the low intensity (linear regime) absorption coefficient. The optical response of the pure solvent (iso-propanol) was first recorded and we observed no nonlinear response in the range of intensities used with the 532 nm excitation wavelength. Figures 4.12 and 4.13 shows open aperture Z-scan traces of Cu_2O powder in iso-propanol at 6ns and 30ps excitation. All samples show SA to RSA behavior at 6ns excitation. Since 532nm excitation falls in the absorption region, all samples show SA behavior first (when the sample is far from the focal point or at lower intensities) and then due to strong excited state absorption (ESA), the RSA behavior dominates at higher intensities or nearer to the focal point. During ESA, the nonlinear process dominates taking the first excited electron in the lower conduction band region to the higher excited conduction band states

through a second photon. Such a process is referred to as free-carrier or excited-state absorption.

Open aperture Z-scan traces (figure. 4.12) strongly depend on the peak intensity (I_{00}), as the saturation of absorption and ESA effects compete with each other. With increasing input intensity the valley in the Z-scan trace is monotonically enhanced due to strong ESA. These intensity-dependent transmittance curves can be used to calculate contribution from SA and ESA. As along with the predominant ESA, TPA can also simultaneously contribute to the reverse saturable absorption, we use here β_{eff} as the effective excited state absorption coefficient to include both the ESA and the TPA for the theoretical modeling.

Switchover from SA to RSA on increase of the input intensity has been observed in various materials under nanosecond, and femtosecond pulse excitation [33-35]. In order to model this type of behavior of RSA within SA, the observed experimental data is fitted with the following equation that combines the saturation behavior with saturation intensity of I_s and the effective excited state absorption (β_{eff}) coefficients that included both the excited state absorption and two photon absorption (TPA)

$$\alpha(\mathrm{I}) = \frac{\alpha_0}{1+\frac{I}{I_s}} + \beta_{eff} I \qquad (1)$$

Here, the first term describes the saturable absorption and the second term describes reverse saturable absorption including possible direct two photon absorption (β). α_0 is the linear absorption coefficient at 532nm and is derived from the absorption spectrum. I and I_S are laser intensity at each position in the Z-scan and saturation intensity, respectively.

In this case, the propagation of the laser beam through the medium can be given by

$$dI/dz = -\alpha(I)I \qquad (2)$$

where α(I) is the total nonlinear absorption coefficient and z is the propagation distance in the medium. In figure. 11&12 solid lines shows theoretical fit to the experimental data using above equations, where β and I_s have been used as fitting parameters to match the dip and peak, respectively, in the experimental data. We can find that the theoretical simulations are in good agreement with the experimental results.

The laser intensity induces competition between first excited state saturation and nonlinear absorption because of the absorption from the first excited state to the higher states. Because of the long lifetime of the S_1 state, nearly 1.3 ns [36], the excitation laser pulse can induce the electrons in the excited state to undergo a transition to still higher excited states. Cu_2O-I and Cu_2O-II samples were found to be stable up to 540MW/cm^2, Cu_2O-III sample stable up to 135MW/cm^2, above which the materials start getting damaged.

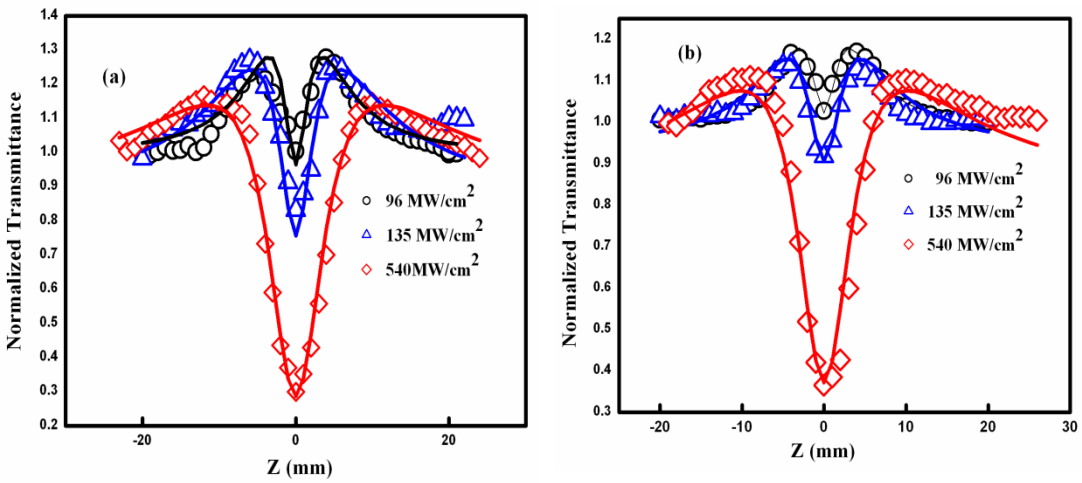

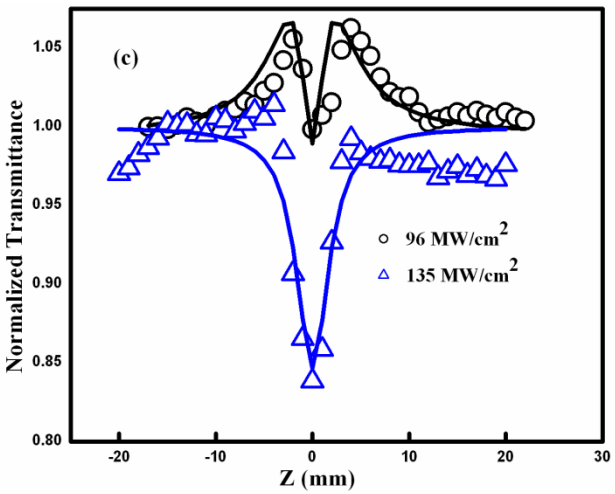

Figure 4.11 *Open aperture Z- scan curves of (a) Cu_2O-I (b) Cu_2O-II (c) Cu_2O-III at 532nm 6ns excitation.(open circles, open triangles and open squares are experimental curves and solid line theoretically generated curves).*

In case 30ps excitation at low intensities (at 3Gw/cm^2) Cu_2O-I shows SA to RSA behavior, Cu_2O-II and Cu_2O-III shows SA to RSA behavior. At higher excitation intensity (9.5 Gw/cm^2) one can clearly observed sample shows only RSA behavior. Theoretically simulated values of β_{eff} and I_s values at 6ns and 30ps are shown in Table. 4.3&4.4. From this table one can observe that β_{eff} values are higher for nano-clusters and micro-cubes compared to their micro-panicles. One can see that as the particle size decreases, we observe an increase in the absorbance in the blue region and also an increase in the linear absorption coefficient at 532 nm. Increase in the linear absorption coefficient increases the excited state absorption and increase in the absorbance in the blue region could lead to larger two photon absorption cross-section. Therefore we see an increase in the β_{eff}. The observed effective nonlinear absorption coefficient at 6ns excitation in the case of Cu_2O-I ($1.9X10^{-8}$ cmW^{-1}) is comparable to some of well known materials like zinc octacarboxy phthalocyanine ($51X10^{-8}$ cmW^{-1}) [37], Pt nanoparticles ($3.22X10^{-8}$ cmW^{-1}) [34] and CdS nanoparticles ($3.15X10^{-}$

^{8} cmW^{-1}) [38]. The observed effective nonlinear absorption coefficient at 30ps excitation is comparable some of the well know Porphyrins [39] and bulk single crystals [40]. nanoparticles ($3.22X10^{-8}$ cmW^{-1}) [34] and CdS nanoparticles ($3.15X10^{-8}$ cmW^{-1}) [38]. The observed effective nonlinear absorption coefficient at 30ps excitation is comparable some of the well know Porphyrins [39] and bulk single crystals [40].

Table 4.3 *The obtained nonlinear optical parameters of Cu_2O powders in iso-propanol at 6ns excitation.*

Sample Name	Linear absorption coefficient (α_0) cm^{-1}	Peak Intensity I_{00} ($MWcm^{-2}$)	I_s ($MWcm^{-2}$)	β (cmW^{-1})	Ref
Cu_20-I	2.143	96	20	$19.0X10^{-9}$	
		135	25	$16.5\ X10^{-9}$	
Cu_20-II	1.703	96	35	$12.2\ X10^{-9}$	
		135	40	$11.5\ X10^{-9}$	
Cu_20-III	0.58	96	45	$4.2\ X10^{-9}$	
		135		$4.2\ X10^{-9}$	
zinc octacarboxy phthalocyanine				$51\ X10^{-8}$	37
DNA (2 wt%) doped Rhodamine 6G PVA solution			140	$540X10^{-12}$	33
Pt–PVP aqueous solution			1.1	$3.22X10^{-8}$	34
CdS nanoparticles				$3.15X10^{-8}$	38

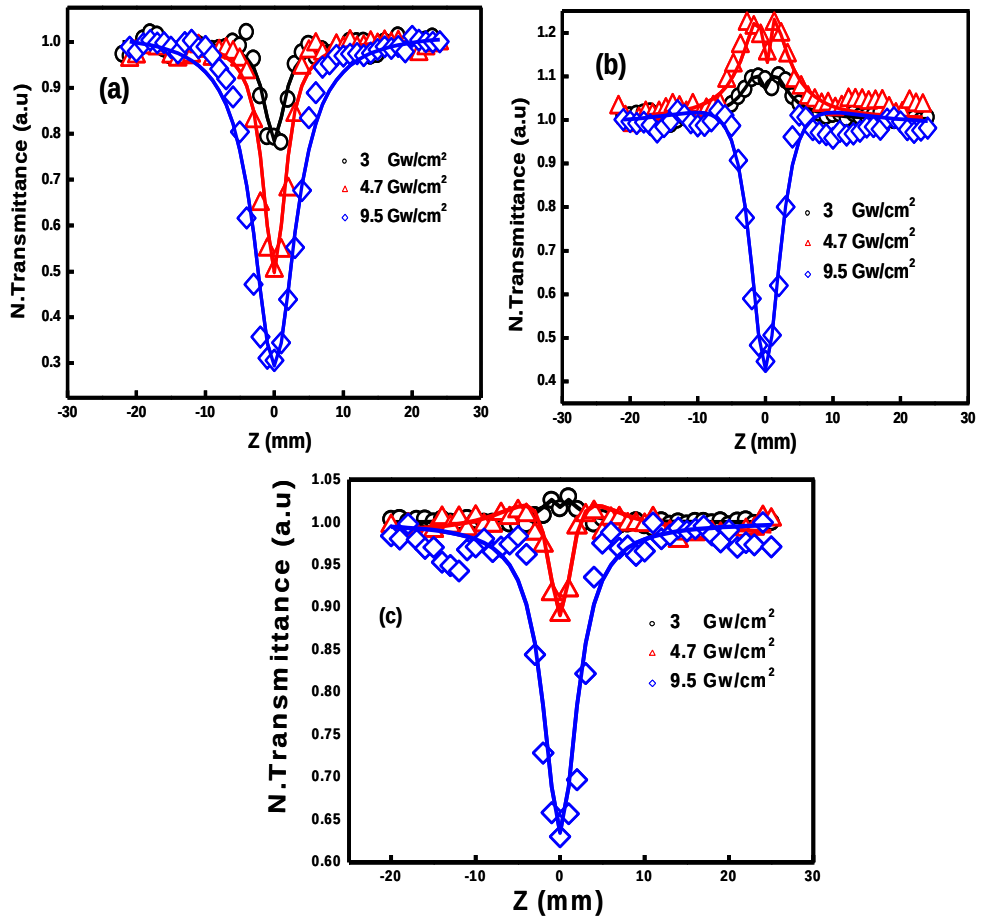

Figure 4.12 *Open aperture Z- scan curves of (a) Cu2O-I (b) Cu2O-II (c) Cu2O-III at 532nm 30ps excitation.(open circles, open triangles and open squares are experimental curves and solid line theoretically generated curves).*

Table 4.4 *The obtained nonlinear optical parameters of Cu_2O powders in iso-propanol at 30 picosecond 532nm excitation*

Sample Name	Linear absorption coefficient (α_0) cm^{-1}	Peak Intensity I_{00} ($MWcm^{-2}$)	I_s ($MWcm^{-2}$)	β_{eff} (cmW^{-1})	Ref
Cu_20-I	2.81	3	--	$6.19X10^{-10}$	
		4.7	--	$6.60\ X10^{-10}$	
		9.5	--	$6.41\ X10^{-10}$	
Cu_20-II	1.91	3	$1X10^{9}$	$3.28X10^{-10}$	
		4.7	$0.1X10^{9}$	$2.95X10^{-10}$	
		9.5	$1.5X10^{9}$	$3.7\ X10^{-10}$	
Cu_20-III	0.69	3	$2.5\ X\ 10^{9}$	$1X10^{-10}$	
		4.7	$1.09X10^{9}$	$2X10^{-10}$	
		9.5	--	$1.5X10^{-10}$	
$Sn–Sn(TTP)_2$ At (25ps ext)				1.5×10^{-9}	39
BSO single crystal At (55ps ext)				2×10^{-9}	40

The major advantage of the Cu_2O nanoparticles is that they are not toxic, easy to synthesize and its source material is cheap. These studies find application in optical limiting devices. The RSA behavior may also find use when Cu_2O is used in solar cells increasing the effective absorption coefficient. SA and RSA behaviors of Cu_2O could also play an important role in photonic devices such as optical pulse compression, optical switching and laser pulse

narrowing. To the best of our knowledge this is the first report on the observation of both SA and RSA behaviors of Cu_2O.

4.4 Conclusion

Different morphologies of Cu_2O nanopowders were prepared by a simple chemical coprecipitation method at room temperature by varying the concentration of NaOH. With increase in the concentration of NaOH, reduction in the XRD peak widths and shift of UV-Vis absorption maximum towards red region demonstrated the increase in the particle size. XRD, FTIR and SAED data confirms the formation of single phase Cu_2O. However, Raman and EPR show spectral lines belonging to both CuO and Cu_2O. From this we conclude that CuO could be in the nanocrystalline form in as synthesized Cu_2O powders. We observed a strong dependence of the band gap with change in the particle size inferred from the UV-Vis, XRD line shapes, FESEM and TEM data. This is the first observation of SA and RSA behavior in case of Cu_2O at 532nm excitation. We also observed a strong dependence of the effective nonlinear absorption coefficient with change in the particle size. Effective nonlinear absorption coeiffient (β_{eff}) values in the case nano-clusters are higher compared to the micro-particles.

4.5 References

1. B.D. Yuhas, P. Yang, *J. Am. Chem. Soc.* 131(10) (2009) 3756.
2. Y.Z. Huang, H. Miao, Q.H Zhang, C. Chen, J. Xu, *Catal Lett.* 122 (2008) 344.
3. W. Liu, G. Chen, G. He, W. Zhang, *J. Nanopart Res.* 13 (2011) 2705.
4. S. Zhuiykov, E. Kats, D. Marney, K. Kalantar-zadeh, *Prog. in Org. Coatings* 70 (2011) 67.

5. S.K. Li, C.H. Li, F.Z. Huang, Y. Wang, Y.H. Shen, A.J. Xie, Q. Wu, *J. Nanopart Res.* 13(2011) 2865.
6. J. Antony, Y. Qiang, M. Faheem, D. Meyer, D.E. McCready, M.H. Engelhard, *Appl. Phys. Lett.* 90 (2007) 013106.
7. C.C Hu, J.N Nian, H. Teng, *Sol. Energy Mater. Sol Cells* 92 (2008) 1071.
8. X. Zhang, J. Song, J. Jiao, X. Mei, *Solid State Sci.* 12 (2010) 1215.
9. L. Zhang, H. Wang, *ACSNano* 5(4) (2011) 3257.
10. H. Sekhar, D. Narayana Rao, *J Mater. Sci.* 47 (2012) 1964.
11. H. Sekhar, D. Narayana Rao, *J Alloys and Compd* 517 (2012) 103.
12. M.J.S. Spencer, I. Yarovsky, W. Wlodarski, K. Kalantar-zadeh, *Nanotechnology* 22 (2011) 135704.
13. S. Nayeb Sadeghi, A. Shafiekhani, M.A. Vesaghi, *J. Nanopart Res.* 13 (2011) 4681.
14. K. Borgohain, N. Murase, S. Mahamuni, *J. Appl. Phys.* 92 (2002) 1292.
15. A. Ye Yermakov, M.A. Uimin, A.A. Mysik, V.B. Vykhodets, T.E. Kurennykh, V.I. Sokolov, V.S. Gaviko, N.N. Schegoleva, N.B. Gruzdev, *J. Magn. Magn. Mater.* 310 (2007) 2102.
16. M.B. Mahajan, M.S. Pavan, P.A. Joy, *Solid State Commun.* 149 (2009) 2199.
17. N. Venkatram, R.S.S. Kumar, D. Narayana Rao, S.K. Medda, S. De, G. De, *J. Nanosci. Nanotechnol.* 6 (2006) 1990.
18. S. Nagarajan, Z. Li, V. Marchi-Artzner, F. Grasset, Y. Zhang, *Med. Biol. Eng. Comput.* 48 (2010) 1033.
19. J. He, G.D. Scholes, Y.L. Qu, W. Ji, *J. Appl. Phys.* 104 (2008) 023110.
20. P. Prem Kiran, S. Venugopal Rao, M. Ferrari, B.M. Krishna, H. Sekhar, S. Alee, D. Narayana Rao, *Nonlinear Opt Quantum Opt.* 40 (2010) 223.

Chapter 4

21. M. Sheik-Bahae, A.A. Said, T.H. Wei, D.J. Hagan, E.W. VanStryland, *IEEE J Quantum Electron.* 26(4) (1990) 760.
22. H. Sekhar, P. Prem kiran, D. Narayana Rao, *Mater. Chem. Phys.* 130 (2011) 113.
23. M. Guedes, J.M.F. Ferreira, A.C. Ferro, *Ceram Int.* 35 (2009) 1939.
24. S. Wang, Q. Huang, X. Wen, X.Y. Li, S. Yang, *Phys. Chem. Chem. Phys.* 4 (2002) 3425.
25. N. Srinivas Rao, S. Bale, M. Purnima, K. Siva Kumar, S. Rahman, *Bull Mater. Sci.* 28(6) (2005) 589.
26. S. Banerjee, D. Chakravorty, *Europhys Lett.* 52(4) (2000) 468.
27. K. Suzuki, N. Tanaka, A. Ando, H. Takagi, *J. Am. Ceram. Soc* 94 (8) (2011) 2379.
28. Z. Wang, H. Wang, L. Wang, L. Pan, *Cryst. Res. Technol.* 44 (6) (2009) 624.
29. M. Chen, G. Diao, X. Zhou, *Nanotechnology* 18 (2007) 275606.
30. C.H. Kuo, C.H. Chen, M.H. Huang, *Adv. Funct.Mater.* 17 (2007) 3773.
31. Z. Huai-Ruo, Y. Hong-Chun, S. Cheng-Min, Y. Huai-Xin, L. Jian-Qi, *Chin Phys.* 15(6) (2006) 1290.
32. M.J. Siegfried, K.S. Choi, *J. Am. Chem. Soc.* 128 (2006) 10356.
33. B. Nithyaja, H. Misha, P. Radhakrishnan, V.P.N. Nampoori, *J. Appl. Phys.* 109 (2011) 023110.
34. Y. Gao, X. Zhang, Y. Li, H. Liu, Y. Wang, Q. Chang, W. Jiao, Y. Song, *Opt. Commun.* 251 (2005) 429.
35. H.I. Elim, J. Yang, J.Y. Lee, J. Mi, Wei Ji, *Appl. Phys. Lett.* 88 (2006) 083107.
36. S. Kundu, S. Jana, P.K. Biswas, *Mater Sci-Poland* 23(1) (2005)

37. M.B.M. Krishna, L. Giribabub, D. Narayana Rao, *J. Porphyrins Phthalocyanines* 16 (2012) 1015.

38. N. Venkatram, D. Narayana Rao, M.A. Akundi, *Opt Express* 13 (2005) 867.

39. P. Prem Kiran, D. Raghunath Reddy, B.G. Maiya, A.K. Dharmadhikari, G. Ravindra Kumar, D. Narayana Rao, Opt. Commun. 252 (2005) 150.

40. R.A. Ganeev, A.I. Ryasnyansky, R.I. Tugushev, M.K. Kodirov, F.R. Akhmedjanov, T. Usmanov, Opt. Quant. Electron. 36 (2004) 807.

Chapter 5

Preparation characterization and its Stokes and anti-Stokes luminescence in heat treated CdS nanopowders

Abstract

In this chapter we discussed about the spectroscopic studies on heat treated CdS nano powders. Structural dependent Stokes and Anti-stokes luminescence were studied by using 6ns Nd: YAG (355nm) and 100 fs Ti: Sapphire (798nm) laser. Heat treatment at 400 and 600 ºC, powders show only a band edge emission with relatively narrow full-width half maximum, which means that powders possess good optical property. Dependence of the anti-Stokes luminescence (upconversion) on heat treatment of the powders was studied through laser excitation.

The results of this chapter are published in Journal of Physical Chemistry C (Accepted) *"Stokes and anti-Stokes luminescence in heat treated CdS nanopowders"* by **H. Sekhar** and D. Narayana Rao

Chapter 5

5.1 Introduction

Recently, there has been a significant increase of interest in small-size semiconductor particles, in which electron and hole wave functions are quantum-confined by a deep potential well. Recent studies have shown that many fundamental physical properties of semiconductor materials strongly depend on the size, shape, and structure of the semiconductor nanocrystals. Chalcogenides consist one or more of the chalcogens or group 16 elements with at least one electropositive element such as cadmium, lead and zinc. Shape controlled synthesis of cadmium chalcogenides with different morphologies such as nanorods, nanowires, nanotrees, and multipods has been reported [1-3]. Due to technical interest cadmium chalcogenides form important class of materials owing to their wide use in a variety of electronic and optoelectronic devices like solar cells, photo detectors, light emitting diodes and optical data storage [4-8]. CdS exhibits the phenomena of cathodoluminescence and phosphorescence. Lasing action has also been reported in single CdS nanowire optical cavities [9]. CdS is an unstable material and can easily change into other materials (like $CdSO_4$, $(CdO)_2$. $CdSO_4$ and CdO) on heating in air [10]. The physical and chemical properties of CdS at nanoscale regime have been exhaustively studied by many researchers over a period of last several years. However, new and sometimes conflicting results have left open the subject on the nature of impurities in CdS and their effects on the physical properties of this and other II-VI compounds. Usually two types of emission bands, band edge and defect luminescence, are observed from CdS nanoparticles. The band edge emission is narrow and located near the absorption edge of the particles, while the defect emission is always broad and Stokes-shifted [3,11,12].

In a majority of cases luminescence processes that typically involve an excited state, the lower level or the ground state. The subject “anti-Stokes

luminescence" also called "infrared to visible conversion", or "co-operative luminescence" or "photon summing" or simply "up-conversion" has received much attention from the scientific community, particularly while increasing the solar cell efficiencies. Femtosecond (near-infrared) pulsed laser is an ideal excitation source to investigate various luminescent mechanisms as it generates intense pulses at high repetition rate and shorter pulse duration. The generation of shorter wavelength or high energy photons is one of the important goals of research in photonics. Harmonic generation, parametric up-conversion, stimulated Raman scattering and anti-Stoke (up-conversion) luminescence are some of the popular methods for converting low energy photons to high energy photon. Up-conversion luminescence (UCL) is a type of luminescence where the excitation wavelength is longer than the emission wavelength.

The up-conversion is a nonlinear process and it has been used to detect the defects and understand their emission in semiconductor quantum dots [13], which is different from that of the band edge emission. The existence of intermediate states with energies resonant with or lower than those of the excitation photons is a prerequisite for this up-converted photoluminescence. Carriers must be excited to these intermediate states by the first excitation photon and further to the higher energy states through various underlying mechanisms such as Auger excitation [14], two-step two-photon absorption [15], or the thermal effect [16]. Nanoparticles play a major role in the up-conversion as their energy level position and the transition probabilities between various levels get modified due to quantum size effects. The up-conversion luminescence of nanoparticles has many potential applications in display technology, memory, lighting, solar cells, optical sensing and bio-imaging applications [17]. In semiconductors, band gap energy is an important parameter that determines electronic and optical properties [18]. For stronger

band edge emission, one has to control the defect states as the defect states compete with the band edge emission. Band-edge luminescence was previously observed in various semiconductors at low temperature [19].

5.2 Experimental

Materials: **C**admium acetate dihydrate, Sodium sulfide, Polyvinyl pyrrolidone (PVP), milli Q water

5.2.1 Preparation

Nanopowders of PVP capped CdS, were prepared by simple co-precipitation method in milli Q water at room temperature [20]. In the preparation process, first 30 ml of 0.1 M Na_2S aqueous solution and 30 ml aqueous solutions of cadmium acetate were prepared. At room temperature about 15ml of PVP (MW-55,000) solution in methanol was added to 30 ml of Cd aqueous solution by vigorous stirring. 0.1 M Na_2S solution was added slowly drop-wise to the Cd-PVP mixed solution under vigorous stirring. After 90 minutes of stirring, the precipitate particles were isolated from the solution by centrifuging at 6000 rpm for 15 min. The precipitate was washed with milli-Q water and methanol through multiple cycles of centrifuging. The synthesized powders were heat treated at 80 ºC in silicon oil bath for 6 hours. This dried CdS powders were again heat treated for 2 hours at different temperatures of 200, 300, 350, 400, 600 and 725 ºC in air environment and then characterized by different spectroscopic techniques.

5.3 Results and Discussion

5.3.1 TG-DTA

Thermal analysis of the as-synthesized CdS powders (at 80 ºC) was carried out to know the possible changes occurring when the samples were subjected to heat treatment. Figure 5.1(a) shows a plot of the TGA data (left curve) and figure 5.1(b) shows the plot of the DTA data (right curve) as a function of sample temperature. From TGA curve, one can observe two prominent major weight reductions; first weight reduction of 8 % between 265 to 391 ºC. The corresponding DTA curve shows exothermic peak at 350 ºC is related to decomposition of water and organics in CdS. Second weight reduction of 10 % loss in TGA between 687 to 746 ºC has been reported as due to change from cubic to hexagonal phase in inert gas atmosphere while it forms a mixture of CdO and $CdSO_4$. 2CdO in air environment [21]. There is an overall weight loss of 27% till 800 ºC for CdS when heated in inert gas atmosphere.

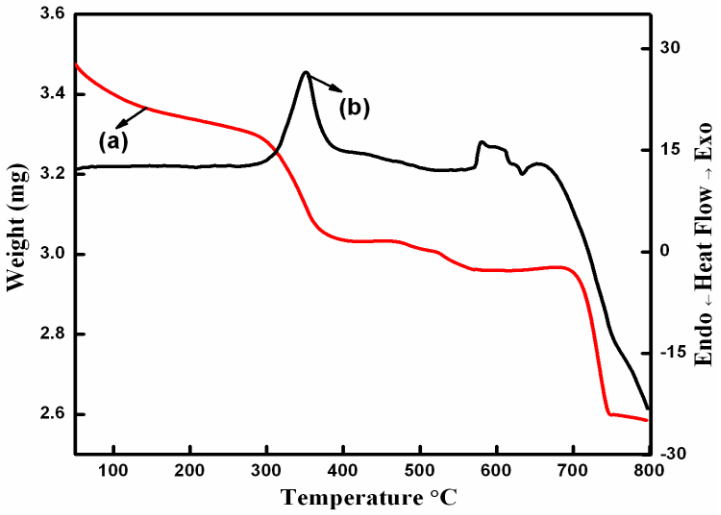

Figure 5.1 *(a) TGA (b) DTA curves of CdS powders*

5.3.2 XRD

CdS can crystallize in four different crystalline structures: the hexagonal structure (wurtzite), cubic structure (zinc blende), the cubic rock salt structure and the distorted rock salt structure. It is well known that bulk CdS has stable wurtzite (hexagonal) structure from room temperature to melting point. However, metastable cubic phase has been found in thin films and nanocrystalline powders [3,4]. Although the coexistence of cubic and hexagonal phases has been reported for CdS. Thermal behavior of CdS in air environment is complicated. Therefore X-ray diffraction studies were carried out to determine the phase change when the samples were heat treated from 80 to 725 ºC leaving the sample at each temperature for two hours. Figure 5.2 shows the X-ray diffraction spectra. X-ray diffraction reflection peaks of heat treated sample at 80 and 200 ºC sample are broad in nature as shown in figure 5.2(a). This can be attributed to a very small grain size of the particles [20]. X-ray diffraction peaks are assigned to (1 1 1), (2 2 0), (3 1 1) and (3 3 1) planes of cubic phase [20] and well matches with its JCPDS data card no. 80-0019. If we heat the powders to 300 ºC one can observe from the figure 5.2(a) small peaks of (100) and (101) hexagonal phase riding over the (111) peak of cubic phase suggesting the presence of small amount of hexagonal phase. If we increase the heating temperature above 300 ºC, one can clearly see that the intensities of these two hexagonal phase peaks at $2\theta=36.6^0$ and 47.8º increase. From this result we conclude that the relative content of hexagonal phase increases with the increase in temperature, while the heat treated sample at 600 ºC the structure becomes completely hexagonal. The fraction of hexagonal phase was estimated from the total integrated intensities of (1 0 0), (1 0 3) and (0 0 2), (1 1 0) lines. The relative content of hexagonal phase (X_h) [22] was calculated from the ratio $(I_{100} + I_{103})/(I_{002}+ I_{110})$. The content of hexagonal phase with respected to the

sample's temperature was calculated and is shown as inset of figure 5. 2(b). If we increase the temperature one can clearly observe that the X-ray diffraction peaks become sharp and FWHM decreases, i.e. crystallite size increases. Because of heat treatment in air environment oxygen diffuses into the crystal lattice and surface atoms of sulfur in CdS get oxidized forming $CdSO_4$. Earlier studies show that CdS gets partially oxidized to the extent of 44.3% as $CdSO_4$ [10]. The XRD pattern of heat treated at 600 ºC powders confirms that their structure corresponds to that of mixture of CdS and $CdSO_4$ (with JCPDF data card no. 77-2306 and 85-0673). When powders are heat treated at 725 ºC, it forms like sulfur dioxide (SO_2) and $CdSO_4.(CdO)_2$ (with JCPDF No 32-0140). These differences are due to the complicated nature of the heterogeneous processes affected by the chemical adsorption or heat exchange processes, etc.

Possible reactions are as follows

$$CdS + 2O_2 \longrightarrow CdSO_4 \text{ (At 400 and 600 ºC 2hours)}$$

$$3CdS+5O_2 \longrightarrow (CdO)_2.\ CdSO_4 + 2SO_2 \text{ (At 725 ºC 2hours)}$$

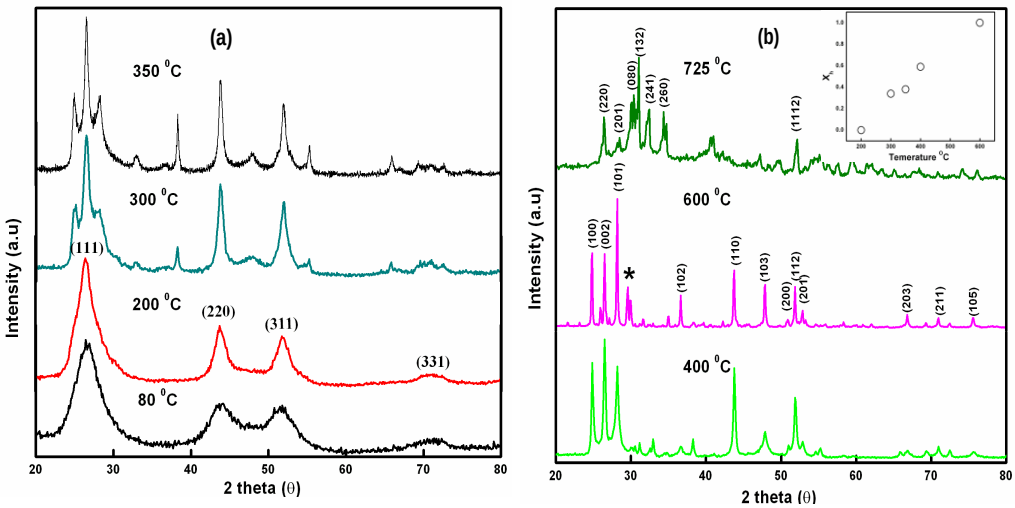

Figure 5.2 *XRD pattern of CdS powders heat treated at (a) 80 200, 300 and 350 ºC (b) 400, 600 and 725 ºC.*

5.3.3 FTIR studies

FT-IR studies were carried out to understand the bond formation in heat treated CdS powder samples and their spectra are shown in figure 5.3. The band at 632 cm^{-1} belongs to Cd-S stretching [20]. If we increase the temperature from 200 to 400 ºC or above one can see that absorption band at 1095 cm^{-1} increasing. Absorption band at 1095 cm^{-1} is assigned to SO_4^{-2} [23], which means that the powders get oxidized at higher temperatures. From this result we conclude that oxygen diffuses into the crystal lattice and surface atoms of sulfur in CdS will get oxidized to $CdSO_4$. In the higher energy region the peak at 3420 cm^{-1} is assigned to O-H stretching, peak at 1632 cm^{-1} is assigned to bending (H-O-H) vibration of the water absorbed on the surface of CdS [24].

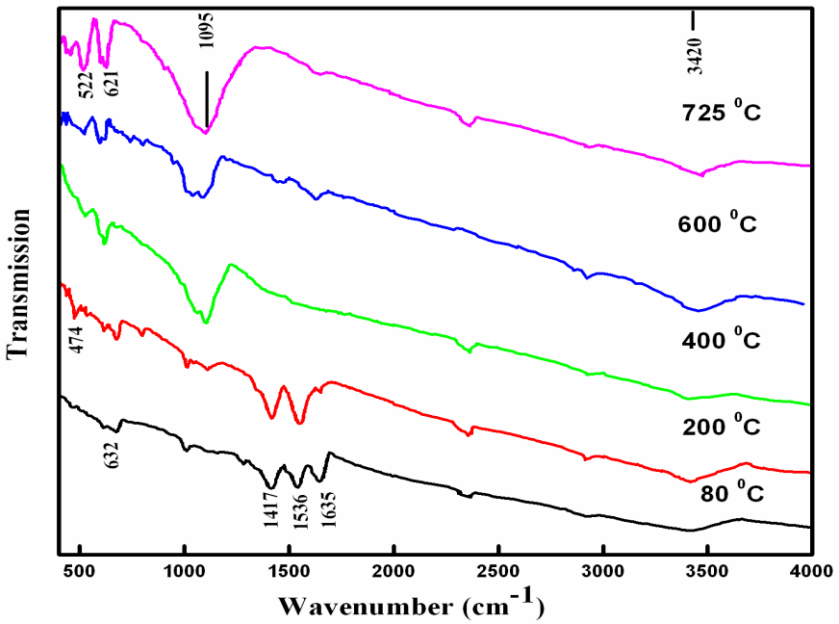

Figure 5.3 *FT-IR spectrum of CdS powders heat treated at different temperatures.*

5.3.4 Raman Studies

Raman spectrum of as synthesized CdS powders is shown in figure 5.4. The peaks at 300 and 600 cm^{-1} are attributed to the first-order and second-order longitudinal-optical phonons (1-LO and 2-LO) of A_1 mode, respectively [24]. Raman spectra of CdS nanopowders prepared at 80 and 200 ºC, a decrease (red-shift (293 and 593 cm^{-1})) of the phonon frequency with respect to CdS bulk frequency is expected. In particular, red shift is expected to be more pronounced for the smallest particles, while at the size increase of nanocrystals, the phonon frequency will approach progressively to the bulk value. Raman peaks of cubic and hexagonal phases do not shift significantly upon the transformation from cubic to hexagonal phase. We observed two differences in Raman signals of hexagonal phase when compared to the Raman signals of cubic phase. The intensity of 2-LO mode is more in hexagonal phase compared to the cubic phase. One finds that the ratio I_{2LO}/I_{1LO} decreases as the particle size reduces as seen from figure 5.4 confirming that the smaller particle forming at lower temperatures are rich in cubic phase. Further the ratio of 2-LO to 1-LO mode intensities (I_{2LO}/I_{1LO}) is a parameter used to specify exciton–phonon interaction strength (S) in the semiconductors. The present results suggest that electron-phonon interaction in hexagonal phase is more compared to their cubic phase because of increasing of the particle size [22]. In Raman signal, the broad background in heat treated (400 ºC) powder samples is due to the photoluminescence. We can also observe that the FWHM of 1-LO and 2-LO modes reduces in case of the hexagonal phase, which is attributed to the increase of particle size. In case of cubic CdS (heat treated at 80 ºC) FWHM of 1-LO peak is 37 cm^{-1}. In hexagonal CdS phase (heat treated at 400 and 600 ºC) FWHM of 1-LO peak is 12 cm^{-1}. A weak band appearing at 235 cm^{-1} corresponds to the E_1 (TO) vibrational modes of CdS [25]. Peaks appearing at

92 and 130 cm^{-1} in heat treated samples are not assigned to any vibrations. Sample shows some distinctive features when heat treated at 725 ºC as compared to the spectra of the samples heat treated at other temperatures. Peaks at 300 and 600 cm^{-1} belong to LO phonons of CdS. Peaks at 426, 627, 997 and 1093 cm^{-1} belong to Raman bands of SO_4^{-2} ion [26].

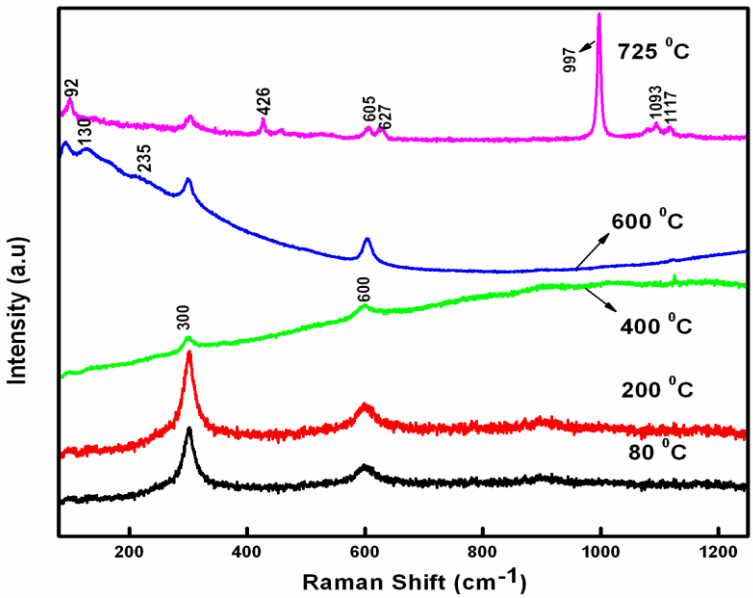

Figure 5.4 *Raman spectrum of CdS powders heat treated at different temperatures.*

5.3.5 FE-SEM-EDAX and TEM analysis

Figure 5.5 shows FE-SEM (lower magnification) and TEM (higher magnification) images of CdS powders. TEM bright-field images are shown as inset of FE-SEM images. From this data we conclude that the particle sizes of as synthesized powder at 80 ºC are smaller in size (3-4nm) compared to the particles heat treated at 400 ºC and above. Smaller size particles experience an enhanced residual strain in addition to a large interfacial energy and large surface to volume ratio. With increasing temperature, the strain relief, the

thermal expansion and the surface melting [27-29] may cause recombination of nanocrystallites. Therefore, an increase in the temperature results in increase in the size of crystallite. Figure 5.6 shows High resolution-TEM images of the synthesized powders heat treated at different temperatures. Lattice fringes observed with 80 ºC heat treated powder give a lattice spacing of about 0.3595 nm and it matches well with the (111) planes of CdS with cubic structure. At 400 and 600 ^{0}C heat treated sample lattice fringes with a lattice spacing of about 0.3197 nm agree well with the (101) planes of CdS having a hexagonal structure. Figure 5.7 shows selected-area electron diffraction (SAED) pattern of CdS powders heat treated at different temperatures. SAED pattern of 80 ºC heat treated CdS powder samples shows that particles are polycrystalline and have cubic structure. The 400 ºC heat treated powders show dot pattern which tells that the particles are crystalline exhibiting wurtzite (hexagonal) structure. For elemental quantification, the heat treated CdS powders were mounted on double-sided carbon tape for carrying out the EDAX analysis. From the EDAX data shown in figure 5.8 and condensed in table 5.1, one can observe that the content of oxygen increases with increasing temperature. This increase in oxygen content proves that oxygen diffuses into the crystal lattice and surface atoms of sulfur interact with oxygen getting oxidized as $CdSO_4$. We have already shown that in FTIR studies the SO_4^{-2} ion band at 1095 cm^{-1} becomes stronger with increasing temperature. Therefore from the EDAX and FTIR studies we conclude that with increasing temperature oxygen will diffuse into the crystal lattice and also leads to the formation of $CdSO_4$.

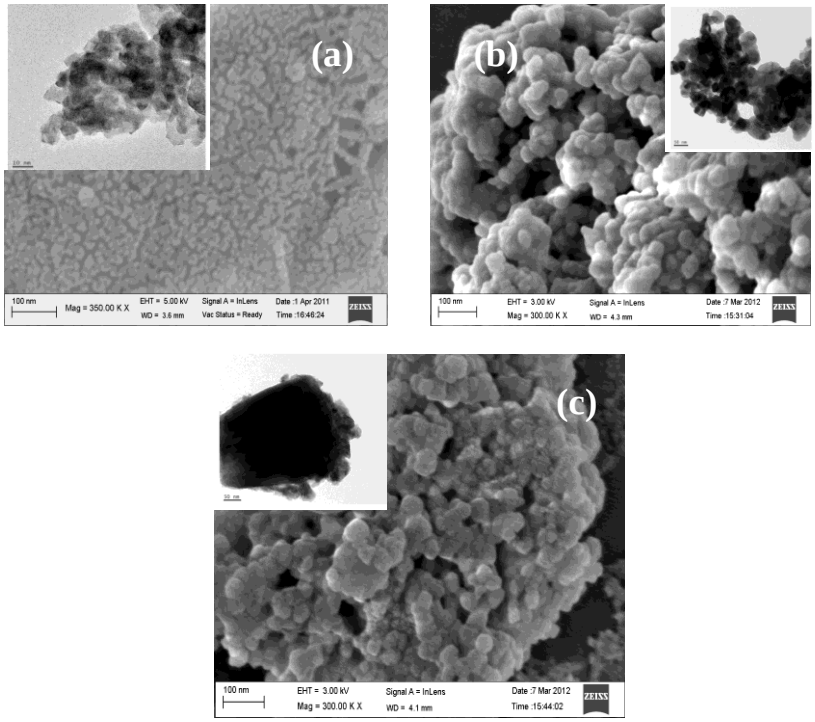

Figure 5.5 *FE-SEM and TEM images of as synthesized CdS powders at (a) 80 ºC (b) 400 ºC (c) 600 ºC.*

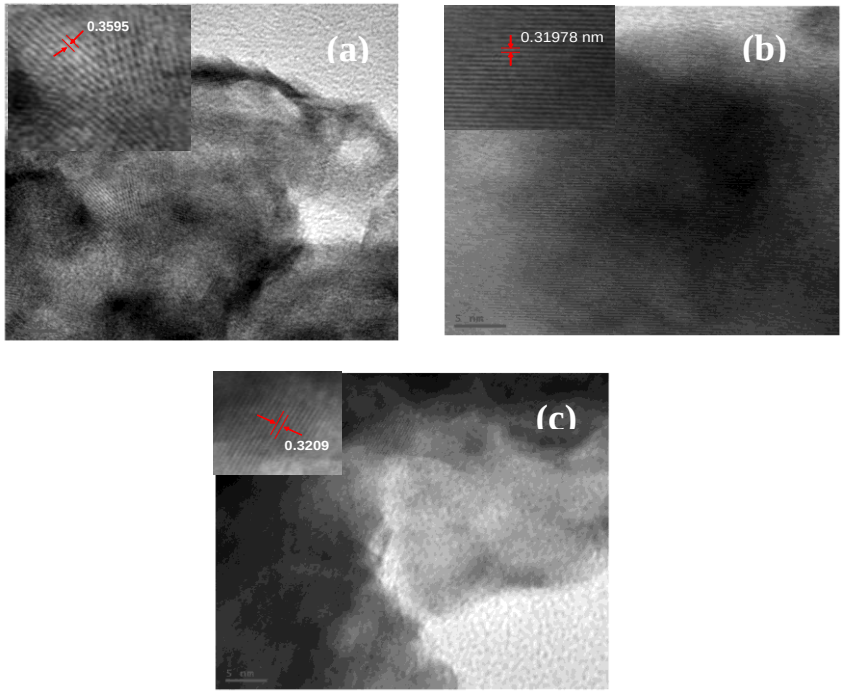

Figure 5.6 *HR-TEM and SAED pattern of as synthesized CdS powders at (a) 80 ºC (b) 400 ºC (c) 600 ºC.*

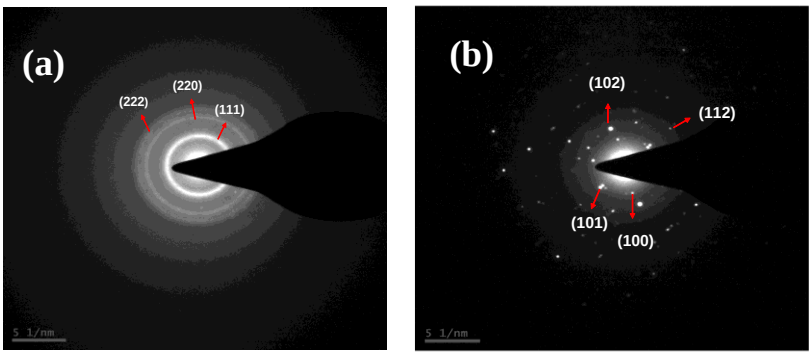

Figure 5.7 *SAED pattern of CdS powders heat treated at (a) 80 ºC (b) 400 ºC*

Table 5.1 *Calculated compositional ratio (from EDAX analysis) of CdS powders heat treated at different temperatures.*

Sample	Elements (At %) From EDAX analysis		
	Cd	S	O
CdS (at 80 ºC)	50.09	49.01	0
CdS (at 200 ºC)	50.64	44.23	5.13
CdS (at 400 ºC)	44.41	42.21	13.38
CdS (at 600 ºC)	33.77	29.77	36.46
CdS (at 725 ºC)	26.26	8.33	65.41

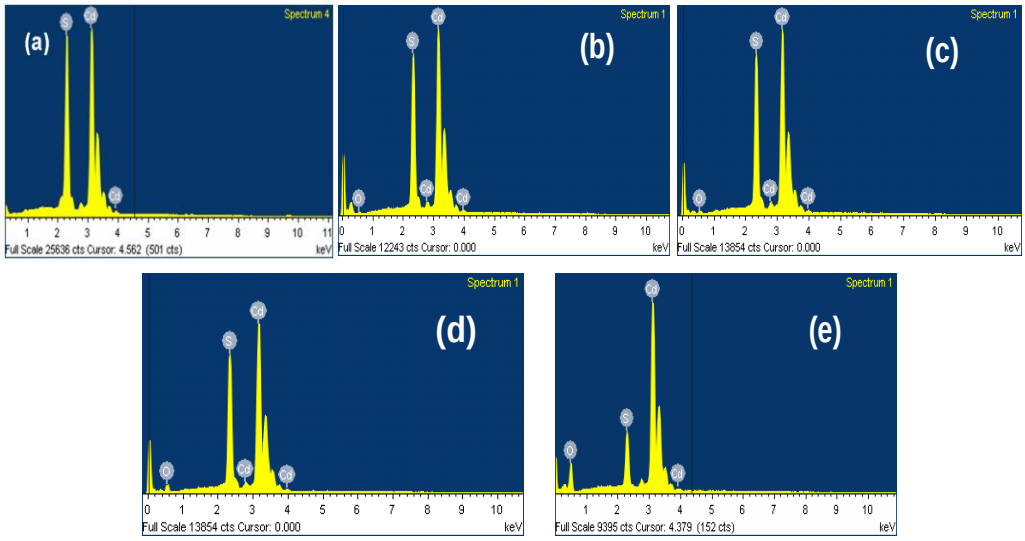

Figure 5.8 *EDAX analysis of as heat treated powders at (a) 80 ºC (b) 200 ºC (c) 400 ºC (d) 600 ºC (e) 725 ºC*

5.3.6 Diffuse Reflectance Spectral studies

Electronic spectra were recorded on a Varian Cary 100 UV–Vis spectrometer in diffuse reflectance geometry, using the DRA-CA-30I sphere accessory. The optical properties of the heat treated CdS powders were studied by using UV–Vis diffuse reflectance spectroscopy (DRS). The diffuse reflectance spectrum converted into absorption spectrum using Kubelka–Munk function for powder samples and as shown in figure 5.9a. From this figure it can be seen that the absorption edge of heat treated CdS powders at 400 and 600 ºC are close to each other. The CdS is a direct semiconductor [30,31]. Direct band gap values of the CdS powder samples were estimated from the $(\alpha h\gamma)^2$ versus photon energy ($h\gamma$) plot which are shown in figure 5.9b. By extrapolating the absorption edge, by linear fit method, the band gap values of the samples are estimated and listed in table 5.2. The optical bandgap (E_g) is found to be temperature dependent and there is a decrease in the bandgap of the semiconductor with increase in the temperature up to 600 ºC. From this table one can observe that the 80 ºC heat treated powders show larger band gap (3.1 eV) compared to the 400 and 600 ºC heat treated samples (2.2eV) which is due to the quantum confinement effect. The optical bandgap (3.11 eV) of 725 ºC heat treated powder sample is different from that of 400 and 600 ºC heat treated powder samples, as the phase changes to $CdSO_4$ $(CdO)_2$. When CdS powder samples are heat treated at 725 ºC, CdS disintegrates in air environment as $CdSO_4$. $(CdO)_2$ and SO_2. From XRD results we can see that the peak at 47.8º has totally disappeared thereby indicating that the powder gets completely converted to $CdSO_4$ $(CdO)_2$ phase. There could be a small quantity of CdS, but it cannot be confirmed from our studies. The band gap strongly depends on size and composition and the observed shift in the band gap to higher energy is attributed to the formation of $CdSO_4$. $(CdO)_2$, which has a different band gap

compared to the CdS. Unfortunately no literature is available on the band gap of this composition. In case of 725 ºC heat treated samples one can observe that the absorption spectrum extends up to 700 nm with large number of defect states.

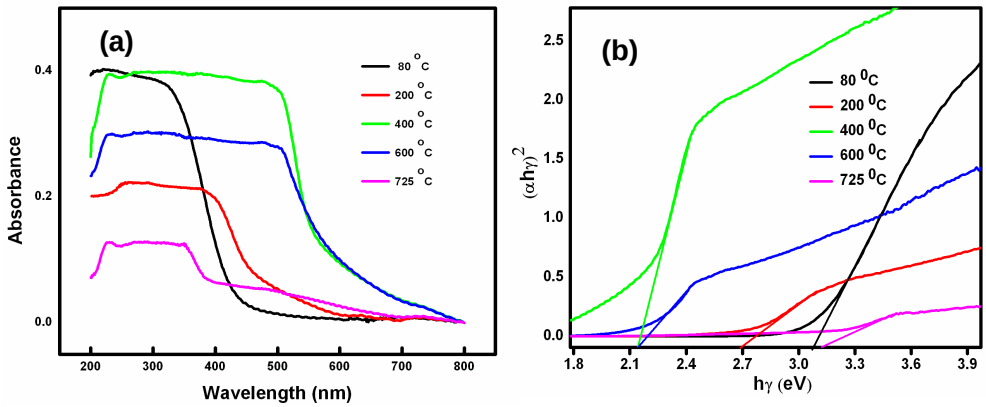

Figure 5.9 *(a) DRS spectra of heat treated CdS powders. (b) hγ versus* $(\alpha h\gamma)^2$

Table 5.2 *Optical bandgap of heat treated CdS powders.*

Sample Code	Band gap (eV)
80 ºC	3.08
200 ºC	2.70
400 ºC	2.14
600 ºC	2.14
725 ºC	3.11

5.3.7 Stokes and anti-Stokes luminescence

For Stokes luminescence (down conversion) samples were excited with 6 ns pulse duration third harmonic at 355 nm of the Nd: YAG laser with a repetition rate of 10Hz. For recording the anti-Stokes (Up-conversion) luminescence of as

heat treated solid samples, 100-fs pulses delivered by a Ti: sapphire laser at 798 nm with a repetition rate of 80 kHz was employed for excitation. Excitation power was varied by using a continuously adjustable neutral density filter and keeping a fixed distance between the sample and the focusing lens. Stokes and anti-Stokes luminescence spectra were collected by Ocean Optics fiber spectrometer. Stokes and anti-Stokes luminescence spectra of heat treated powder samples are shown in figure 5.10 and figure 5.11. Stokes and anti-Stokes luminescence of these heat treated CdS powders under laser excitation was so strong that it was visible to the naked eye and the same was imaged with a Digital (Canon) camera. Stokes luminescence of CdS (heat treated at 80 ºC) powders dispersed in chloroform was shown in our earlier publication [20]. At lower wavelength (290 nm) excitation, CdS shows broad emission centered at 404 nm. To record the Stokes luminescence (down conversion), samples were excited with the third harmonic of Nd; YAG laser at 355 nm. The observed spectrum is shown in figure 5.10. With increasing temperature from 200 to 600 ºC, the Stokes luminescence at 521 nm increases. In 725 ºC heat treated samples, the luminescence decreases while the FWHM increases compare to the 400 and 600 ºC samples. This could be due to the compositional change and also increase of trap or defect states in 725 ºC heat treated samples. The Stokes spectrum of CdS powders heat treated at 400 and 600 ºC shows only a single narrow sharp peak centered at 521 nm with smaller full-width half maximum (fwhm) of 32 nm attributed to band edge emission of CdS [32]. Heat treatment at 725 ºC powder shows the FWHM of as 73nm and the peak splits into two peaks at 521 and 531nm.

For anti-Stokes luminescence (upconversion), samples were excited with 790nm Ti: sapphire laser which delivers 100 fs pulses at 1 KHz. Anti-Stokes luminescence shows a strong dependence on the structure of CdS. At 80

and 200 ºC heat treated powder samples, the CdS is cubic phase and the 725 ºC heat treated powders change its phase from CdS to $CdSO_4$. $(CdO)_2$. This phase does not show any anti-Stoke luminescence. When powders are heat treated at 400 and 600 ºC, the phase changes from cubic to hexagonal. Anti-Stokes luminescence is much stronger in the 600 ºC heat treated samples when compared to the 400 ºC heat treated samples. At 600 ºC heating allows a complete change into hexagonal phase from the cubic phase. Once increases the heating temperature to 400 ºC might cause to increase size of the particle approximately 30-40nm (figure 5.5(b)) and absorption spectrum shifts towards red region (approximately bulk CdS bandgap) due to increasing particle size. Observed Stokes and anti-Stoke green luminescence belongs to band to band transition in CdS [32]. If we increase the temperature upto 600 ºC Stokes and anti-Stoke green luminescence increases compare to their 400 ºC samples. One can clearly observe from the inset of the figure 5.5(c) that smaller grains will aggregate and it forms like bigger particles. Due to increasing particle size the observed anti-Stoke luminescence increases compare to their 400 ºC samples. Earlier studies on rare earth doped phosphorus materials shown that upconversion luminescence is stronger in bigger particles compare to their smaller particles [33,34]. At 725 ºC, the phase changes to $CdSO_4.(CdO)_2$, which may not have strong two photon absorption cross-section. The relationship between anti-Stokes luminescence intensity (I) induced by multiphoton absorption and incident input light intensity ($I_{in)}$ usually shows exponential relation

$$I \alpha I_{in}^{n}$$

Where n is, the number of pump photons required to populate the emitting state. In order to show that two photon absorption (TPA) is the mechanism for the occurrence of the anti-Stokes emission, we carried out

intensity dependent luminescence studies. The inset in figure 5.11 show the log-log plots of the detected anti-Stokes luminescence signal intensity versus the excitation intensity. Its slope is approximately equal to 2, which means that the dominant mechanism for the upconversion is the TPA. The anti-Stokes spectrum shows more than one peak as the states leading to emission which may depend on the selection rules for two photon absorption, while for the Stokes emission the selection rules and the transition probabilities are different and the emission is mostly from the band edge.

With increasing excitation intensity one can observe from figure 5.11 (b) that the TPA induced band edge emission peak shifts towards red region. This is explained as at higher intensities, the two photon absorption takes the electrons to higher energy states, which are more energetic than the band edge. The difference between this state and the band edge is lost into the lattice as thermal energy through nonradiative transitions leading to an increase in the local temperature. At 400 ^{0}C heat treated samples, one can see that the band edge is much steeper than at 600 ^{0}C. The peak of the TPA induced band edge emission is therefore at the same wavelength at different intensities. While at 600 ^{0}C the band edge has longer tail and with increased intensity, the local temperatures would be higher and this leads to an increase in the absorption cross-section for shorter wavelengths leading to a red shift in the peak position of the luminescence [15,35]. At 725 ºC, the phase changes to $CdSO_4.(CdO)_2$, which may not have strong two photon absorption cross-section.

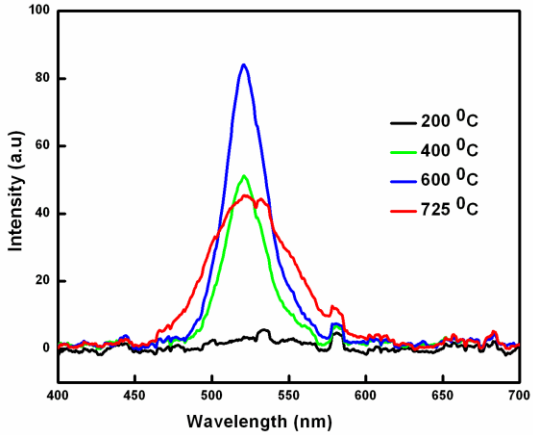

***Figure** 5.**10** Stokes luminescence of CdS powders at different heat treatment.*

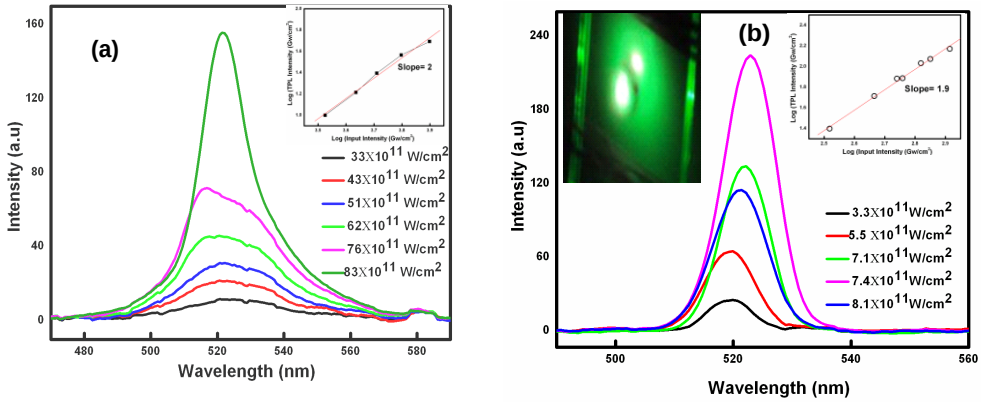

***Figure** 5.**11** Anti-stoke luminescence of CdS powders heat treated at (a) 400 ºC and (b) 600 ºC*

5.4 Conclusions

From XRD results, we conclude that increasing temperature from 200 to 400 ºC or above allows changing phase from cubic to hexagonal. At 725 ºC heat treated powders shows $(CdO)_2$. $CdSO_4$ phase. From FTIR, the absorption band at 1095 cm^{-1} increase with increasing temperature is assigned to SO_4^{-2} vibrations. FWHM of Raman peak decreases with increasing temperature. We

observed structural dependent one and two-photon induced PL emissions in the CdS. Room-temperature Stokes and anti-Stokes band edge luminescence increases with increasing temperature from 400 to 600 ºC. FWHM of Stokes luminescence broadens in case of CdS powders heat treated at 725 ºC. Anti-Stokes luminescence observed with 790 nm excitation is due to two photon absorption induced process.

5.5 References

1. M. Chen, Y. Nam Kim, C. Li, S. Oh Cho, *Cryst. Growth Des.* 8 (2008) 629.
2. W.T. Yao, S.H. Yu, S.J. Liu, J.P. Chen, X.M. Liu, F.Q. Li, *J. Phys. Chem. B* 110 (2006) 11704.
3. A. Datta, S.K. Panda, S. Chaudhur, *J. Phys. Chem. C* 111 (2007) 17260.
4. L. Wang, Y. Liu, X. Jiang, D. Huan Qin, Y. Cao, *J. Phys. Chem. C* 111 (2007) 9538.
5. Y. Jin-nouchi, S. Naya, H. Tada, *J. Phys. Chem. C* 114 (2010) 16837.
6. S. Manna, S. Das, S.P. Mondal, R. Singha, S.K. Ray, *J. Phys. Chem. C* 116 (2012) 7126.
7. C.F. Lin, E.Z. Liang, S.M. Shjh, W.F. Su, *Proc. SPIE* 4641 (2002) 102.
8. X. Li, C. Bullen, J.W.M. Chon, R.A. Evans, M. Gu, *App. Phys. Lett.* 90 (2007) 161116-3.
9. R. Agarwal, C.J. Barrelet, C.M. Lieber, *Nano Lett.* 5 (2005) 917.
10. A. Sabah, S.A.Siddiqi, S. Ali *World Academy of Science, Engineering and Technology* 69 (2010) 82.
11. F. Chen, R. Zhou, L. Yang, N. Liu, M. Wang, H. Chen, *J. Phys. Chem. C* 112 (2008) 1001.

Chapter 5

12. H. Pan, C. Kok Poh, Y. Zhu, G. Xing, K. Chung Chin, Y. Ping Feng, J. Lin, C. Haur Sow, J. Wei, A.T.S. Wee, *J. Phys. Chem. C* 112 (2008) 11227.
13. N. Venkatram, R.S.S. Kumar, D. Narayana Rao, *J. App. Phys.* 100 (2006) 074309-8.
14. Y. Yang, Y.H. Zhang, W.Z. Shen, H.C. Liu, *Prog. Quantum Electron.* 35 (2011) 77.
15. J. He, G.D. Scholes, Y.L. Qu, Wei Ji, *J. Appl. Phys.* 104 (2008) 023110.
16. C.J. da Silva, M.T. de Araujo, *Opt. Mater.* 22 (2003) 275.
17. D. Vennerberg, Z. Lin, *Sci. Adv. Mater.* 3 (2011) 26-40.
18. H. Sekhar, D. Narayana Rao, *J. Nanopart Res.* 14 (2012) 976.
19. A.L. Pan, R.B. Liu, Q. Yang, Y.C. Zhu, J. Zuo, B.S.Zou, *J. Physics: Conference Series* 28 (2006) 12.
20. H. Sekhar, D. Narayana Rao, *J. Mater. Sci.* 47 (2012) 1964.
21. M. Kristl, I. Ban, A. Danc, V. Danc, M. Drofenik, *Ultrasonics Sonochem.* 17 (2010) 916.
22. V. Sivasubramanian, A.K. Arora, M. Premila, C.S. Sundar, V.S. Sastry, *Physica E* 31 (2006**)** 93.
23. 21. M.M. Shokarev, F.I. Vershinina, E.V. Margulis, *J. Struct. Chem.* 11 (1970) 141.
24. H. Sekhar, D. Narayana Rao, *J. Alloys and Compd.* 517 (2012) 103.
25. O. Zelaya-Angel, F. de L. Castillo-Alvarado, J. Avendailo-Lopez, A. Escamilla-Esquivel, G. Contreras-Puente, R. Lozada-Morales, G. Torres-Delgado, *Solid State Commun.* 104 (1997)161-166.
26. W. Rudolph, G. Irmer, *J. Solution Chem.* 23 (1994) 663-684.
27. S.B. Qadri, M. Kuno, C.R. Feng, B.B. Rath, M. Yousuf, *App. Phys. Lett.* 83 (2003) 4011.

28. A.N. Goldstein, C.M. Echer, A.P. Alivisatos, *Science* 256 (1992) 1425.
29. S.B. Qadri, E.F. Skelton, D. Hsu, A.D. Dinsmore, J. Yang, H.F. Gray, B.R. Ratna, *Phys. Rev. B* 60 (1999) 9191.
30. H. Jia, Y. Hu, Y. Tang, L. Zhang, *Electrochem. Commun.* 8 (2006) 1381.
31. Y.C. Zhang, W.W. Chen, X .Y. Hu, *Cryst. Growth Des*. 7 (2007) 580-586.
32. T. Gao, T. Wang *J. Phys. Chem B.* 108 (2004) 20045.
33. G. Yi, H. Lu, S. Zhao, Y. Ge, W. Yang, D. Chen, L.H. Guo, *Nano Lett.* 4 (2004), 2191.
34. G.S. Yi, G.M. Chow, *Adv. Funct. Mater.* 16 (2006) 2324.
35. H. Kalt, M. Rinker, *Phys. Rev. B* 45 (1992) 1139.

6.1 Summary of Results

Intense research is currently being pursued in the field of material preparation, characterization and its linear, nonlinear optical properties of nanoparticles by various laboratories, motivated by the fundamental question of how the material properties evolve with size. My doctoral dissertation is an attempt to prepare few new nano materials with cost effective techniques and study its confinement effect through linear and nonlinear optical absorption spectral studies and our goal is to achieve better optical limiters (materials that would act as linear absorption media at low intensities/fluences and limit to a threshold at higher intensities/fluences).

To summarize, we have studied three different classes of nano materials. My doctoral dissertation is focused on the investigation of nonlinear optical materials like oxides ($Bi_{12}SiO_{20}$ and Cu_2O) and CdS nanomorphologies.

In Chapter 3, we explored the preparation of $Bi_{12}SiO_{20}$ nanoparticles in gram scale quantities by using simple chemical solution decomposition (CSD) method. The value of β for BSO nanocrystals was found to be four orders of magnitude higher for 6 ns excitation and two orders of magnitude higher for 30 ps excitation when compared to the bulk single crystal data. In addition to the nonlinear absorption (NLA), we observed nonlinear scattering (NLS). We are combining two mechanisms like NLA and NLS making it an attractive candidate for nonlinear optical device applications and enhance its optical limiting performance.

In Chapter 4, we explored the synthesis of Cu_2O with different morphologies by changing concentration of NaOH in simple chemical coprecipitation method. Size and shape dependent nonlinear optical absorption

properties at nano and pico second regime at 532nm studied in this chapter. We also observed a strong dependence of the effective nonlinear absorption coefficient with change in the particle size. Effective nonlinear absorption coeiffient (β_{eff}) values in the case nano-clusters are higher compared to the micro-particles. To the best of our knowledge, this is the first observation of SA and RSA behavior in the case of Cu_2O at 532 nm laser excitation.

In Chapter 5, we explored the synthesis of CdS nanomaterials by simple chemical coprecipitation technique and heat treatment allowed us to change the size of the particle and also transform the phase from cubic to hexagonal. We observed enhanced two photon excited luminescence (anti-Stokes luminescence) in case of 600 ºC heat treated CdS powder samples due to complete transformation of hexagonal phase.

6.2 Future Prospects

There are several interesting directions for future work in the areas of the research presented in this thesis. One can manipulate properties by changing particles size or doping with transition metal ions in semiconductor nanocrystals. Fe doped BSO single crystals shows enhanced limiting performance compare to their pure BSO single crystals. But there is a contradiction about occupation site of Fe in BSO. It may occupy either Bi site or Si site.

Doping Fe in BSO nano crystals is a challenging task and identification its occupation site it is rather difficult. It is also possible to enhance nonlinear optical properties by doping in BSO nanocrystals. One can dope transition metal ions like Fe in Cu_2O and with different (lower or higher) amounts one can tune its linear and nonlinear optical properties. With lower doping Fe will go into the lattice site of Cu_2O and at higher dopings it sits on the surface of Cu_2O. One can also tune linear and nonlinear optical properties of Cu_2O by Ag doping.

One can tune or enhance upconversion or anti-Stoke luminescence of CdS by doping with transition metal ion or doping with rare earth ions. This type of materials may be useful in enhancing the solar cell efficiency. Novel devices have emerged based on near-infrared to visible upconvertion materials and they include lasers, infrared quantum counters, photo detectors, temperature sensors, biological labeling, solid-state color displays and security coding data storage.

We believe that the novel developments in the field of nanomaterials presented in this thesis and the extension of these ideas into further avenues will show a way for further exciting research in near future.

Research publications:

(Thesis related publications)

1. **H. Sekhar** and D. Narayana Rao "Stokes and anti-Stokes luminescence in heat treated CdS nanopowders" (***Accepted, J. Physical Chemistry C***)
2. **H. Sekhar** and D. Narayana Rao, "Preparation, characterization and nonlinear saturable and reverse-saturable absorption in cuprous oxide nano clusters, micro cubes and micro particles" ***J. Nanoparticle Research*** 14 (2012) 976.
3. **H. Sekhar** and D. Narayana Rao, "Spectroscopic studies on Zn doped CdS nanopowders prepared by simple co precipitation method" ***Journal of Material Science*** 47 (2012) 1964.
4. **H. Sekhar,** P. Prem Kiran and D. Narayana Rao, "Structural, linear and enhanced third-order nonlinear optical properties of $Bi_{12}SiO_{20}$ nanocrystals" ***Materials Chemistry and Physics*** 130 (2011) 113.
5. **H. Sekhar,** P. Prem Kiran and D. Narayana Rao, "Nonlinear optical properties of BSO nanoparticles dispersed in PMMA Matrix" ***Proc. SPIE*** 92 (2010) 7712.

Not included in the thesis

1. **H. Sekhar** and D. Narayana Rao, "Spectroscopic studies on Fe^{3+} doped CdS nanopowders prepared by simple co-precipitation method" ***J. Alloys and compounds*** 517 (2012) 103
2. **H. Sekhar** and D. Narayana Rao "Preparation, structural and linear optical properties of Zinc Sillenite ($Bi_{12.66}Zn_{0.33}O_{19.33}$) Nanocrystals" (Accepted ***Journal of Materials Science: Materials in Electronics***)
3. **H. Sekhar**, G. Trivikrama Rao, P. Harshavardhan Reddy and D. Narayana Rao, "Preparation, structural and its enhanced green up-conversion

luminescence in heat treated rare earth doped CdMnS nano powders" (***Accepted, J. Alloys and Compounds***)

4. **H. Sekhar** and D. Narayana Rao, "Preparation and characterization of heat treated Zn doped CdS powders and it's Up and down conversion luminescence" (***Minor Revision, Science of Advanced Materials***)
5. **H. Sekhar** and D. Narayana Rao, "Tuning linear optical properties by Fe doping in cuprous oxide" (***Manuscript under preparation***)
6. **H. Sekhar** and D. Narayana Rao, "Tuning linear optical properties by Ag doping in cuprous oxide" (***Manuscript under preparation***)

(Co-authored publications not included in the dissertation)

1. P. Prem Kiran, S. Venugopal Rao, M. Ferrari, B. M. Krishna, **H. Sekhar**, Shadak Alee and D. Narayana Rao, "Enhanced Optical Limiting Performance through Nonlinear Scattering in Nanoparticles of CdS, co-doped Ag-Cu, and BSO" ***Nonlinear Optics and Quantum Optics*** 40 (2010) 223.
2. S. Venugopal Rao, P. Prem Kiran, L. Giribabu, M. Ferrari, G. Kurumurthy, B. M. Krishna, **H. Sekhar** and D. Narayana Rao, "Anomalous Nonlinear Absorption Behavior in an Unsymmetrical Phthalocyanine Studied Near 800 nm using Femtosecond and Picosecond Pulses" ***Nonlinear Optics and Quantum Optics***, 40 (2010) 183.

National and International Conferences

1. **H. Sekhar** and D. Narayana Rao "Stokes and anti-Stokes luminescence in heat treated CdS nanopowders" NLS-2013 (***Poster Presentation***, Accepted)
2. P. Harshavardhan Reddy, **H. Sekhar** and D. Narayana Rao "Picosecond nonlinear optical properties of cuprous oxide with different nano-morphologies" NLS-2013 (***Poster Presentation***, Accepted)
3. **H. Sekhar** and D. Narayana Rao "Stokes and anti-Stokes luminescence in heat treated CdS nanopowders" Frontiers in Physics (FIP)-2012, University of Hyderabad, Hyderabad, India. (***Poster Presentation***)
4. **H. Sekhar** and D. Narayana Rao, "Preparation, structural and linear optical properties of Zn doped CdS nanopowders" (ICMST-2012) (at St. Thomas College, Pala) (***Oral***)
5. **H. Sekhar** and D. Narayana Rao, "Observation of confinement effects through liner and nonlinear absorption spectroscopy in cuprous oxide" (ICMST-2012) (at St.Thomas College, Pala) (***Oral***)
6. **H. Sekhar** and D. Narayana Rao, "Preparation, characterization and its nonlinear saturable and reverse-saturable absorption in cuprous oxide nano clusters, micro cubes and micro particles" (ICONSAT-2012) (at ACRI, Hyderabad) (***Poster Presentation***)
7. **H. Sekhar**, P. Prem Kiran and D. Narayana Rao, "Optical Limiting studies of $Bi_{12}SiO_{20}$ (BSO) nanocrystals embedded in PMMA matrix" (India Singapore Joint Physics Symposium-2010) (at University of Hyderabad) (***Poster Presentation***)
8. **H. Sekhar**, P. Prem Kiran and D. Narayana Rao, "Preparation and characterization of $Bi_{12}SiO_{20}$ nanocrystals and its Optical limiting studies" (NLS-2009) (at DAE-BRNS, Mumbai) (***Poster Presentation***)

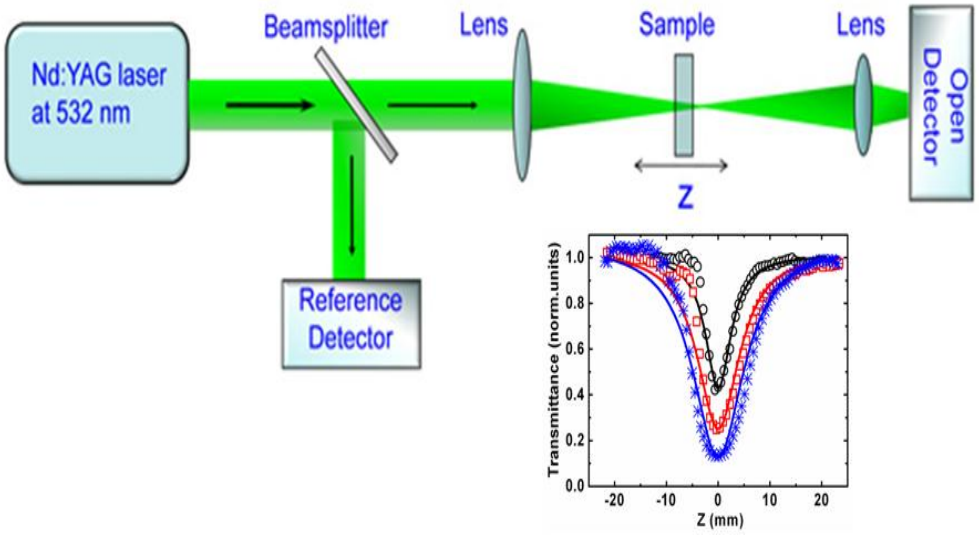
Nd:YAG laser at 532 nm
Beamsplitter
Lens
Sample
Lens
Open Detector
Z
Reference Detector
Transmittance (norm.units)
Z (mm)

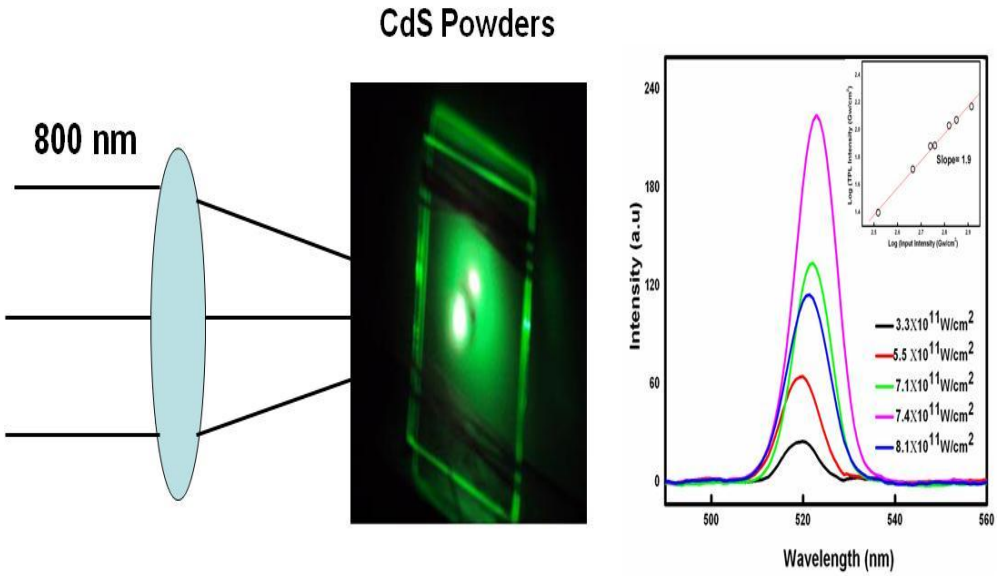
CdS Powders
800 nm
Intensity (a.u)
Wavelength (nm)
Slope= 1.9
3.3X10^11W/cm^2
5.5 X10^11W/cm^2
7.1X10^11W/cm^2
7.4X10^11W/cm^2
8.1X10^11W/cm^2